POLITECNICO DI MILANO

Scuola di Ingegneria Industriale e dell'Informazione

Corso di Laurea Magistrale in Ingegneria Elettrica

HVDC INERTIA SUPPORT

Inertia Emulation Control Strategy for VSC-HVDC Transmission Systems

Relatore: Prof. Luigi Piegari

Correlatore: Prof. Jon Are Suul

Correlatore: Dott. Salvatore D'Arco

Tesi di laurea di:

Francesco Palombi, matricola 900155

Anno accademico 2018/2019

Sommario

I futuri sistemi elettrici di potenza dovranno affrontare nuove sfide dal momento che le unità di generazione termica tradizionali caratterizzate da macchine sincrone (MS) sono sostituite da risorse di energia rinnovabile interfacciate mediante convertitori di elettronica di potenza. L'incremento della quota di generazione eolica e fotovoltaica porterà a periodi con poche centrali con unità di tradizionali generatori sincroni in funzione, e il risultante basso valore di inerzia in rotazione potrà introdurre problemi di stabilità. Possibili situazioni con bassi valori di inerzia in rotazione portano ad affrontare la sfida del controllo di frequenza e di stabilizzare la rete in sistemi elettrici di potenza in isola di grandi dimensioni, come per esempio i sistemi di trasmissione in Gran Bretagna e Irlanda. Nei paesi del nord Europa, molti nuovi collegamenti ad alta tensione in corrente continua (HVDC) sono in costruzione. Condizioni di bassa produzione, grande importazione di energia tramite questi nuovi collegamenti e un basso valore di inerzia in rotazione richiederanno misure preventive per i gestori dei sistemi di trasmissione (TSO).

La diminuzione dell'inerzia equivalente nei sistemi elettrici di potenza richiederà un cambiamento nella gestione delle operazioni del sistema di trasmissione. Quindi, i gestori del sistema di trasmissione dovranno adattare strategie di operazione, schemi di protezione, valutazioni di adeguatezza e pianificare meccanismi per gli intervalli previsti di inerzia equivalente. Per evitare problemi con le già esistenti unità di generazione e i carichi critici, inerzie addizionali dovranno essere mantenute in rotazione oppure il controllo dei convertitori di elettronica di potenza nei sistemi dovrà essere adattato per controbilanciare il problema associato con la bassa inerzia in rotazione. Uno degli approcci per soddisfare questo problema è quello di fornire inerzia virtuale e capacità di regolazione di frequenza dai convertitori di elettronica di potenza nelle connessioni HVDC.

Questa tesi propone un'implementazione del sistema di controllo usato per le connessioni HVDC per introdurre inerzia virtuale e supporto di frequenza. Il sistema di controllo è inizialmente implementato in *Matlab Simulink*, dove le prestazioni sono state valutate. Successiva-

mente, lo stesso sistema di controllo è stato replicato in un software commerciale per l'analisi di stabilità dei sistemi elettrici di potenza (i.e. *DIgSILENT Power Factory*).

Parole chiave - HVDC, Supporto Inerziale, Regolazione di frequenza, VSM, Controllo di convertitore

Abstract

Future power systems will face new challenges as traditional thermal generation units with Synchronous Machines (SMs) are replaced by renewable energy sources interfaced with power electronics converters. An increasing share of wind and PV generation will lead to periods with few traditional SM-based power plants in operation, and the resulting low rotating inertia can introduce stability problems. Scenarios with low system inertia leading to challenges with frequency control and grid stability are emerging in large isolated power systems like the transmission networks in UK and Ireland. In the Nordic countries of Europe several new High-Voltage Direct Current (HVDC) interconnections are under development. Conditions with low load, high HVDC import and low equivalent inertia will require preventive measures from the Transmission System Operators (TSOs).

The decreasing equivalent inertia in power systems will require changes in the transmission system operation and management. Thus, the TSOs will have to adapt their operational strategies, protection schemes, adequacy assessments, and planning tools to the expected range of equivalent inertia. To avoid problems with existing generation units and critical loads, either additional physical inertia must be kept in operation or the control of power converters in the system must be adapted to counteract problems associated with low rotating inertia. One approach to address this issue is to provide virtual inertia and frequency regulation capability by the power electronic converters in HVDC interconnections.

This thesis proposes a control system implementation used for HVDC interconnectors to introduce virtual inertia and frequency support. The control system presented is initially implemented in Matlab Simulink, where the performance have been assessed. Successively, it is replicated in a commercial software for power system stability analysis (i.e. DIgSILENT Power Factory).

Keywords - HVDC, Inertia support, frequency regulation, Virtual synchronous machine, VSC control

Acknowledgement

This thesis summarizes the research conducted during my master thesis internship, which was carried out at SINTEF Energy Research in Trondheim -Norway. The internship has been financed by the "HVDC pro", which is coordinated by Prof. Jon Are Suul and Dr. Salvatore D'Arco as project manager and deputy manager respectively.

First and foremost, I would like to thank my supervisor Professor Luigi Piegari for giving me the opportunity to come here. I would also like to thank my co-supervisors Jon Are Suul and Salvatore D'Arco for their positive encouragement, unwavering support and open door policy throughout my internship period, even though their busy schedule.

I would like to extend my gratitude to my colleagues at the Electric Power Engineering department at SINTEF Energy Research for creating an easy, fun and comfortable working environment. Special thanks is due to Igor Gabiola and Javier Roldan for being a commendable office-mates during my first months and for all their support and help at the beginning of this experience.

Finally, I would like to express my heartfelt thanks to my parents, siblings and grandparents for their endless love and invaluable support and for everything I am and have.

Last but not least, I would like to thank my girlfriend Noemi for her incessant love and patience which gave me the strength to continue in this experience even though the long distance that separated us.

**This work was supported by the project "HVDC Inertia Provision" (HVDC Pro), financed by the ENERGIX program of RCN with project number 268053/E20 and the industry partners; Statnett, Equinor, RTE and ELIA.*

Contents

List of Figures **xi**

List of Tables **xv**

Introduction **1**

1 High Voltage Direct Current Transmission Systems **3**

1.1 Classification of HVDC Links 5

1.2 Line Commutated Converters 6

1.3 Voltage Source Converters 8

2 Control System of HVDC **11**

2.1 Structure of the HVDC 11

2.2 Control scheme of HVDC converters 13

2.2.1 Modelling Conventions 15

2.2.2 Electrical system equations 16

2.3 Virtual Synchronous Machine control system implementation 18

2.3.1 VSM inertia emulation and active power droop control 18

2.3.2 Reactive power droop controller 20

2.3.3 Reference frame orientations 21

2.3.4 Phase locked loop 23

2.3.5 Virtual impedance and voltage controllers 24

2.3.6 Current controllers and active damping 26

2.4 DC-link control system implementation 27

2.4.1 DC-link voltage controller 28

2.4.2 Droop-based AC voltage controller 29

3 Tuning of the controllers **31**

3.1 Tuning of phase locked loop 31

3.1.1 PI Compensator 31

3.1.2 Voltage Controlled Oscillator 32

3.1.3 Low-pass filters 32

3.1.4 Inverse tangent function 33

3.1.5 Tuning criterion 33

3.2 Tuning of Inner Current Controller 35

3.2.1 PI Compensator 36

3.2.2 PWM converter 37

3.2.3 Physical System 37

3.2.4 Tuning criterion 38

3.3 Tuning of outer loop AC voltage controllers 40

3.3.1 PI Compensator 41

3.3.2 Current Controller 41

3.3.3 Physical Circuit 43

3.3.4 Tuning criterion 45

3.4 Tuning of DC-Link Voltage Controller 46

3.4.1 PI Compensator 47

3.4.2 Physical Circuit 47

3.4.3 Tuning Criterion 49

3.5 Tuning of VSM inertia emulation controller 50

3.6 Tuning of active, reactive power and AC voltage droop controllers 53

3.7 Tuning of active damping controller 55

3.8 Summary of parameters 56

4 Dynamic simulations with VSM and DC-link controlled HVDC **59**

4.1 Dynamic response to change in loading with AC ideal voltage sources 59

4.2 Dynamic response to change in loading with equivalent AC grids 64

4.3 Dynamic response to load step with equivalent AC grids 68

4.3.1 Inertia constant and damping coefficient sensitivity 72

5 HVDC interconnector with two VSM controlled converters **75**

5.1 Control scheme of HVDC with two VSMs 75

5.2 VSM inertia emulation with active power droop and DC-link voltage control 77

5.3 Small signal model of the reference HVDC with two VSMs 78

5.3.1 Linearization 79

5.3.2 Analysis of stability 81

5.3.3 Participation factor 82

5.3.4 Eigenvalue sensitivity 84

5.4 Dynamic simulations of HVDC control system with two VSMs 88

5.4.1 Dynamic response to change in loading with AC ideal voltage sources . . 88

5.4.2 Dynamic response to load step with equivalent AC grids 91

Conclusion and Suggestion for Further Research **95**

Summary of the Main results and contributions 95

Outline of relevant topics for further research 97

Closing remarks 97

Bibliography **I**

Appendix A: Non-Linear State Space Model of HVDC with VSM and DC control **V**

Appendix B: Non-Linear State Space Model of HVDC with two VSMs **IX**

List of Figures

1.1 *Break even distance HVDC* 4
1.2 *Monopolar HVDC link* [1] 5
1.3 *Bipolar HVDC link* [1] 6
1.4 *Monopolar back-to-back HVDC link* [1] 6
1.5 *Basic scheme of LCC station* [2] 7
1.6 *Voltage Source Converter connected to a grid through an LCL filter* 9

2.1 *Single-line diagram HVDC* 11
2.2 *PI-model of the submarine cable.* 13
2.3 *Overview of HVDC control scheme* 14
2.4 *VSM inertia emulation with power-frequency droop* 19
2.5 *Reactive power droop controller* 21
2.6 *Vector Diagram* 22
2.7 *Phase locked loop* 23
2.8 *Virtual impedance, voltage control and current control* 25
2.9 *Implementation of active damping* 27
2.10 *DC-Link voltage controller* 28
2.11 *Droop-based AC voltage controller* 29

3.1 *Bode diagram open loop transfer function PLL* 34
3.2 *Bode diagram closed loop transfer function PLL* 35
3.3 *Voltage Source Converter connected to a grid through an LC filter* 36
3.4 *General Block Diagram of Inner Current Control* 36
3.5 *Current Controller* 38
3.6 *Bode diagram inner loop current controller* 40
3.7 *General Block Diagram of AC voltage controller* 40

3.8 *Example of Step Response Current Control* 42
3.9 *AC Voltage Controller* 44
3.10 *Bode diagram outer loop AC voltage controller* 46
3.11 *Block diagram DC-link voltage controller* 46
3.12 *Bode diagram outer loop DC voltage controller* 50
3.13 *Response of active power of VSM to a step in the power reference input varying the damping factor k_d* 51
3.14 *Response of the VSM speed to a step in the power reference input varying the damping factor k_d* 52
3.15 *Phasor diagram of a simplified model of power converter connection to a grid* . . 53
3.16 *Frequency and voltage droop characteristics in grids with dominant inductive behaviour* 55

4.1 *Single-line diagram HVDC with AC voltage sources* 60
4.2 *Active power response of HVDC link connected to AC ideal voltage sources to a step in the power reference input* 60
4.3 *Frequency response of HVDC link connected to AC ideal voltage sources to a step in the power reference input* 61
4.4 *Phase angle orientation of HVDC link connected to AC ideal voltage sources to a step in the power reference input* 62
4.5 *DC voltage response of HVDC link connected to AC ideal voltage sources to a step in the power reference input* 62
4.6 *Single-line diagram HVDC with equivalent AC grids* 64
4.7 *Active power response of HVDC link connected to AC equivalent grids to a step in the power reference input* 66
4.8 *Frequency response of HVDC link connected to AC equivalent grids to a step in the power reference input* 66
4.9 *Phase angle orientation of HVDC link connected to AC equivalent grids to a step in the power reference input* 67
4.10 *DC voltage response of HVDC link connected to AC equivalent grids to a step in the power reference input* 68
4.11 *Nordic frequency response of HVDC link connected to AC equivalent grids to a load step in the Nordic grid* 69

4.12 *Active power response of HVDC link connected to AC equivalent grids to a load step in the Nordic grid* 69
4.13 *European frequency response of HVDC link connected to AC equivalent grids to a load step in the Nordic grid* 70
4.14 *Phase angle orientation of HVDC link connected to AC equivalent grids to a load step in the Nordic grid* 71
4.15 *DC voltage response of HVDC link connected to AC equivalent grids to a load step in the Nordic grid* 71
4.16 *Response of active power of VSM to a load step of 10% varying the mechanical time constant T_a* 73

5.1 *Overview of the innovative HVDC control scheme* 76
5.2 *VSM inertia emulation with active power-frequency droop and DC-link voltage control* 77
5.3 *Root locus of all the system poles for the linearized equilibrium point* 82
5.4 *Participation factor of the unstable complex conjugate pair poles* 83
5.5 *Parametric sensitivity of the critic poles of the system* 85
5.6 *Root locus of the unstable pole pair when the DC buffer capacitances are swept* . 87
5.7 *Root locus of all the system poles for the linearized equilibrium point with buffer capacitance* 87
5.8 *Single-line diagram HVDC with AC voltage sources* 88
5.9 *Active power response of HVDC link connected to AC ideal voltage sources to a step in the power reference input* 89
5.10 *Frequency response of HVDC link connected to AC ideal voltage sources to a step in the power reference input* 89
5.11 *DC voltage response of HVDC link connected to AC ideal voltage sources to a step in the power reference input* 90
5.12 *Single-line diagram HVDC with equivalent AC grids* 91
5.13 *Frequency response of HVDC link connected to equivalent AC grids to a load step* 92
5.14 *Active power response of HVDC link connected to equivalent AC grids to a load step* 93
5.15 *DC voltage transient response of HVDC link connected to equivalent AC grids to a load step* 93

List of Tables

2.1 *Physical parameters of the investigated HVDC configuration* 13

3.1 *Values of the parameters for the tuning of the HVDC control system* 57

4.1 *Parameters of the equivalent synchronous generators and step up transformers* . 65

5.1 *Parameters of the HVDC with two VSMs control system implementation* 80

5.2 *System eigenvalues - the unstable pair of complex conjugate poles is highlighted with red.* 82

Abbreviations

AC	Alternate Current
DC	Direct Current
HP	High Pass
HVDC	High-Voltage Direct Current
LCC	Line Commutated Converter
MIMI	Multiple-Input Multiple-Output
MMC	Modular Multilevel Converter
PCC	Point of Common Coupling
PI	Proportional Integral
PLL	Phase Locked Loop
PWM	Pulse-Width Modulation
RoCoF	Rate of Change of Frequency
SISO	Single-Input Single-Output
SRF	Synchronous Reference Frame
TSO	Transmission System Operator
VSC	Voltage Source Converter
VSM	Virtual Synchronous Machine

Introduction

In classical power systems, the Synchronous Machine (SM) with speed governor and excitation control offers favourable features to support the system operation within a distributed control scheme. Indeed, SMs contribute to the system damping through their inertia, participate in the primary frequency regulation through the droop response of the speed controller, and provide local control of voltage or reactive power flow. These capabilities, and especially the inertial and damping response common to all SMs, are not inherently offered by the power electronics interfaces commonly adopted for the integration of renewable energy sources and HVDC transmission systems. A distributed model for production and local control is also opening the possibility of islanded operation, which is inherently feasible with one or more controllable SMs in the islanded area. Such islanding operation is usually more complex to achieve with power converter interfaces designed for integration with a large-scale power system.

Power from many traditional large-scale generation facilities is currently being replaced by distributed generation capacity from wind power and photovoltaics. The traditional control structures implemented in the power converters for these applications rely on the synchronization to a stable grid frequency supported by large rotating inertias and are not inherently suitable in a SmartGrid context. Thus, from an implementation perspective, significant research efforts are still devoted towards development of control schemes for power electronic converters explicitly conceived to address the conditions emerging in future SmartGrids. Given the inherent benefits of the SMs outlined above, a captivating approach is the control of power electronic converters to replicate the most essential properties of the SM and by that gain equivalent features from a functional point of view. Thus, several alternatives for providing auxiliary services like reactive power control, damping of oscillations and emulation of rotating inertia with power electronic converters have been proposed [3]. Some of these control strategies are explicitly designed to mimic the dynamic response of the traditional SM, and can therefore be classified in broad terms as Virtual Synchronous Machines (VSM).

This thesis starts with a brief overview describing the HVDC transmission systems and highlighting the main advantages derived by their utilization in power transfer. The first chapter is also characterized by a short explanation of the varies technologies adopted for the HVDC transmission systems.

In the second chapter the control system for a HVDC link is presented. The examination of the structure of the system is firstly depicted, then the general overview of the control scheme is shown. Successively, the all the functional blocks used in the implementation of the control of both Voltage Source Converter (VSC) HVDC power electronics converter are studied and all the nonliner mathematical equations are pointed out.

The third chapter presents the approach used for the tuning of all the fundamental block controllers applied in the control scheme previously presented. Starting from the tuning of the phase locked loop, the chapter proceeds to the design of the PI parameters of the inner loop current control, the outer controls. In addition, results of simulations of the VSM are presented to show how the parameters selection influences the performance of the control scheme.

In the fourth chapter, a comparison between the results of the control system obtained by two different software for power system analysis, *Matlab* and *DIgSILENT* is presented. The aim of this chapter is to demonstrate the equivalence between these two environments to exploit the powerful of *DIgSILENT* in the analysis of power system stability. Moreover, simulation of the HVDC control system presented connected to a realistic power system composed by realistic SGs are executed and the results are exposed.

The fifth chapter presents a innovative configuration of HVDC control, which consists of two VSMs. The idea of this control is to obtain the inertia support in both sides of the HVDC link. The pros and drawbacks of this original control are highlighted.

Chapter 1

High Voltage Direct Current Transmission Systems

Chapter introduction

High Voltage Direct Current Transmission systems have the advantages over Alternated Current (AC) in special situations. The motivations for using HVDC systems are generally economic and technical. From the economic point of view, the DC transmission is characterized by higher power transfer in fewer lines than an equivalent AC solution. For DC the frequency is zero, hence the inductance is irrelevant. The effects of the inductance have to be compensated along the AC line and this adds costs for long distances [1].

Furthermore, the HVDC transmission does not suffer from skin effect guaranteeing the possibility to use thinner conductors. However, the HVDC converter stations at both ends are more expensive than equivalent AC terminals and thereby an economical break-even distance arises, as illustrated in Figure 1.1. From the technical viewpoint, there are three main factors that make the HVDC systems interesting:

1. *Long cable transmission:* The charging current in cables being fed with AC makes transmissions over long distances impractical. In order to keep voltage levels and losses within reasonable limits, the HVAC solution requires reactive power compensation equipment along the cables. Such equipment adds cost to the link, and it is in some cases not possible to implement. An example is the undersea transmissions, because if the cable is fed instead with HVDC, the large capacitance is irrelevant since the charging current is frequency dependent.

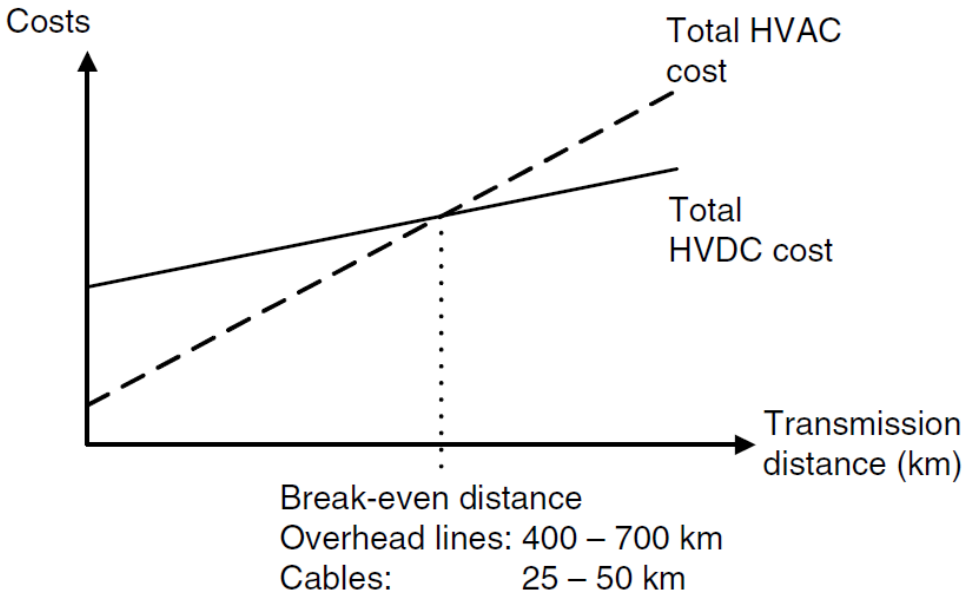

Figure 1.1: *The break-even distance, where the HVDC solution becomes more economical than an equivalent AC.* [1]

2. *Asynchronous interconnection:* The HVDC technology can connect two asynchronous power systems with equal or different frequency. The interconnection is often beneficial for both of the systems and acts as a buffer between them.

3. *Stabilization in power systems:* HVDC links can be used within synchronous AC systems to improve the control of power flow from one part of the system to another and thereby prevent large cascading failures or even blackouts in the grid.

The applications above mentioned are mainly implemented with Line Commutated Converter (LCC). Nowadays, Voltage Source Converter is becoming very competitive due to its several advantages [4].

This chapter will provide a general overview to the different kind of HVDC transmission systems. Two terminal systems will be mainly considered, followed by a brief introduction of multiterminal systems. Moreover, a description of the different technologies will be furnished.

1.1 Classification of HVDC Links

HVDC links may be broadly classified into the following categories:

- Monopolar links;
- Bipolar links;
- Back-to-back.

The basic configuration of a *monopolar link* is shown in Figure 1.2. It is uses one conductor, usually of negative polarity. The return path is provided by ground or water. Cost considerations often lead to the use of such systems, particularly for cable transmission. This type of configuration may also be the first stage in the development of a bipolar system.

Instead of ground return, a metallic return may be used in situations where the earth resistivity is too high or possible interference with underground/underwater metallic structure is objectionable. The conductor forming the metallic return is at low voltage.

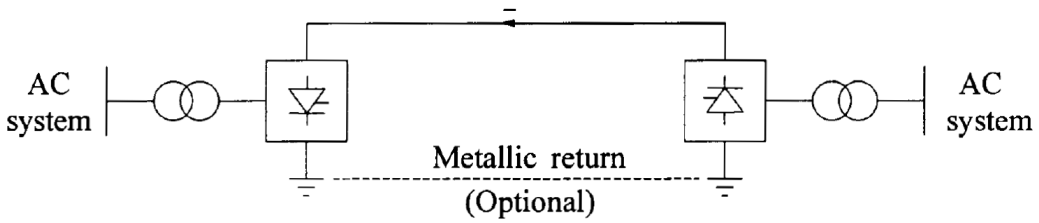

Figure 1.2: *Monopolar HVDC link* [1]

The *bipolar link* configuration is shown in Figure 1.3. It has two conductors, one positive and the other negative. Each terminal has two converters of equal rated voltage, connected in series on the dc side. The junctions between the converters is grounded. Normally, the currents in the two poles are equal and there is no ground current. The two poles can operate independently. If one pole is isolated due to a fault on its conductor, the other pole can operate with ground and thus carry half the rated load or more by using the overload capabilities of its converters and line.

The *back-to-back* HVDC systems may be designed using both of the previous configurations. The converters are located at the same site, with no transmission line between them, interconnecting two AC system. In the Figure 1.4 is it represented a monopolar back-to-back HVDC connection with 12-pulse configuration.

The most common HVDC link configurations consist of the point-to-point connections; where

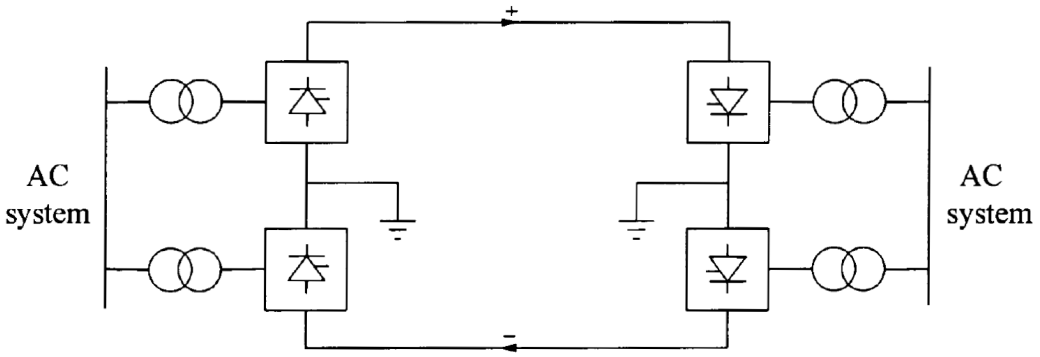

Figure 1.3: *Bipolar HVDC link* [1]

two converter stations are connected by an overhead line or undersea cable.

Multi-terminal HVDC systems are difficult to realize using line commutated converted because reversals of power are effected by reversing of the polarity of DC voltage, which affects all converters connected to the systems. With the voltage source converter, power reversal is achieved instead by reversing the current direction, making parallel-connected multiterminals systems much easier to control. For this reason, multiterminal systems are expected to become much more common in the near future.

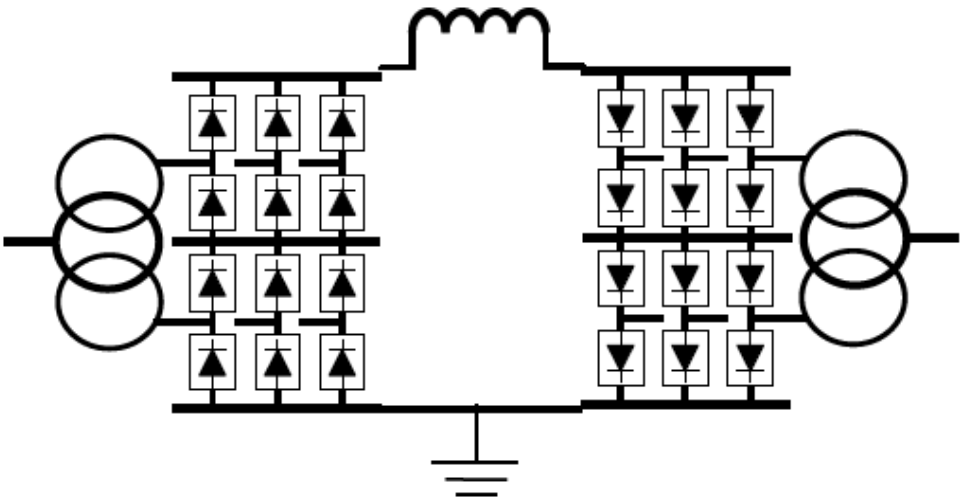

Figure 1.4: *Monopolar back-to-back HVDC link* [1]

1.2 Line Commutated Converters

The development of power electronics and semiconductors in the late 1960s led to the thyristor based valve technology. The AC power is fed to a converter operating as rectifier. Output of

this rectifier is DC power, independent of AC supply frequency and phase. The DC power is transmitted through a conduction medium: an overhead line, a cable or a short length of bus bar. The second converter is operated as inverter and allows the DC power to flow into the receiving AC network.

The converter requires alternating AC voltage to operate as inverter, since the thyristors can only be turned on by control action, and rely on the external AC system to effect the turn-off process. This is the reason why the thyristor-based converter topology used in HVDC is known as Line-Commutated Converter. Conventionally, the LCC HVDC system utilizes the thyristor technology. The required DC system voltages are achieved by a series connection of a sufficient number of valves.

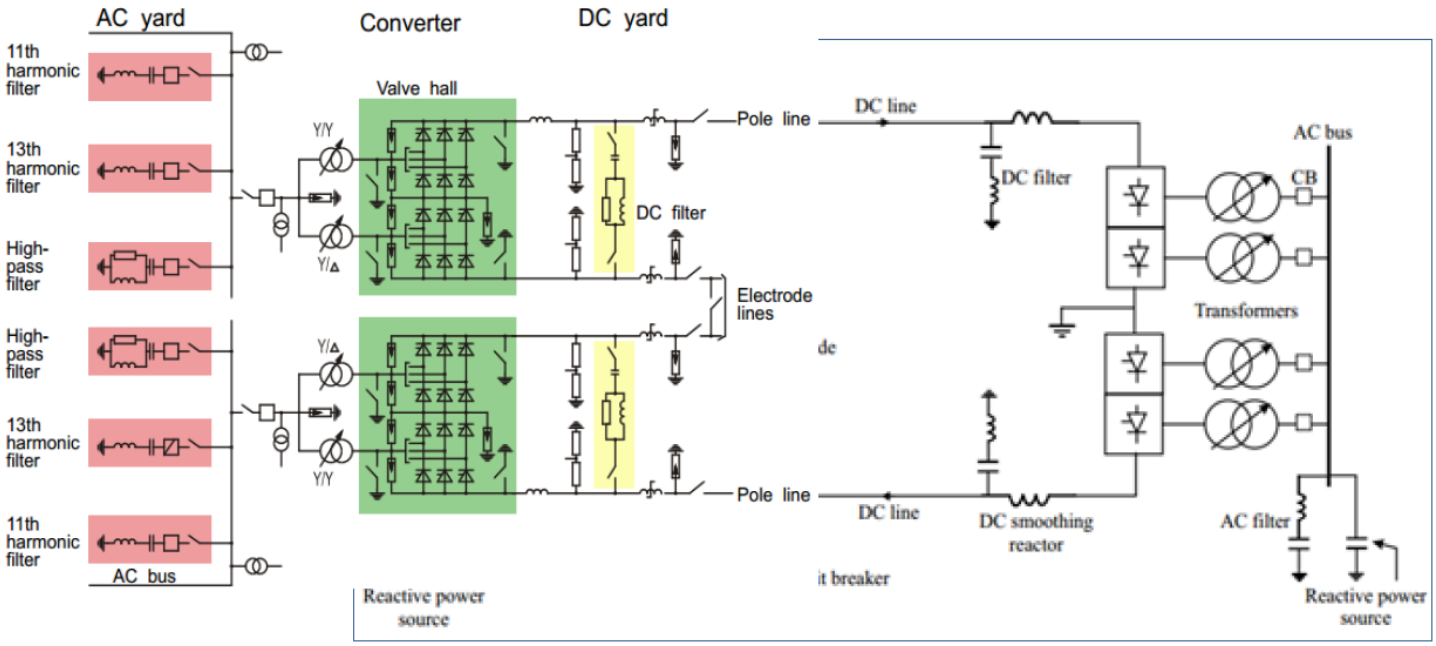

Figure 1.5: *Basic scheme of LCC station* [2]

A basic scheme of a LCC HVDC station is shown in Figure 1.5. The converter station is normally split into two areas:

- AC switchyard, which incorporates the AC harmonic filters and High-Pass (HP) filters;
- Converter island, which incorporates the valve hall;
- Converter transformers;
- DC switchyard.

The LCC HVDC converter must be always connected to a system that contain synchronous machines in order to provide the commutating voltage. As a consequence, this technology cannot feed power into a passive system. With some other types of semiconductor device, such as the Insulated-Gate Bipolar Transistor (IGBT), both turn-on and turn-off can be controlled, giving a second degree of freedom.

1.3 Voltage Source Converters

IGBTs can be used to make self-commutated converters. In such converters, the polarity of DC voltage is usually fixed being smoothed by a large capacitance. For this reason, an HVDC converter using IGBTs is referred to as a Voltage Source Converter.

The operation of the converter is achieved by Pulse Width Modulation (PWM). With PWM it is possible to create any phase angle and/or amplitude (up to a certain limit) by changing the PWM pattern, which can be done almost instantaneously. From a transmission network viewpoint, it acts as a motor or generator without mass that can control active and reactive power almost instantaneously.

In the Figure 1.6 is shown the principal electric scheme to connect the VSC to the grid. The converter reactor, represented by L_f and R_f is one of the key components in VSC due to two main purposes: the first one is to limit the short circuit current at the IGBT valves, while the second is providing a low-pass filter of the PWM pattern. Consequently, the harmonic currents related to the switching frequency and generated by the converter are blocked by the converter reactor. However, for applications above several kilowatts, it becomes quite expensive to realize higher value filter reactors. Moreover, the system dynamic response may become poorer. An alternative and attractive solution to this problem is to use an LCL filter as shown in Figure 1.6 [5].

Up to now, implemented VSC converters have been based on two-/three-level converter which enables switching two or three different voltage levels to the AC terminal of the converter. The converter voltage created by PWM is far from the desired voltage. It needs AC filter to achieve an acceptable waveform. Both, the size of the voltage steps and the related voltage gradients can be reduced or minimized if the AC voltage generated by the VSC can be selected in smaller increments than at two or three level only. The more steps that are used, the smaller is the proportion of harmonics and the lower is the high-frequency noise. The converters with high number of steps are termed multilevel converters. In particular, a new and different approach

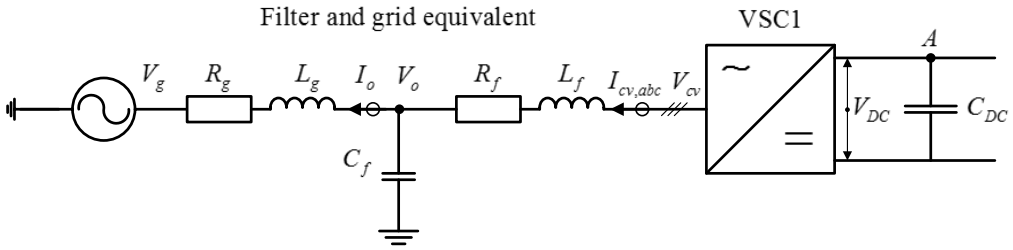

Figure 1.6: *Voltage Source Converter connected to a grid through an LCL filter*

is Modular Multilevel Converter (MMC) technology [6].

Chapter conclusion

This chapter has briefly introduced the high voltage direct current transmission systems and exposed the reason why are becoming so common in the electrical power networks. Moreover, the differences between the two main categories of HVDC transmission systems have been described.

Chapter 2

Control System of HVDC

Chapter introduction

This chapter presents the structure of the HVDC interconnector and shows an overview of the control schemes for the selected power electronics converters used at the two terminals of the DC-link. Furthermore, the modelling conventions used for the analysis of each regulator are expressed. Moreover, each functional block of both the control schemes are described and all the nonlinear mathematical equations are pointed out.

2.1 Structure of the HVDC

The HVDC interconnection studied in this master thesis corresponds to the new HVDC link under construction, which will connect the Nordic grid to the Continental grid, so called NordLink. The system rated power will be 1500 MVA divided between two VSCs, each of them

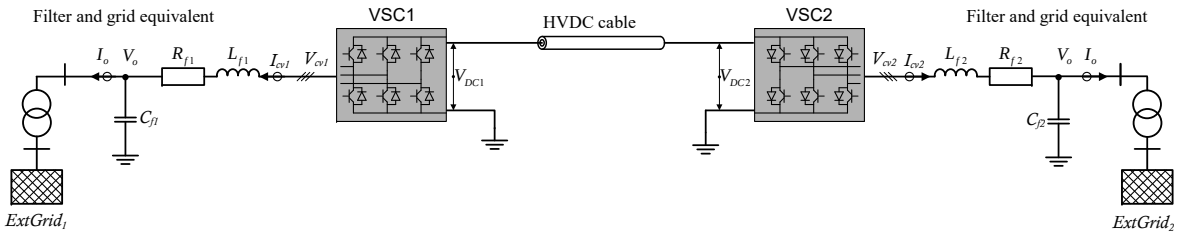

Figure 2.1: *Single-line diagram of a VSC-HVDC transmission system made up by two-level converter connected to external grids through LC filter.*

with a rated power of 750 MVA. Indeed, this HVDC links will be the first case of full bipole VSC-HVDC converter rated at ± 525 kV in the DC side [7].

This thesis focuses particular attention on the control system of an average model of VSC, for this reason the choice of converter type is equivalent. In other words, it can be selected either the two-level VSC or the MMC power electronics converters without leading the generality of the treatise. The main difference between the two type of converter is the interface to the AC grid, which is constituted by an LC filter for the two-level VSC while it is only made up by a series reactor for the MMCs.

The Single-line diagram of a VSC-HVDC transmission system built by two-level Converters connected to external grids through LC is presented in Figure 2.1. It should be noted that for the sake of simplicity, the scheme represents only one of the two asymmetric monopolar HVDC interconnectors which constitute the full bipolar connection.

The use of PWM for switching of the IGBT of the VSC used in HVDC application allows a sinusoidal input current with a total harmonic distortion (THD) under 5%. However, the typical switching frequencies for HVDC application between 2-10 kHz can cause higher order harmonics that can disturb other sensitive loads/equipments on the grids [8].

In order to reduce the current harmonics around the switching frequency a high value series inductance should be used. However, for applications above several kilowatts, it becomes quite expensive to realize higher value filter reactors. Additionally, the system dynamic response may become poorer.

A solution is to use the filter reactor to block the high-frequency harmonic currents generated by the converter from entering into the power system, while a HP filter installed at the Point of Common Coupling (PCC), which has the objective to provide a low-impedance path to ground for the high-frequency harmonic currents. The whole configuration composed by series reactor and HP filter constitute a low-pass filter system [9].

It should be noted that the HP filter installed at the PCC is purely capacitive at the fundamental frequency [10], and its equivalent capacitance is denoted by C_f, as shown in Figure 2.1. The resultant configuration is a LC filter, which could be designed according to the criteria presented in [5].

As it has been anticipated, another possible type of connection can be done using MMC converters, which are connected to external grids only through the series reactor. This filter is a series reactor identified by an equivalent inductance (L_f) and resistance (R_f).

Regarding the modelling of the DC cable, it can be represented by its equivalent PI-model,

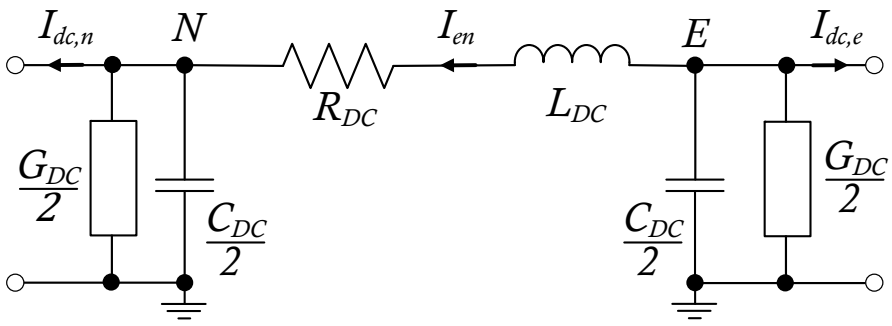

Figure 2.2: *PI-model of the submarine cable.*

as show in Figure 2.2.

The physical parameter of the electric power system have been reported in Table 2.1.

Table 2.1: *Physical parameters of the investigated HVDC configuration*

Parameter		Value	Parameter		Value
Rated Voltage	$V_s[kV]$	232,7	Filter inductance	$l_f[pu]$	0.08
Rated power	$S_b[MVA]$	750	Filter resistance	$r_f[pu]$	0.003
Rated angular frequency	$\omega_b[rad/s]$	2π*50	Filter capacitance	$c_f[pu]$	0.074
Grid inductance Norway	$l_{g,n}[pu]$	0.0308	Grid resistance Norway	$r_{g,n}[pu]$	9e-4
Grid inductance Europe	$l_{g,e}[pu]$	0.0133	Grid resistance Europe	$r_{g,e}[pu]$	4e-4
DC cable inductance	$l_{dc}[pu]$	0.0	DC cable capacitance	$c_{dc}/2[pu]$	2.12
DC cable resistance	$r_{dc}[pu]$	0.086 pu	DC cable conductance	$g_{dc}/2[pu]$	1.7e-3

2.2 Control scheme of HVDC converters

This section describes the control scheme for the selected HVDC link implementation, considering the control system overview of each side of the HVDC interconnector.

The selected implementation is based on an internal representation of the SM inertia and damping behaviour through a reduced order swing equation, together with cascaded voltage and current controllers for operating a VSC. Moreover, the reactive power control has been implemented to control the AC side voltage. An overview of the implemented VSM-based control strategy of the main control for the VSC is shown in the upper part of Figure 2.3. In the figures, upper case symbols indicate physical variables and parameters, while lower case symbols represent per unit quantities.

However, emulation of inertia and damping effects requires an energy buffer with sufficient capacity to represent the energy storage effect of the emulated rotating inertia available. Thus, the amount of virtual inertia that can be added to the system by a single VSM unit will be

limited by the DC-side configuration and by the current rating of the converter.

As explained, the DC-side limitation is one of the factor to take into account. For this rea-

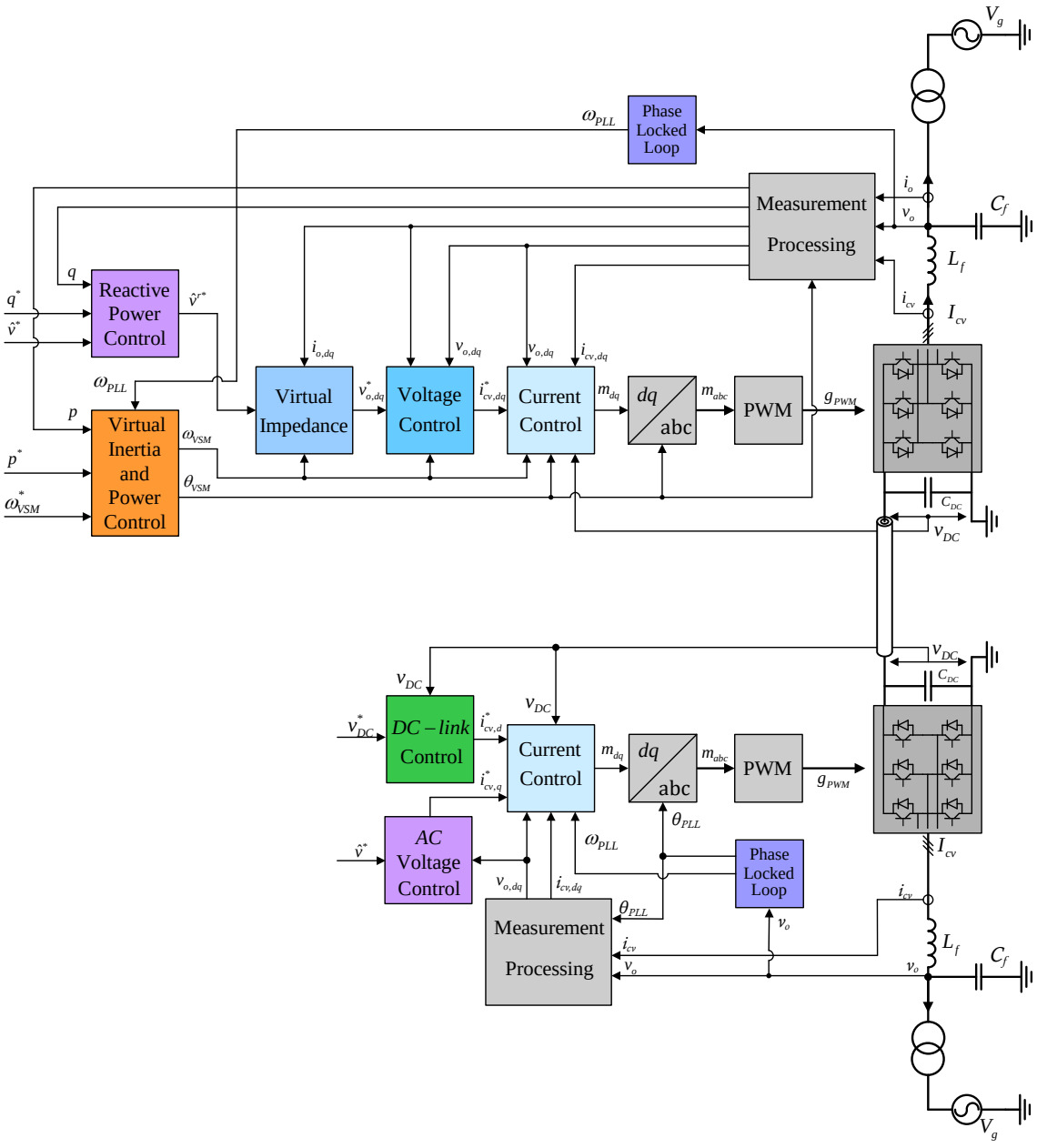

Figure 2.3: *Overview of HVDC control system for a two-level converter.*

son, at least one side of the HVDC system must control the DC-link voltage, v_{dc}. The simplest scenario could be summarized as follow. One converter controls the DC-link voltage and the reactive power flow or the AC voltage amplitude. While, the second converter controls both active and reactive power flow. An overview of the implemented DC-link and AC voltage amplitude

control strategy for VSC is shown in the lower part of Figure 2.3.

2.2.1 Modelling Conventions

In a three-phase VSC, the aim is tracking sinusoidal voltage or current commands. The widely used vector control principle gives the possibility to transform the balanced three-phase voltages and currents to the synchronous dq-axis voltage and current component via the Park Transformation.

The dq-frame possesses different merits that motivate the utilization of vector control principle. Firstly, the control of three half-bridge converters is transformed to an equivalent problem of controlling two equivalent subsystems. Moreover, the concept of instantaneous reactive power can be defined in the dq-frame [11]. If the control is exercised in the dq-frame, a sinusoidal command tracking problem is transformed to an equivalent DC command tracking problem. Hence, Proportional Integral (PI) compensators can be used for the control. Lastly, the time-varying mutually coupled inductances can be transformed to constant parameters.

For the following investigations, upper case symbols indicate physical variables and parameters, while lower case symbols represent per unit quantities. The base value for the per unit system are defined from the apparent power rating of the converter and the peak value of the rated phase voltage [1].

Furthermore, bold symbols represent synchronous reference frame dq variables expressed as space vectors, i.e. as $\mathbf{x} = x_d + jx_q$. The modelling analysis and control of the electrical system on the ac-side will be represented in a Synchronous Reference Frame (SRF) aligned with the voltage vector $\mathbf{v}_o$ at the PCC. The transformation of three-phase voltage and current measurements from the stationary reference frame into the SRF is based on the amplitude-invariant Park Transformation, Equation 2.1 and 2.2, with the d-axis aligned with the voltage vector $\mathbf{v_o}$ and the q-axis leading the d-axis by 90°, as given by 2.3 [1]. Thus, the magnitude of the current and voltage vectors at rated conditions is 1.0 pu.

$$v_d = \frac{2}{3}[v_a \cos(\theta) + v_b \cos(\theta - \frac{2}{3}\pi) + v_c \cos(\theta + \frac{2}{3}\pi)] \tag{2.1}$$

$$v_q = -\frac{2}{3}[v_a \sin(\theta) + v_b \sin(\theta - \frac{2}{3}\pi) + v_c \sin(\theta + \frac{2}{3}\pi)] \tag{2.2}$$

$$\mathbf{v}_o(t) = V_o \cdot e^{j(\omega_g t + \theta_g)} = \mathbf{V}_{o,dq} \cdot e^{j\delta} \tag{2.3}$$

where

$$\mathbf{V}_{o,dq} = V_{od} + j \cdot V_{oq} \quad and \quad \delta = \omega_g t + \theta_g \tag{2.4}$$

Whenever possible, SRF equations are presented in complex space vector notation as:

$$\mathbf{x} = x_d + j x_q \tag{2.5}$$

Thus, active and reactive powers can be expressed on complex or scalar form as:

$$p = Re(\mathbf{v} \cdot \bar{\mathbf{i}}) = v_{o,d} \cdot i_{o,d} + v_{o,q} \cdot i_{o,q} \tag{2.6}$$

$$q = Im(\mathbf{v} \cdot \bar{\mathbf{i}}) = -v_{o,d} \cdot i_{o,q} + v_{o,q} \cdot i_{o,d} \tag{2.7}$$

The current notation indicated in Figure 2.3 result in positive values for active and reactive powers flowing form the converter into the grid.

2.2.2 Electrical system equations

The electrical system equation included in the model, according to Figure 2.3, consists of three main parts.
The first two parts are the AC systems. They are characterized by a set of filter inductors connected to the converters. Then, the shunt capacitor banks constitute the capacitance of the LC filter used to connect the station to the grid. Finally, a Thévenin equivalent of the grid represents the power system connected to the HVDC, which for the sake of simplicity are represented without the subscript of the HVDC side.
The third part is the DC-link connection between two converters. It is made of by the PI-model of the cable as shown in Figure 2.2.

The AC system interface is assumed to achieve a simple model that mainly includes the dynamics of the converter control system and its interaction with the equivalent grid voltage. Considering an instantaneous average model of the converter, the SRF state space equations of the electrical system can be established as given by Equation 2.8:

$$\begin{aligned}
\frac{d\mathbf{i}_{cv}}{dt} &= \frac{\omega_b}{l_f}\mathbf{v}_{cv} - \frac{\omega_b}{l_f}\mathbf{v}_o - \left(\frac{r_f\omega_b}{l_f} + j\cdot\omega_g\omega_b\right)\mathbf{i}_{cv} \\
\frac{d\mathbf{v}_o}{dt} &= +\frac{\omega_b}{c_f}\mathbf{i}_{cv} - \frac{\omega_b}{c_f}\mathbf{i}_o - j\cdot\omega_{pu}\omega_b\cdot\mathbf{v}_o \\
\frac{d\mathbf{i}_o}{dt} &= \frac{\omega_b}{l_g}\mathbf{v}_o - \frac{\omega_b}{l_g}\mathbf{v}_g - \left(\frac{r_g\omega_b}{l_g} + j\cdot\omega_g\omega_b\right)\mathbf{i}_o
\end{aligned} \tag{2.8}$$

In these equations, $\mathbf{i}_{cv}$ is the filter inductor current, $\mathbf{v}_{cv}$ is the converter output voltage, $\mathbf{v}_o$ is the voltage at the filter capacitors, $\mathbf{i}_g$ is the current flowing into the grid equivalent and $\mathbf{v}_g$ is the grid equivalent voltage. The inductance and equivalent resistance of the filter inductor is given by l_f and r_f, the filter capacitor is c_f, while the grid inductance and resistance are given by l_g and r_g. The per unit grid frequency is given by ω_g, while the base angular grid frequency is defined by ω_b. It should be noted that the state space model from Equation 2.8 represents the electrical system in any SRF. Hence, the system will be modelled using the SRF defined by the VSM swing equation in section 2.3, while using the SRF defined by the Phase Locked Loop (PLL) in section 2.4.

Regarding the DC connection, the model used includes the DC dynamic of the converter control systems and the interaction between the two VSC-HVDC converters, as given by Equation 2.9, 2.10 and 2.11.

$$\begin{cases}
\dfrac{dv_{dc,n}}{dt} &= \dfrac{\omega_b}{c_{dc,n}}\cdot(i_{en} - i_{dc,n} - g_{dc,n}\cdot v_{dc,n}) \\
i_{dc,n} &= \dfrac{1}{v_{dc,n}}\left(v_{cvn,d}\cdot i_{cvn,d} + v_{cvn,q}\cdot i_{cvn,q}\right)
\end{cases} \tag{2.9}$$

$$\begin{cases}
\dfrac{di_{en}}{dt} &= \dfrac{\omega_b}{l_{dc}}\cdot v_{dc,e} - \dfrac{\omega_b}{l_{dc}}\cdot v_{dc,n} - \dfrac{\omega_b}{l_{dc}}\cdot r_{dc}\cdot i_{en}
\end{cases} \tag{2.10}$$

$$\begin{cases}
\dfrac{dv_{dc,e}}{dt} &= \dfrac{\omega_b}{c_{dc,e}}\cdot(-i_{en} - i_{dc,e} - g_{dc,e}\cdot v_{dc,e}) \\
i_{dc,e} &= \dfrac{1}{v_{dc,e}}\left(v_{cve,d}\cdot i_{cve,d} + v_{cve,q}\cdot i_{cve,q}\right)
\end{cases} \tag{2.11}$$

It should be noted that the upper equations of 2.9 and 2.11 describes the Kirchhoff's current law at the node "N" and "E" of Figure 2.2, respectively. Whereas, the lower equations describes the power balance between the AC and DC sides of the converters assuming the ideal lossless scenario. It should be noted that the power calculation at the AC side uses the converter terminal measurements instead of the PCC quantities. This is the reason why the $v_{cve,q}$ is not equal to zero even though the PLL synchronization.

As regards the Equation 2.10, it describes the coupling between the two converters.For the sake of simplicity, the subscript "n" and "e" represent the quantities of Norway and Europe, respectively. In these equations, $v_{dc,n}$ and $v_{dc,e}$ are the DC voltages of the VSC converters, i_{en} is the current flowing from Europe to Norway and $i_{dc,n}$ and $i_{dc,e}$ are the DC currents flowing into the VSCs. The inductance and the resistance of the cable are represented by l_{dc} and r_{dc}, while the capacitances and the conductances of each side are given by $c_{dc,n}$,$g_{dc,n}$, $c_{dc,e}$ and $g_{dc,e}$.

2.3 Virtual Synchronous Machine control system implementation

This section describes the control scheme for the selected VSM reference implementation, considering each functional block, and derives the corresponding mathematical model.

An overview of the studied VSM configuration is shown in the upper part of Figure 2.3, where a VSC is connected to a grid through an LC. In the following, the switching effects of the VSC are neglected and an ideal average model is assumed for modelling the converter.

The VSM-based control with virtual inertia provides frequency and phase angle references ω_{VSM} and θ_{VSM} to the internal control loops for operating the VSC, while a reactive power controller provides the voltage amplitude reference $\hat{v}^{r^*}$. Thus, the VSM inertia emulation and the reactive power controller appear as outer loops providing the references for the cascaded voltage and current controllers, further analysed. A Phase Locked Loop detects the actual grid frequency, but this frequency is only used for implementing the damping term in the swing equation. Thus, the operation of the inner loops controllers does not rely on the PLL as in conventional VSC control systems, but only on the power-balance-based synchronization mechanism of the VSM inertia.

In the following sub-sections, the implementation of each functional block of the VSM-based control and the mathematical models of all the system elements from Figure 2.3 are presented.

2.3.1 VSM inertia emulation and active power droop control

The emulation of a rotating inertia and the power-balance based synchronization mechanisms of this virtual inertia are the main difference between the investigated VSM control structure and conventional control systems for VSCs. The VSM implementation investigated in this case is based on a conventional swing equation representing the inertia and damping of a traditional SM [3], [12]. The swing equation used for the implementation is linearized with respect to the

speed so that the acceleration of the inertia is determined by the power balance according to:

$$\frac{d\omega_{VSM}}{dt} = \frac{p^{r^*}}{T_a} - \frac{p}{T_a} - \frac{p_d}{T_a} \tag{2.12}$$

In this equation, p^{r^*} is the virtual mechanical input power, p is the measured electrical power flowing from the VSM into the grid, and p_d is the damping power, while the mechanical time constant is defined as T_a (corresponding to twice the per unit *inertia constant* H in a traditional SM). The per unit mechanical speed ω_{VSM} of the virtual inertia is then given by the integral of the power balance while the corresponding phase angle θ_{VSM} is given by the integral of the speed. A block diagram representing the implementation of the VSM swing equation is shown on the right of Figure 2.4.

The VSM damping power p_d, representing the damping effect of a traditional SM, is defined

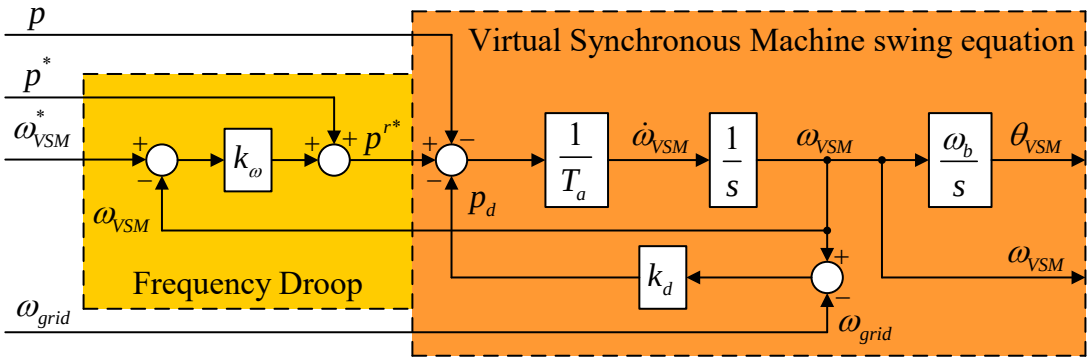

Figure 2.4: *Virtual Synchronous Machine inertia emulation with power-frequency droop.*

by the damping constant k_d and the difference between the VSM speed and the actual grid frequency. Thus, an estimate of the actual grid frequency is needed for the VSM implementation. As indicated in the figure, the estimated frequency is in this case labelled as ω_{grid} and is provided by a PLL.

An external frequency droop, equivalent to the steady-state characteristics of the speed governor for a traditional synchronous machine, is included in the power control of the VSM as shown in the left part of Figure 2.4. This power-frequency droop is characterized by the droop constant k_ω acting on the difference between a frequency reference ω^*_{VSM} and the actual VSM speed ω_{VSM}. Thus, the virtual mechanical input power p^{r^*} to the swing equation is given by the sum of the external power reference set-point, p^*, and the frequency droop effect, as shown on the left of Figure 2.4.

For modelling the VSM in SRF, the phase angle of the VSM in grid connected mode should be constant under steady-state conditions and should correspond to the phase displacement between the virtual position of the VSM internal voltage and the position of the grid voltage vector. Since only the deviation of the VSM speed from the actual grid frequency should be modelled to achieve this, a new set of variables representing the speed deviation $\delta\omega_{VSM}$ and the corresponding phase angle difference $\delta\theta_{VSM}$ is introduced. Thus, the power balance of the VSM inertia can be expressed by Equation 2.13, while the VSM phase displacement is defined by Equation 2.14:

$$\frac{d\delta\omega_{VSM}}{dt} = \frac{p^*}{T_a} - \frac{p}{T_a} - \frac{k_d(\omega_{VSM} - \omega_{PLL})}{T_a} - \frac{k_\omega(\omega_{VSM} - \omega^*)}{T_a} \tag{2.13}$$

$$\frac{d\delta\theta_{VSM}}{dt} = \delta\omega_{VSM} \cdot \omega_b \tag{2.14}$$

Since the VSM speed in steady state will become equal to the grid frequency ω_g, the frequency deviation $\delta\omega_{VSM}$ will return to zero under stable grid connected operation.

The actual per unit speed of the VSM shown in the block diagram of Figure 2.4 can be expressed from the speed deviation $\delta\omega_{VSM}$ resulting from Equation 2.13 and the grid frequency ω_g as given by Equation 2.15. The corresponding VSM phase angle θ_{VSM} is then defined by Equation 2.16.

$$\omega_{VSM} = \delta\omega_{VSM} + \omega_g \tag{2.15}$$

$$\frac{d\theta_{VSM}}{dt} = \omega_{VSM} \cdot \omega_b \tag{2.16}$$

The phase angle θ_{VSM} will then become a saw-tooth signal between 0 and 2π, which is the phase angle that will be used for the transformation between the rotating reference frame defined by the VSM inertia and the three-phase signals, as indicated in the upper part of Figure 2.3.

2.3.2 Reactive power droop controller

The droop-based reactive power controller applied in this case is similar to the controllers commonly applied in microgrid systems [13]. The voltage amplitude reference $\hat{v}^{r^*}$ used for the inner loop voltage and current control is then calculated by Equation 2.17 where $\hat{v}^*$ is the external voltage amplitude reference and q^* is the reactive power reference. The gain k_q is the reactive power droop gain acting on the difference between the reactive power reference and the filtered reactive power measurement q_m. The state of the corresponding first order low pass filter applied in this case is defined by Equation 2.18,where ω_f is the cut-off frequency. A block

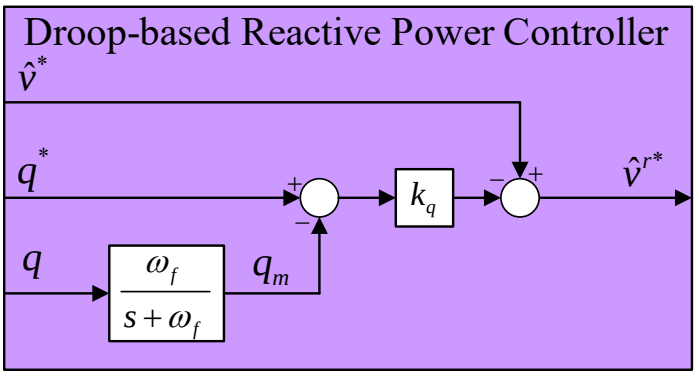

Figure 2.5: *Reactive power droop controller.*

diagram of the resulting control structure is shown in Figure 2.5.

$$\hat{v}^{r^*} = \hat{v}^* + k_q(q^* - q_m) \tag{2.17}$$

$$\frac{dq_m}{dt} = -\omega_f \cdot q_m + \omega_f \cdot q \tag{2.18}$$

2.3.3 Reference frame orientations

The synchronization of the VSM control system to the grid is based on the phase angle orientation of the virtual rotor of the VSM, and the phase angle θ_{VSM} is used in the transformation between the stationary reference frame and the VSM-oriented SRF. Thus, the power balance of the VSM swing equation will ensure the synchronization to the grid voltage without the need for a traditional PLL. Since, the VSM-oriented SRF in steady state rotates with the same frequency as the grid voltage, this phase angle will be continuously increasing between 0 and 2π, as indicated in the vector diagram shown in Figure 2.6. The VSM-oriented SRF is used for both control and modelling of the system, and therefore, also the model of the electrical system will be represented in this reference frame. This has significant advantages for the modelling of the system, since multiple reference frame transformations between a local SRF for controller implementation and a global SRF for electrical system modelling can be avoided. Considering the amplitude of the equivalent grid voltage $\hat{v}_g$ to be known, the voltage vector $\mathbf{v}_g$ in the VSM-oriented SRF can then be expressed by Equation 2.19, while it can be expressed by Equation 2.20

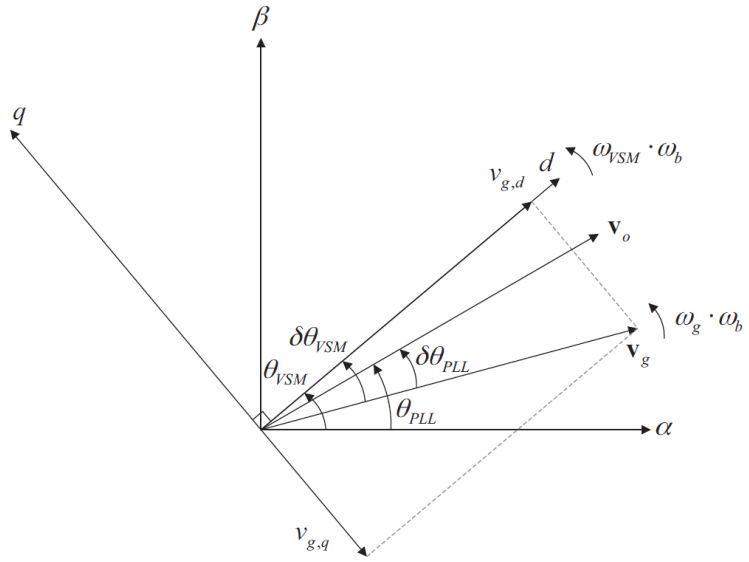

Figure 2.6: *Vector diagram defining the SRF and voltage vector orientations.*

in the SRF for the DC-Link control implementation.

$$\mathbf{v}_g = \hat{v}_g e^{-j\delta\theta_{VSM}} \tag{2.19}$$

$$\mathbf{v}_g = \hat{v}_g e^{-j\delta\theta_{PLL}} \tag{2.20}$$

By the power-balance-based synchronization effect of the VSM swing equation, the control system defines its own reference frame orientation with respect to the grid voltage. In principle, no additional reference frame are needed to model the system from the upper part of Figure 2.3. However, since an estimation of the grid frequency is used to implement the VSM damping effect, a PLL operating on the measured voltage $\mathbf{v}_o$ at the PCC is implemented as part of the control system. Thus, this PLL will estabilish its own SRF aligned with the voltage vector $\mathbf{v}_o$. The phase angle displacement of this PLL with respect to the grid voltage can then be defined as $\delta\theta_{PLL}$ in a similar way as for the phase angle displacement of the VSM. The detailed implementation of the PLL will be presented in the following sub-section, but the definition of its steady state phase displacement $\delta\theta_{PLL}$ with respect to the grid voltage, and the corresponding phase angle θ_{PLL} between the rotating PLL-oriented SRF and the stationary reference frame, is shown in Figure 2.6.

According to the definitions indicated in Figure 2.6, the phase angle between the VSM and the PLL oriented SRFs will be defined by the difference between the VSM and PLL angles. For modelling of the PLL in its own reference frame, the voltage $\mathbf{v}_o$ at the PCC can be transformed

from the VSM-oriented reference frame to the PLL-oriented reference frame by:

$$\mathbf{v}_o^{PLL} = \mathbf{v}_o^{VSM} e^{-j(\delta\theta_{PLL} - \delta\theta_{VSM})} \tag{2.21}$$

2.3.4 Phase locked loop

The Phase Locked Loop applied in this case for tracking the actual grid frequency is based on [14] and its structure is shown in Figure 2.7.

This PLL is using the low-pass filters on the estimated d- and q- axis voltage components

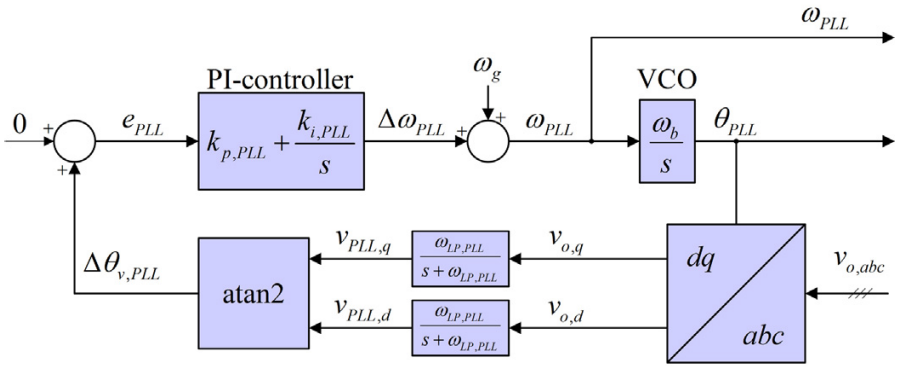

Figure 2.7: *Phase locked loop.*

and an inverse tangent funtion to calculate the phase angle error of the PLL. This phase angle error e_{PLL} is the output to a PI controller tracking the frequency of the measured voltage. For the practical implementation, the estimated frequency ω_{PLL} is then integrated to obtain the estimate of the actual instantaneous phase angle θ_{PLL} used for transformation of the voltage measurements into the PLL-oriented SRF.

For modelling of the PLL, there should be considered both of the two control schemes overview. As regards the VSM implementation, the voltage vector $\mathbf{v}_o$ in the VSM-oriented SRF must be transformed into the PLL-oriented SRF according to Equation 2.21. Whereas, as concern the DC-link voltage control, the voltage vector $\mathbf{v}_o$ in the SRF is already aligned with the PLL-oriented SRF. As a consequence, the two values coincide.

The states of the applied first order low-pass filters in the PLL, defining the filtered voltage v_{PLL}, can be expressed by Equation 2.22 and Equation 2.23, for the VSM and the DC-Link control implementation control schemes respectively, where the cut-off frequency of the applied

low pass filters is given by $\omega_{LP,PLL}$:

$$\frac{d\mathbf{v}_{PLL}}{dt} = -\omega_{LP,PLL} \cdot \mathbf{v}_{PLL} + \omega_{LP,PLL} \cdot \mathbf{v}_o e^{-j(\delta\theta_{PLL} - \delta\theta_{VSM})} \tag{2.22}$$

$$\frac{d\mathbf{v}_{PLL}}{dt} = -\omega_{LP,PLL} \cdot \mathbf{v}_{PLL} + \omega_{LP,PLL} \cdot \mathbf{v}_o \tag{2.23}$$

The integrator state ε_{PLL} of the PI controller can then be defined by:

$$\frac{d\varepsilon_{PLL}}{dt} = \arctan\left(\frac{V_{PLL,q}}{V_{PLL,d}}\right) \tag{2.24}$$

In the same way as explained for the SRF modelling of the VSM swing equation, a speed deviation $\delta\omega_{PLL}$ with respect to the grid frequency is defined for the PLL according to Equation 2.25. The corresponding phase angle displacement, $\delta\theta_{PLL}$, of the PLL is then defined by Equation 2.26:

$$\delta\omega_{PLL} = k_{p,PLL} \cdot \arctan\left(\frac{V_{PLL,q}}{V_{PLL,d}}\right) + k_{i,PLL} \cdot \varepsilon_{PLL} \tag{2.25}$$

$$\frac{d\delta\theta_{PLL}}{dt} = \omega_{PLL} \cdot \omega_b \tag{2.26}$$

In accordance with the definitions introduced for the VSM swing equation, the actual per unit frequency ω_{PLL} detected by the PLL is given by Equation 2.27. The phase angle used in the implementation of the PLL, for transformation of the measured three-phase voltage into the PLL-oriented SRF, is then defined by θ_{PLL} according to Equation 2.28:

$$\omega_{PLL} = \delta\omega_{PLL} + \omega_g \tag{2.27}$$

$$\frac{d\theta_{PLL}}{dt} = \omega_{PLL} \cdot \omega_b \tag{2.28}$$

2.3.5 Virtual impedance and voltage controllers

As indicated in the lower part of Figure 2.3, the voltage amplitude reference $\hat{v}^{r^*}$ resulting from the reactive power droop controller in Figure 2.5 is passed through a virtual impedance before it is used as a reference for controlling the voltage $\mathbf{v}_o$ at the point of common coupling. This virtual impedance can be considered as an emulation of the quasi-stationary characteristic of the synchronous impedance in a traditional SM. The virtual impedance will influence the steady-state and dynamic operation of the VSM, and it will be shown how it can be used to shape the dynamic characteristics of the system. Since power flowing through the virtual inductance

will cause a phase angle displacement between the grid voltage and the virtual inertia position of the VSM, it will also reduce the sensitivity of the VSM to small disturbances in the grid. The influence from the virtual resistance r_v and inductance l_v on the capacitor voltage reference vector $\mathbf{v}_o^*$ defined on basis of the current $\mathbf{i}_o$ according to:

$$\mathbf{v}_o^* = \hat{v}^{r^*} - (r_v + j \cdot \omega_{VSM} \cdot l_v) \cdot \mathbf{i}_o \tag{2.29}$$

The resulting d- and q-axis voltage components $v_{o,d}^*$ and $v_{o,q}^*$ are used directly as references for the decoupled SRF PI voltage controllers as shown in the left part of Figure 2.8.

The detailed structure of SRF PI for the filter capacitor voltage is shown in the middle of

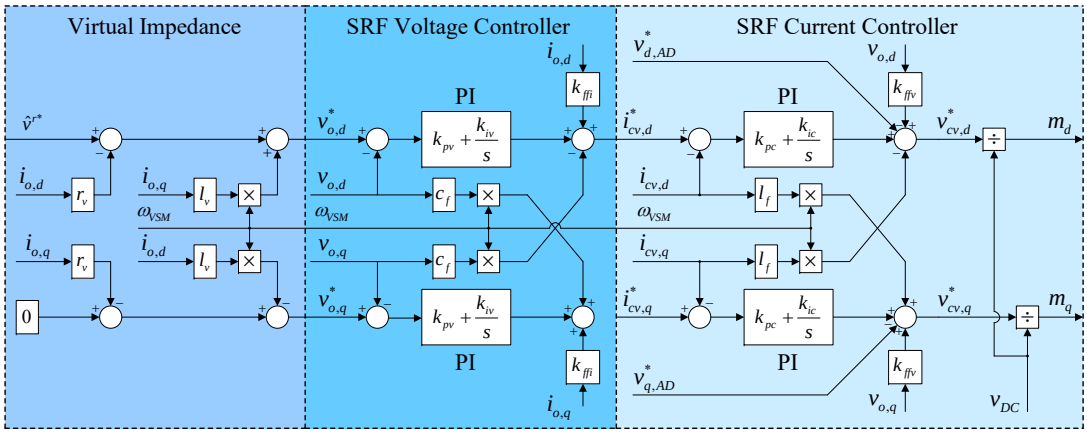

Figure 2.8: *Virtual impedance, voltage control and current control.*

Figure 2.8, and is producing the reference values $\mathbf{i}_{cv}^*$ for the converter currents. These currents reference can be expressed by Equation 2.30, where the PI controller gains are defined by k_{pv} and k_{iv}. A gain factor k_{ffi} that can be set to 1 or 0 is used to enable or disable the feed-forward of measured currents flowing into the grid. The states $\boldsymbol{\xi}$ are defined to represent the integrators of the PI voltage controllers as given by Equation 2.31:

$$\mathbf{i}_{cv}^* = k_{pv}(\mathbf{v}_o^* - \mathbf{v}_o) + k_{iv} \cdot \boldsymbol{\xi} + j \cdot c_f \cdot \omega_{VSM} \cdot \mathbf{v}_o + k_{ffi} \cdot \mathbf{i}_o \tag{2.30}$$

$$\frac{d\boldsymbol{\xi}}{dt} = \mathbf{v}_o^* - \mathbf{v}_o \tag{2.31}$$

The current references from the voltage controllers should be limited to avoid over-currents in case of voltage drops, fault conditions or other severe transients. This also implies that the

voltage controllers must be protected form windup conditions in case the current references are saturated. However, the required limitations and anti-windup techniques for the investigated VSM scheme are similar to what is needed in conventional droop-based control schemes with cascaded SRF voltage and current controllers, as for instance discussed in [15]. Since these limitations are not influencing the dynamics of the control scheme within the normal operating range, further details will not be discussed here.

2.3.6 Current controllers and active damping

The applied inner loop current controllers are conventional SRF PI compensators with decoupling terms [11], as shown in the right side part of Figure 2.8. The output voltage reference from the controller is defined by Equation 2.32, where the resulting voltage reference for the converter is denoted by $\mathbf{v}^*_{cv}$. The proportional and integral gains of the PI controller are defined by k_{pc} and k_{ic}, and a gain factor k_{ffv} is used to disable or enable the voltage feed-forward in the output of the current compensators. The states $\boldsymbol{\gamma}$ are defined to represent the integrators of the PI controllers according to Equation 2.33:

$$\mathbf{v}^*_{cv} = k_{pc}(\mathbf{i}^*_{cv} - \mathbf{i}_{cv}) + k_{ic} \cdot \boldsymbol{\gamma} + j \cdot l_f \cdot \omega_{VSM} \cdot \mathbf{i}_{cv} + k_{ffv} \cdot \mathbf{v}_o - \mathbf{v}^*_{AD} \tag{2.32}$$

$$\frac{d\boldsymbol{\gamma}}{dt} = \mathbf{i}^*_{cv} - \mathbf{i}_{cv} \tag{2.33}$$

In Equation 2.32, the voltage reference for the converter also includes an active damping term $\mathbf{v}^*_{AD}$ designed for suppressing LC oscillations in the filter [5]. The implementation of the active damping algorithm is shown in Figure 2.9, and is based on high pass filtering of the measured voltage $\mathbf{v}_o$, obtained from the difference between $\mathbf{v}_o$ and the low pass filtered value of the same voltage. The resulting high pass filtered signal is then scaled by the gain k_{AD} according to Equation 2.34 and subtracted from the output of the current controllers to cancel detected oscillations in the capacitor voltages:

$$\mathbf{v}^*_{AD} = k_{AD}(\mathbf{v}_o - \boldsymbol{\phi}) \tag{2.34}$$

The corresponding internal states $\boldsymbol{\phi}$ of the low pass filters used for the active damping are defined by Equation 2.35, where ω_{AD} is the cut-off frequency:

$$\frac{d\boldsymbol{\phi}}{dt} = \omega_{AD} \cdot \mathbf{v}_o - \omega_{AD} \cdot \boldsymbol{\phi} \tag{2.35}$$

For the practical implementation of the VSC control system, the voltage reference $\mathbf{v}_{cv}^*$ result-

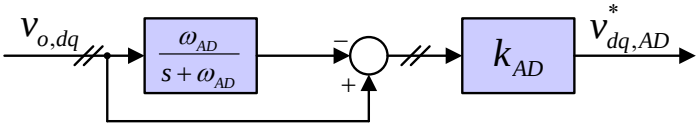

Figure 2.9: *Implementation of active damping.*

ing from the current compensator is divided by the measured DC-link voltage to result in the modulation index $\mathbf{m}$ as show to the right of Figure 2.8. Neglecting the switching operation of the converter and any delay due to the PWM implementation, the instantaneous average value of the per unit converter output voltage is given by the product of the modulation index and the actual DC-voltage. Under this assumption, the output converter voltage will be approximately equal to the voltage reference as summarized by Equation 2.36 [11]:

$$\mathbf{m} = \frac{\mathbf{v}_{cv}^*}{v_{DC}}, \quad \mathbf{v}_{cv} = \mathbf{m} \cdot v_{DC} \rightarrow \mathbf{v}_{cv} \approx \mathbf{v}_{cv}^* \tag{2.36}$$

Thus, the AC side operation of the converter will be effectively decoupled from any dynamics in the DC voltage, and it is not necessary to further discuss or model the DC side of the converter for achieving an accurate representation of the dynamics on the AC side. It should be noted that the DC cable connected to the DC-link of the converter might still impose restrictions on the allowable power exchange during the various operating conditions. However, this detailed discussion will be treated in section 2.4. Whereas, to maintain generality it will be assumed that the power requested from the AC side is always available at the DC-link of the converter.

2.4 DC-link control system implementation

This section describes the implementation for the selected DC-Link and AC voltage control system, considering each functional block, and derives the corresponding mathematical model.

The DC-link and AC voltage control, shown in the lower part of Figure 2.3, provides the d- and q-axis reference of the inner loop current control $\mathbf{i}_{cv}^*$. Conversely from the VSM-based control with virtual inertia, the frequency and phase angle references used by the internal loops for operating the VSC are provided by the PLL, defined by ω_{PLL} and θ_{PLL}, respectively.

The aim of this control system implementation is to maintain the DC-link level within admissible value and to ensure the assumed hypothesis made in subsection 2.3.6 of assuming that the power requested from the AC side is always available at the DC-link of the converter. It should be noted that to achieve this assumption the current control should be characterized by an embedded limitation prioritizing the active component. This specification states that the control system implementation mainly prioritizes the DC-link voltage control and then contributes in the AC voltage regulation.

In the following sub-section, the implementation and the mathematical models of the AC and DC-link voltage controls from the lower part of Figure 2.3 are presented. As regards the other elements, the analysis treated previously can be used.

2.4.1 DC-link voltage controller

As indicated in the lower part of Figure 2.3, the DC-Link voltage reference v^*_{DC} intrinsically defined and corresponding to the unitary value in per unit is used as a reference for controlling the voltage amplitude in the DC-Link.

The detailed structure of the DC-Link PI is shown in Figure 2.10, and is producing the

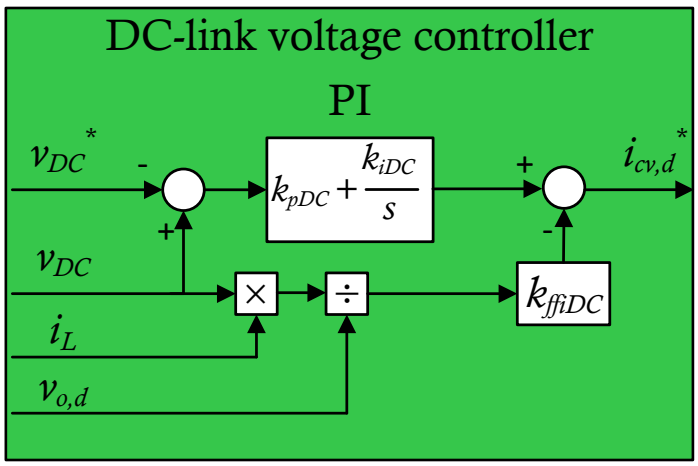

Figure 2.10: *DC-Link voltage controller.*

reference value $i^*_{cv,d}$ for the converter d-axis current. This current reference can be expressed by Equation 2.37, where the PI controller gains are defined by k_{pDC} and k_{iDC}. A gain factor k_{ffiDC} that can be set to 1 or 0 is used to enable or disable the feed-forward of the inner loop d-axis current. The state ζ is defined to represent the integrator of the PI DC-link voltage

compensator as given by Equation 2.38:

$$i^*_{cv,d} = k_{pDC}(v_{DC} - v^*_{DC}) + k_{iDC} \cdot \kappa - k_{ffiDC} \cdot \frac{v_{DC}}{v_d} \cdot i_L \tag{2.37}$$

$$\frac{d\kappa}{dt} = v_{DC} - v^*_{DC} \tag{2.38}$$

2.4.2 Droop-based AC voltage controller

The AC voltage controller applied in this case is similar to the droop-based controller applied in subsection 2.3.2. The q-axis converter current reference used for the inner loop current controller is calculated by Equation 2.39 where $\hat{v}^*$ is the external voltage amplitude reference. The gain k_{AC} is the AC voltage droop gain acting on the difference between the external voltage amplitude reference and the filtered d-frame voltage measured at the point of common coupling $v_{o,dm}$. The state of the corresponding first order low pass filter applied in this case is defined by Equation 2.40, where ω_{AC} is the cut-off frequency. A block diagram of the resulting control structure is shown in Figure 2.11.

$$i^*_{cv,q} = k_{AC}(\hat{v}^* - |v_{o,m}|) \cdot \frac{1}{v_{o,d}} \tag{2.39}$$

$$\frac{d|v_{o,m}|}{dt} = -\omega_{AC} \cdot |v_{o,m}| + \omega_{AC} \cdot \sqrt{v^2_{o,d} + v^2_{o,q}} \tag{2.40}$$

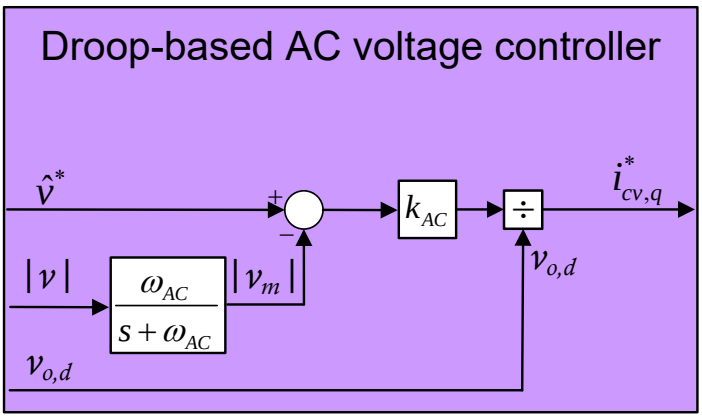

Figure 2.11: *Droop-based AC voltage controller.*

Chapter conclusion

This chapter proposes an innovative approach for controlling the power converter used in HVDC transmission system. The structure of the HVDC interconnector and the control scheme of the power electronics converters have been presented and discussed in detail. Each functional block has been analysed and all the nonlinear mathematical equations have been derived. All the equations needed for the detailed modelling of the HVDC configuration presented in this chapter can be reduced to a model on state-space form. The resulting non-linear state space model of the overall system is reported in Appendix 5.4.2.

Chapter 3

Tuning of the controllers

Chapter introduction

In the chapter 2, all the fundamental blocks of the control schemes used for the HVDC transmission system under analysis have been presented. In this chapter, the tuning of each PI controller and droop-based controller is carry out. The approach used for the tuning of the all fundamental blocks is described, starting from the inner current controller loop and proceeding up to the most external one.

3.1 Tuning of phase locked loop

An accurate active and reactive power control depends on accurate grid synchronization. In subsection 2.3.4 a particular implementation of PLL has been presented. The used configuration consists on a PI compensator, a Voltage Controlled Oscillator (VCO), an inverse tangent function and two low-pass filters for both d- and q-axis.

It should be noted that the approach presented in this sub-section can be used for both the VSM-based and DC-Link voltage control systems being the components of them equal.

3.1.1 PI Compensator

The PI controller process the error of the phase angle, which comes from the comparison $e_{PLL} = 0 + \delta\theta_{v,PLL}$ and provides the angular frequency deviation $\delta\omega_{PLL}$.

The representative equation of the PI compensator is:

$$K_{PLL}(s) = k_{p,PLL} + \frac{k_{i,PLL}}{s} = k_{p,PLL} \cdot \frac{1 + T_{i,PLL} \cdot s}{T_{i,PLL} \cdot s}, \quad where \quad T_{i,PLL} = \frac{k_{p,PLL}}{k_{i,PLL}} \tag{3.1}$$

The parameters $k_{p,PLL}$ and $T_{i,PLL}$ are defined as the proportional gain and integral time constant, respectively. These two quantities are the design parameters to be specified through the tuning of the compensator.

For tuning the parameters of the phase locked loop the VCO and the low-pass filters of the d- and q-axis of the voltage vector $\mathbf{v}_0$ must be considered.

3.1.2 Voltage Controlled Oscillator

The phase angle used in the implementation of the PLL, for transformation of the measured three-phase voltage measurements at the filter capacitors into the PLL-oriented SRF, is obtained through the VCO.

Basically, it consists on a integrator wrap state integrator between 0 and 2π having a proportional gain equals to the rated angular frequency ω_b and the equivalent transfer function is shown by 3.2:

$$h_{VCO}(s) = \frac{\omega_b}{s} \tag{3.2}$$

3.1.3 Low-pass filters

During the transformation into synchronous reference frame, the voltage filtering has been introduced for the dq voltage components without causing phase shift and misalignment. The objective of the voltage filtering is the attenuation of noise and the mitigation of harmonics.

The transfer function of the low-pass filter is expressed by 3.3:

$$h_{LP,PLL}(s) = \frac{\omega_{LP,PLL}}{s + \omega_{LP,PLL}} = \frac{1}{1 + T_{f,PLL}} \tag{3.3}$$

In order to avoid the phase shift and misalignment, the selection of the cut-off frequency of the low-pass filters $\omega_{LP,PLL}$ should be done with care.

In this thesis, the approach used to set up the the cut-off frequency $\omega_{LP,PLL}$ consists on the selection of the highest frequency that allows to filter the possible harmonics present in the measured voltage $\mathbf{v}_0$. In other words, the fifth harmonic is the limitation of the bandwidth of the low-pass filters.

It should be noted that being the filter applied after the park transformation, the third harmonic does not appear since it behaves as zero sequence component and the fifth harmonic angular frequency ω_5 corresponds to 200π rad/s.

In order to select a cut-off frequency which provides a good attenuation of eventual harmonics

without introducing a phase shift and misalignment a value equal to 500 rad/s has been decided.

3.1.4 Inverse tangent function

Several examples of phase locked loop for grid synchronization of power electronics converter can be found in literature [16] [17]. Among them, the inverse tangent function structure has been selected.

The conventional PLL works using only the q-axis component of the measured voltages as the error signal. However, it implies a nonlinearity in the gain of the PLL, as given by Equation 3.4 and 3.5 for small and large deviation, respectively.

$$v_{0,q} \approx \hat{v} \sin(\Delta\theta) \approx \hat{v}\Delta\theta \tag{3.4}$$

$$v_{0,q} \approx \hat{v} \sin(\Delta\theta) \approx \hat{v} \tag{3.5}$$

Furthermore, the value of $v_{0,q}$ will decrease for $\Delta\theta < 90°$ and the grid voltage amplitude $\hat{v}$ always appears as a gain in the system.

The introduction of the inverse tangent function allows accurate detection of the phase angle error in full angular range. Moreover, it implies discontinuity in the phase angle at 180° and the grid voltage amplitude $\hat{v}$, using the inverse tangent function, does not appear as a gain in the system, as can be seen in Equation 3.6:

$$\Delta\theta = \tan^{-1}\left(\frac{v_{0,q}}{v_{0,d}}\right) = \tan^{-1}\left(\frac{\hat{v}\cdot\sin(\Delta\theta)}{\hat{v}\cdot\cos(\Delta\theta)}\right) = \tan^{-1}\left(\tan(\Delta\theta)\right) \tag{3.6}$$

3.1.5 Tuning criterion

The open loop transfer function of the phase locked loop block diagram can be defined as given by 3.7:

$$h_{OL,PLL}(s) = \left(k_{p,PLL} + \frac{k_{i,PLL}}{s}\right) \cdot \frac{\omega_b}{s} \cdot \frac{1}{1 + T_{f,PLL}} \tag{3.7}$$

The characteristic of the open loop transfer function is suitable for tuning the PLL by the Symmetrical Optimum (SO) criterion, which ensures the maximum phase angle at the crossover frequency of the open loop transfer function [18].

From the open loop transfer function shown in Equation 3.7, it is possible to notice the presence of two poles in the origin and one at the cut-off frequency $1/T_{f,PLL}$. In addition the only zero of the transfer function is given by the PI compensator and its correspondent

frequency is $1/T_{i,PLL}$. These considerations lead to the conclusion that the phase characteristic is symmetrical.

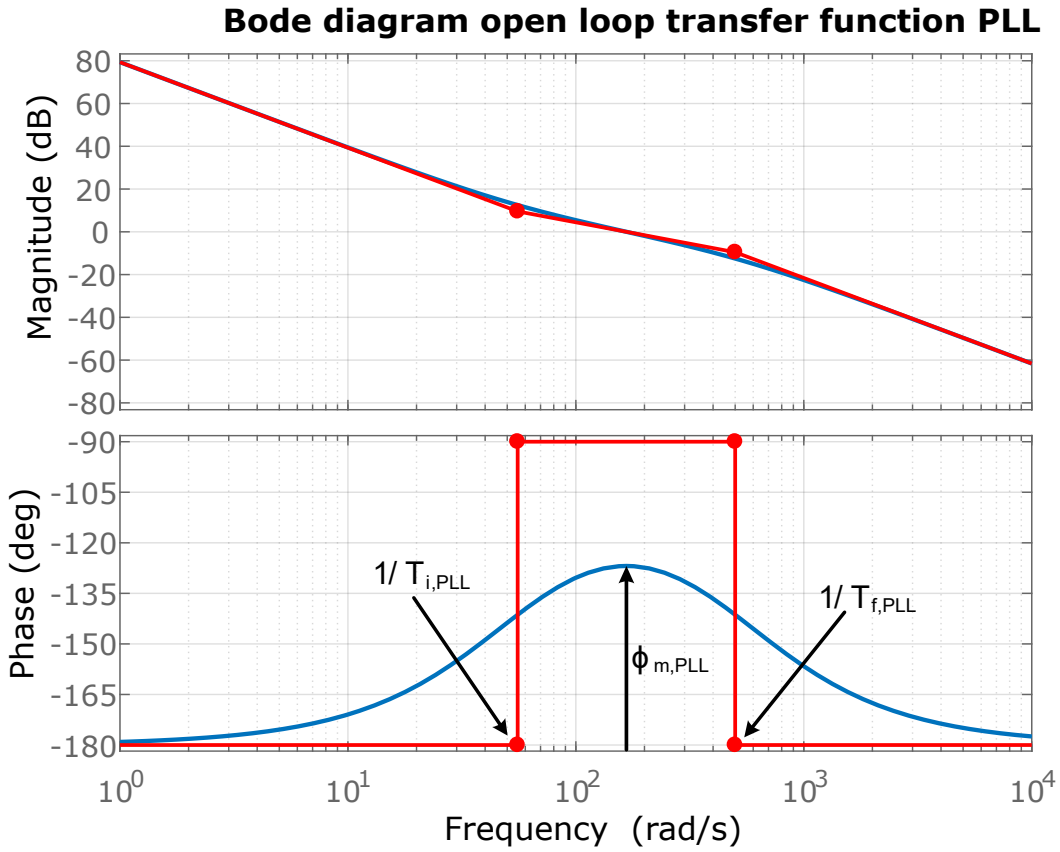

Figure 3.1: *Bode diagram open loop transfer function PLL. The red line represents the asymptotic approximation of the frequency response marking the poles and zeros with dots, while the blue line is the actual frequency response.*

In order to respect the constraint of the SO criterion, the parameters of the PI compensator are expressed in terms of the design parameter "$a = 2\xi + 1$", which relates the tuning of the PI controller to the damping factor ξ of the closed loop transfer function, as given by 3.8:

$$T_{i,PLL} = a^2 \cdot T_{f,PLL}, \quad \omega_{c,PLL} = \frac{1}{a \cdot T_{f,PLL}} \tag{3.8}$$

Substituting the crossover frequency $\omega_{c,PLL}$ into the open loop transfer function in frequency domain, the parameters fulfilling the SO criterion are expressed by 3.9:

$$k_{p,PLL} = \frac{1}{2\pi\omega_b \cdot a \cdot T_{f,PLL}}, \quad k_{i,PLL} = \frac{1}{2\pi\omega_b \cdot a^3 \cdot T_{f,PLL}^2} \tag{3.9}$$

In this thesis, the design parameter a has been selected to get the critical damping, which corresponds to ξ equals to $1/\sqrt{2}$.

The bode diagram representing the magnitude in decibel (dB) and phase in degrees (deg) of the open and closed loop transfer functions of the PLL have been presented in Figure 3.1 and 3.2, respectively.

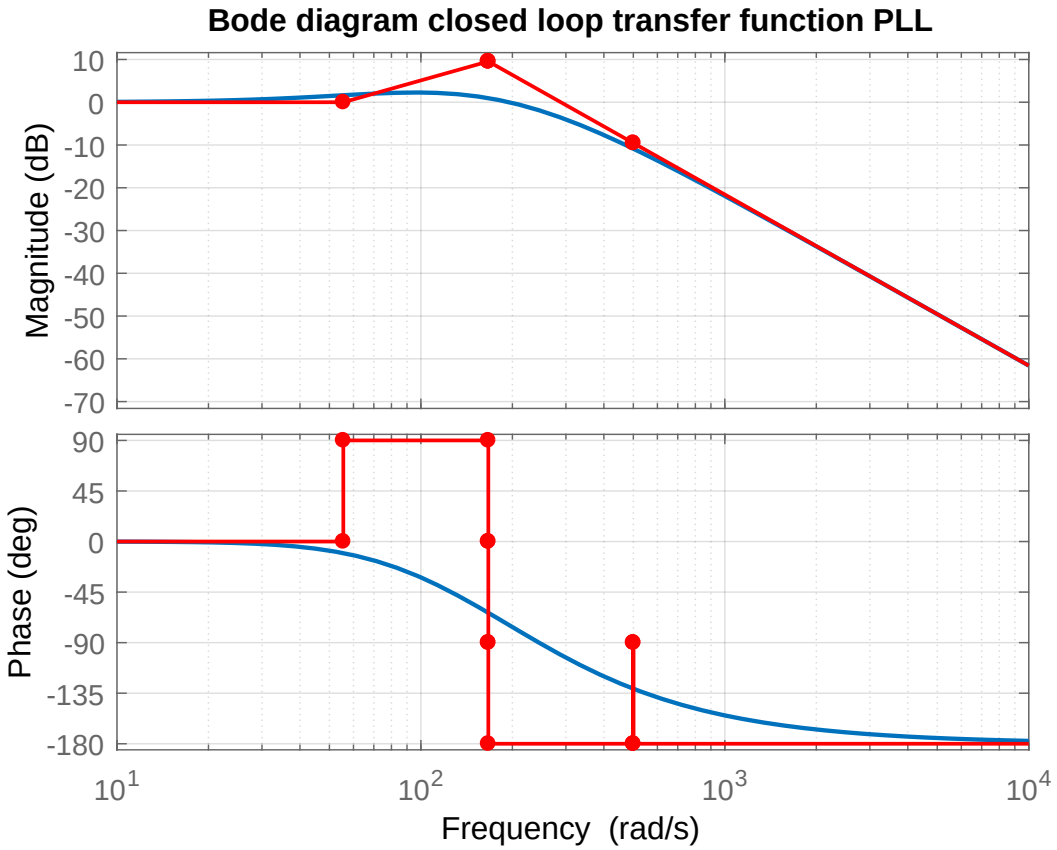

Figure 3.2: *Bode diagram closed loop transfer function PLL. The red line represents the asymptotic approximation of the frequency response marking the poles and zeros with dots, while the blue line is the actual frequency response.*

It can be noticed from the Figure 3.1 that the phase margin of the open loop transfer function is greater than 45 deg, which means that the control system is stable and robust.

3.2 Tuning of Inner Current Controller

The inner current controller of the VSC control structure can be implemented in the dq-frame, based on the basic relationship of the system model. The control loop consist of PI controllers, decoupling factors, feed-forward terms and active damping terms as it has been presented in

subsection 2.3.6.

The objective of the inner current loop is to control the current in the filter inductor represented by L_f and R_f in the Figure 3.3. The simplified block diagram of the current controller VSC system in both d- and q-axis is represented in Figure 3.4. It should be noted that, due to the symmetrical structure of the HVDC interconnector under analysis, the following procedure can be applied to the both HVDC power electronics converters.

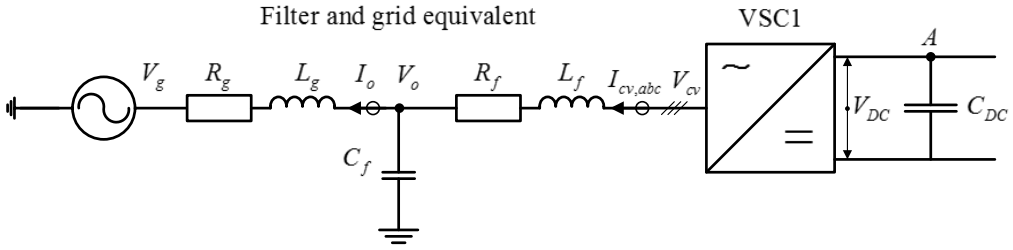

Figure 3.3: *Voltage Source Converter connected to a grid through an LC filter*

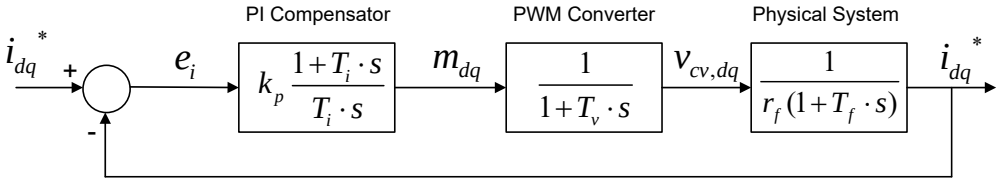

Figure 3.4: *General Block Diagram of Inner Current Control*

3.2.1 PI Compensator

The PI controllers process the error of current that comes from the comparison $\mathbf{e}_i = \mathbf{i}_{cv}^* - \mathbf{i}_{cv}$ and provide the converter voltage references $\mathbf{v}_{cv}^*$. It is possible to notice that the current-control loops are identical. Therefore, the same compensator can be used for both d-axis and q-axis.

The representative equation of the PI compensator is:

$$K_{cc}(s) = k_{pc} + \frac{k_{ic}}{s} = k_{pc} \cdot \frac{1 + T_{ic} \cdot s}{T_{ic} \cdot s}, \quad where \quad T_{ic} = \frac{k_{pc}}{k_{ic}} \tag{3.10}$$

The parameters k_{pc} and T_{ic} are defined as the proportional gain and integral time constant, respectively. These two quantities are the design parameters to be specified through the tuning of the compensator.

For tuning the parameters of the inner loop current controllers, the delay effect of the converter PWM operation must be considered.

3.2.2 PWM converter

From the control point of view, the converter is considered as an ideal power transformer with a time delay [19]. Approximating the effect of the PWM with a first order transfer function, the converter block is given by 3.11.

$$T_v \approx \frac{T_{sw}}{2} \tag{3.11}$$

3.2.3 Physical System

Applying Kirchhoff's Circuit Laws to the right mesh of the ac-side of Figure 1.6, it is possible to define the electrical system equation, as given by 3.12.

$$\mathbf{V}_{cv} = \mathbf{V}_o + R_f \mathbf{I}_{cv} + L_f \frac{d}{dt}\mathbf{I}_{cv} + j \cdot \omega L_f \mathbf{I}_{cv} \tag{3.12}$$

Divided by the base voltage $V_b = Z_b I_b = R_b I_b = \omega_b L_b I_b$, the per unit complex vector equation obtained is represented in 3.13

$$\mathbf{v}_{cv} = \mathbf{v}_o + r_f \mathbf{i}_{cv} + \frac{l_f}{\omega_b}\frac{d}{dt}\mathbf{i}_{cv} + j \cdot \omega_g l_f \mathbf{i}_{cv} \tag{3.13}$$

The current can be controlled by acting on the converter voltage $\mathbf{v}_{cv}$. It is possible to notice that due to the presence of $j \cdot \omega_g l_f \mathbf{i}_{cv}$, the dynamics of the dq-frame currents are coupled. In order to decouple the dynamics the converter voltage reference can be given by PI-controllers and decoupling terms according to 3.14

$$\mathbf{v}^*_{cv} = \mathbf{v}_{PI} + \mathbf{v}_o + j \cdot \omega_g l_f \mathbf{i}_{cv} \tag{3.14}$$

In the Figure 3.5 it is represented the structure of the decoupled PI current controllers. On the basis of the above-mentioned control process, it is possible to sketch the simplified control block diagram of Figure 3.4, which is equivalent to the control system of Figure 3.5. It should be noted that in the control system of Figure 3.5, all the control, feed-forward, and feedback signals are DC quantities in the steady state.

The system behaviour is governed by the Equation 3.13. As it has been introduced before, the model of the VSC in the SRF is a multiple-input multiple-output (MIMO) system, strongly

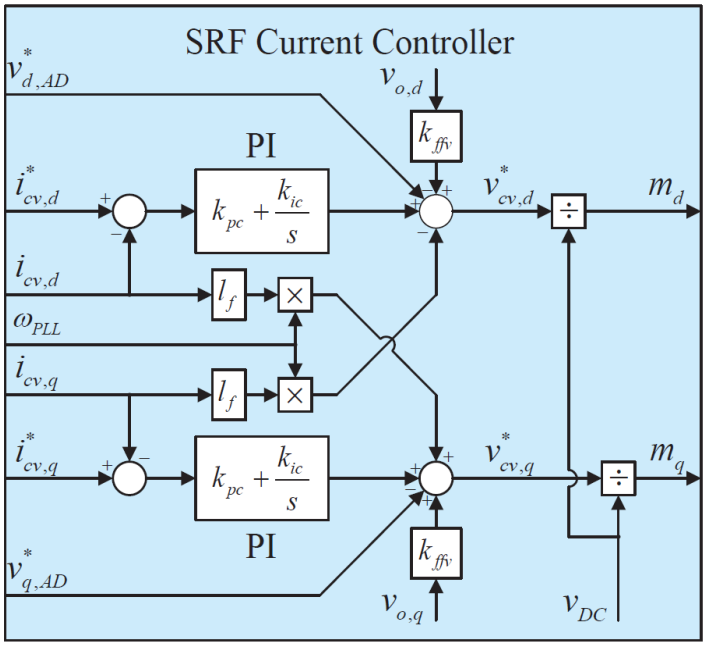

Figure 3.5: *Current Controller*

coupled and non linear. As a result of the Equation 3.14, the control system is reduced to a linear single-input single-output (SISO) system. From the control point of view, the cross-coupling and the feed-forward terms can be considered as disturbances. Therefore, they could be neglected.

3.2.4 Tuning criterion

The open loop transfer function for the current controllers can be defined as given by 3.15. [20]

$$h_{OL,cc,dq}(s) = \frac{i_{cv,dq}(s)}{v_{PI,dq}(s)} \approx \left(k_{pc} + \frac{k_{ic}}{s}\right) \cdot \frac{1}{1 + T_v \cdot s} \cdot \frac{1}{r_f \cdot (1 + T_f \cdot s)} \tag{3.15}$$

where

$$T_f = \frac{L_f}{R_f} = \frac{l_f}{r_f \cdot \omega_b} \tag{3.16}$$

Based on the open loop transfer function 3.15, the PI current controller gains k_{pc} and k_{ic} can be calculated according to the Modulus Optimum (MO) criterion.

The MO criterion is based on two guidelines:

1) *Pole Cancellation*: $T_{ic} = T_f$;
2) *Critical Damping*: $\xi = \frac{1}{\sqrt{2}}$

The cancellation of the slow process pole is done by the zero of the PI-compensator. Hence,

simplifying the expression 3.15 by defining $T_{ic} = T_f$, eliminating the pole of the physical system with the zero of controller, the open loop transfer function becomes,

$$h_{OL,cc,dq}(s) \approx \frac{k_{pc}}{T_f \cdot r_f} \cdot \frac{1}{s \cdot (1 + T_v \cdot s)} \tag{3.17}$$

Based on the open loop transfer function 3.17, because of pole-zero cancellation, the closed loop transfer function becomes a second order transfer function as given by 3.18.

$$h_{CL,cc,dq} = \frac{h_{OL,cc,dq}(s)}{1 + h_{OL,cc,dq}(s)} \approx \frac{\dfrac{k_{pc}}{T_f \cdot r_f \cdot T_v}}{s^2 + \dfrac{1}{T_v} \cdot s + \dfrac{k_{pc}}{T_f \cdot r_f \cdot T_v}} \tag{3.18}$$

The system is identified by the undamped natural frequency ω_n and the damping factor ξ as given by 3.19.

$$\omega_n = \sqrt{\frac{k_{pc}}{T_f \cdot r_f \cdot T_v}}, \quad \xi = \frac{1}{2} \cdot \sqrt{\frac{T_f \cdot r_f}{k_{pc} \cdot T_v}} \tag{3.19}$$

The proportional parameter of the PI compensator k_{pc} is calculated in order to obtain an unitary gain of the closed loop transfer function at the cut-off frequency equal to 1. This condition correspond to the following result:

$$k_{pc} = \frac{T_f \cdot r_f}{2 \cdot T_v} \tag{3.20}$$

By using the value of gain shown in 3.20, the closed loop transfer function is simplified as given by 3.21,

$$h_{CL,cc,dq} = \frac{1}{2T_v^2 \cdot s^2 + 2T_v \cdot s + 1} \tag{3.21}$$

where

$$\omega_n = \frac{1}{T_v \cdot \sqrt{2}} \quad and \quad \xi = \frac{1}{\sqrt{2}} \tag{3.22}$$

Consequently, the tuning of the PI controller by Modulus Optimum Criterion can be summed up according to 3.23.

$$k_{pc} = \frac{T_f \cdot r_f}{2 \cdot T_v} = \frac{l_f}{2\omega_b T_v} \quad and \quad k_{ic} = \frac{r_f}{2 \cdot T_v} \tag{3.23}$$

Furthermore, the phase margin associated to the second order transfer function Ψ_c is given by 3.24,

$$\Psi_c = 90^\circ - \arctan \sqrt{\frac{\sqrt{2} - 1}{2}} \approx 65.5^\circ \tag{3.24}$$

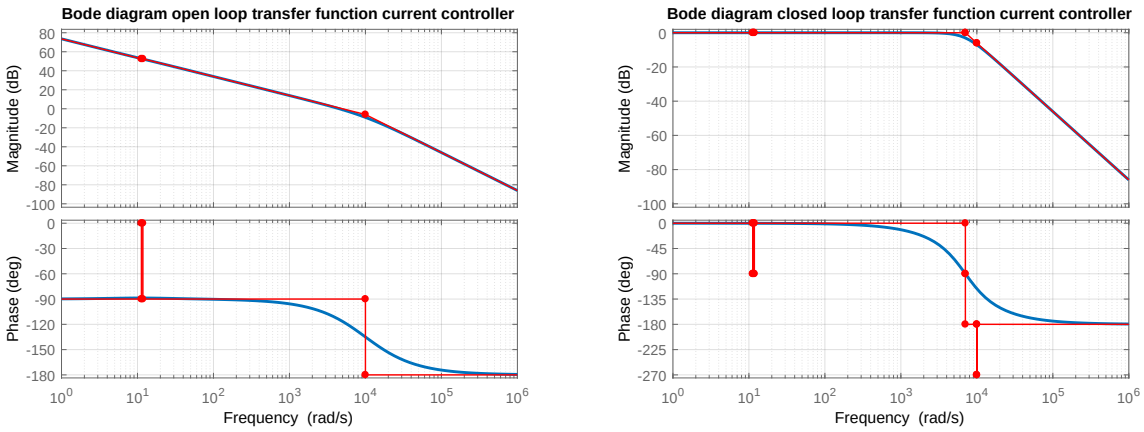

Figure 3.6: *Bode diagram inner loop current controller - Open and closed loop transfer function, left and right chart respectively. The red lines represent the asymptotic approximation of the frequency response marking the poles and zeros with dots, while the blue lines are the actual frequency response.*

Hence, it is possible to conclude that the tuning of the PI current control is fast and stable. The Bode diagrams representing the magnitude in decibel (dB) and phase in degrees (deg) of the open and closed loop transfer functions, shown in Equation 3.15 and 3.18, have been presented in the Figure 3.6.

3.3 Tuning of outer loop AC voltage controllers

The outer AC voltage controllers of the VSC consists of a PI compensator, decoupling factors and feed-forward terms as it has been described in subsection 2.3.5. The objective of this outer loop is to control the voltage at the shunt filter capacitors represented by C_f in the Figure 3.3.

The simplified block diagram of the outer AC voltage controllers is represented in Figure 3.7.

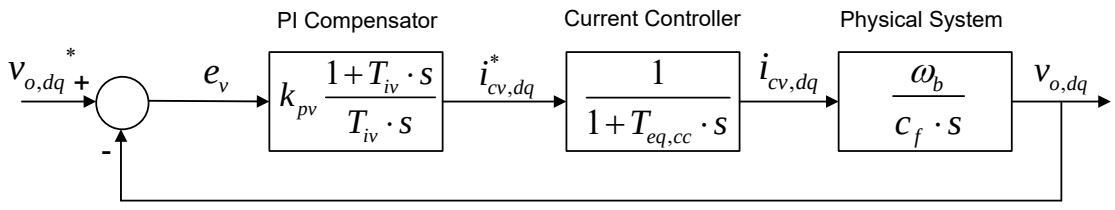

Figure 3.7: *General Block Diagram of AC voltage controller*

3.3.1 PI Compensator

The PI controller processes the error of ac voltage that comes from the comparison $\mathbf{e}_v = \mathbf{v}_o^* - \mathbf{v}_o$ and provide the converter current references $\mathbf{i}_{cv}^*$. It is possible to notice that the outer control loops are identical. Therefore, the same compensator can be used for both d-axis and q-axis.

The representative equation of the PI compensator is:

$$K_{vc}(s) = k_{pv} + \frac{k_{iv}}{s} = k_{pv} \cdot \frac{1 + T_{iv} \cdot s}{T_{iv} \cdot s}, \quad where \quad T_{iv} = \frac{k_{pv}}{k_{iv}} \tag{3.25}$$

The parameters k_{pv} and T_{iv} are defined as the proportional gain and integral time constant, respectively. These two quantities are the design parameters to be specified through the tuning of the compensator.

For tuning the parameters of the outer-loop ac-voltage controllers, the time constant $T_{eq,cc}$, representing the closed loop current controller, must be considered.

3.3.2 Current Controller

In many cases, the closed current loop is assumed to be ideal and represented by a unity factor for the design of outer loop. Instead of assuming the controller to be ideal, a simplified representation of the second order closed loop transfer function of the current controller by the equivalent first order approximation is considered here.

The simplification is found by requiring the time integral of the difference between the reference and the output of the system after a reference step input to be equal for both the original second order model and the approximated one.

The closed loop second order transfer function of current controller is defined by Equation 3.21. Let the transfer function be approximated by an equivalent first order transfer function as given by 3.26.

$$h_{ec,cc}(s) = \frac{1}{1 + T_{eq,cc} \cdot s} \tag{3.26}$$

The equivalent time constant $T_{eq,cc}$ of the approximated transfer function is evaluated by equating the error function between the closed loop second order and first order transfer functions.

Taking a step function as an input,

$$U(s) = \frac{1}{s} \tag{3.27}$$

The respective error functions are defined by 3.28 and 3.29.

$$Err_1(s) = \frac{1}{s} - \left(\frac{1}{s} \cdot \frac{1}{2T_v^2 \cdot s^2 + 2T_v \cdot s + 1}\right) = \frac{2T_v^2 \cdot s + 2T_v}{2T_v^2 \cdot s^2 + 2T_v \cdot s + 1} \tag{3.28}$$

$$Err_2(s) = \frac{1}{s} - \left(\frac{1}{s} \cdot \frac{1}{1 + T_{eq,cc} \cdot s}\right) = \frac{T_{eq,cc}}{1 + T_{eq,cc} \cdot s} \tag{3.29}$$

The condition for the two transfer function to be equal is that the integral from zero to infinity of the time domain errors coincide, as shown in 3.30.

$$\int_0^\infty Err_1(t) \cdot \mathrm{d}t = \int_0^\infty Err_2(t) \cdot \mathrm{d}t \tag{3.30}$$

Applying the Laplace transform, it is possible to state that the limit of the complex variable s to zero of Equation 3.28 and Equation 3.28 is equal to the error integrals expressed in Equation 3.30.

$$\mathcal{L}\left[Err_1(t)\right] = Err_1(s) = \int_0^\infty \left[e^{-st} \cdot Err_1(t)\right] \mathrm{d}t \tag{3.31}$$

$$\lim_{s \to 0} Err_1(s) = \int_0^\infty Err_1(t) \cdot \mathrm{d}t \tag{3.32}$$

Hence, the condition of equality in Equation 3.30 can be expressed as given by 3.33.

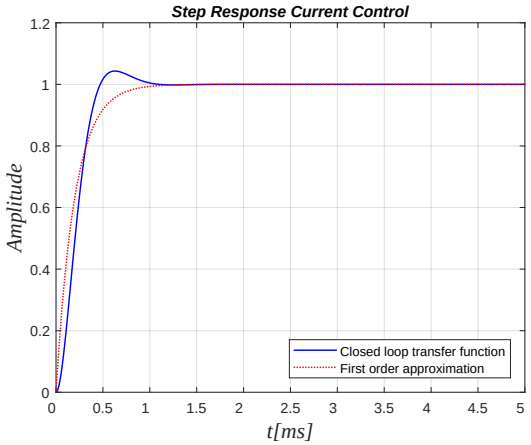

Figure 3.8: *Comparison between the step responses of the complete second order transfer function and the equivalent first order approximation of the current control*

$$\lim_{s \to 0} Err_1(s) = \lim_{s \to 0} Err_2(s) \tag{3.33}$$

$$\lim_{s\to 0} \frac{2T_v^2 \cdot s + 2T_v}{2T_v^2 \cdot s^2 + 2T_v \cdot s + 1} = \lim_{s\to 0} \frac{T_{eq,cc}}{T_{eq,cc} \cdot s + 1} \tag{3.34}$$

As a conclusion, the equivalent time constant $T_{eq,cc}$ of the closed loop current control is equal to twice the PWM delay T_v, as expressed in 3.35

$$T_{eq,cc} = 2T_v \tag{3.35}$$

In the Figure 3.8 is it possible to appreciate the different of between the step response of closed loop transfer function and the first order approximation.

3.3.3 Physical Circuit

Applying the Kirchhoff's Current Law at the node "o" in the scheme of Figure 3.3, it is possible to write the electrical system equation, as given by 3.36.

$$\frac{d\mathbf{v}_o(t)}{dt} = \frac{1}{C_f}\left[\mathbf{i}_o(t) - \mathbf{i}_{cv}(t)\right] \tag{3.36}$$

Let us express the dynamic equation in dq-frame using the vector principle.

$$\frac{d}{dt}\left(\mathbf{V}_{o,dq} \cdot e^{j\delta}\right) = \frac{1}{C_f}\left(\mathbf{I}_{o,dq} \cdot e^{j\delta} - \mathbf{I}_{cv,dq} \cdot e^{j\delta}\right) \tag{3.37}$$

Developing the derivative of time in the left side term

$$\frac{d\mathbf{V}_{o,dq}}{dt} \cdot e^{j\delta} + j \cdot \frac{d\delta}{dt} \cdot \mathbf{V}_{o,dq} \cdot e^{j\delta} = \frac{1}{C_f}\left(\mathbf{I}_{o,dq} - \mathbf{I}_{cv,dq}\right) \cdot e^{j\delta} \tag{3.38}$$

Let us simplify $e^{j\delta}$ in both sides, and according to Equation 2.4, it is possible express $\frac{d\delta}{dt} = \omega_g$. The result is shown in 3.39

$$\frac{d\mathbf{V}_{o,dq}}{dt} = -j \cdot \omega_g \mathbf{V}_{o,dq} + \frac{1}{C_f}\mathbf{I}_{o,dq} - \frac{1}{C_f}\mathbf{I}_{cv,dq} \tag{3.39}$$

The per unit complex vector equation can be obtained dividing both terms by the base current $I_b = V_b\omega_b C_b$, as represented in 3.40.

$$\frac{d\mathbf{v}_{o,dq}}{dt} = -j \cdot \omega_{pu} \cdot \omega_b \cdot \mathbf{v}_{o,dq} + \frac{\omega_b}{c_f}\mathbf{i}_{o,dq} - \frac{\omega_b}{c_f}\mathbf{i}_{cv,dq} \tag{3.40}$$

Decomposing the Equation 3.40 into real and imaginary parts, the dq-frame model of the circuit of Figure 3.3 is obtained, as given by 3.41-3.42:

$$\frac{dv_{o,d}}{dt} = \frac{\omega_b}{c_f} \cdot i_{o,d} - \frac{\omega_b}{c_f} \cdot i_{cv,d} + \omega_{pu} \cdot \omega_b \cdot v_{o,q} \tag{3.41}$$

$$\frac{dv_{o,q}}{dt} = \frac{\omega_b}{c_f} \cdot i_{o,q} - \frac{\omega_b}{c_f} \cdot i_{cv,q} - \omega_{pu} \cdot \omega_b \cdot v_{o,d} \tag{3.42}$$

In 3.41 and 3.42 $v_{o,d}$ and $v_{o,q}$ are state variables, $i_{cv,d}$ and $i_{cv,q}$ are control inputs, while $i_{o,d}$ and $i_{o,q}$ are disturbances inputs. Due to the presence $\omega_{pu} \cdot \omega_b$ terms in 3.41 and 3.42, dynamics of $v_{o,d}$ and $v_{o,q}$ are coupled. To decouple the dynamics, it is possible to determine $i^*_{cv,d}$ and $i^*_{cv,q}$ as given by 3.43 and 3.44:

$$i^*_{cv,d} = i_{PI,d} - i_{o,d} - \omega_{pu} \cdot \omega_b \cdot \frac{c_f}{\omega_b} \cdot v_{o,q} \tag{3.43}$$

$$i^*_{cv,q} = i_{PI,q} - i_{o,q} + \omega_{pu} \cdot \omega_b \cdot \frac{c_f}{\omega_b} \cdot v_{o,d} \tag{3.44}$$

where $i_{PI,d}$ and $i_{PI,q}$ are two new control inputs. In the Figure 3.9 it is represented the

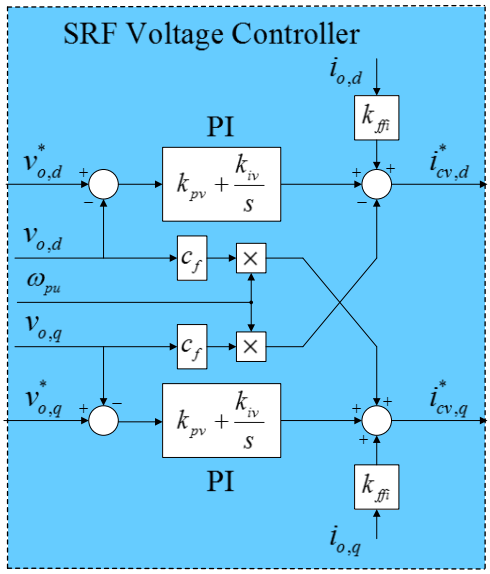

Figure 3.9: *AC Voltage Controller*

structure of the decoupled PI SRF voltage controller.

The system behaviour governed by the equations 3.41 and 3.42, as the current control, is a MIMO system, strongly coupled and non linear. As a result of the equations 3.43 and 3.44,

the control system can be reduced to a SISO system. From the control view point, the cross-coupling terms $\omega_{pu} \cdot c_f$ and the feed-forward components $\mathbf{i}_{o,dq}$ can be considered as disturbances. Therefore, they could be neglected.

Furthermore, the system can be rewritten according to 3.45 and 3.46:

$$\frac{dv_{o,d}}{dt} = \frac{\omega_b}{c_f} \cdot i_{PI,d} \tag{3.45}$$

$$\frac{dv_{o,q}}{dt} = \frac{\omega_b}{c_f} \cdot i_{PI,q} \tag{3.46}$$

3.3.4 Tuning criterion

Applying the Laplace Transform to equations 3.45 and 3.46, the open loop transfer functions of the ac-voltage controller can be derived, as given by 3.47:

$$h_{OL,vc,dq}(s) = \frac{\mathbf{v}_{o,dq}}{\mathbf{i}_{PI,dq}} = \left(k_{pv} + \frac{k_{iv}}{s}\right) \cdot \frac{1}{1 + T_{eq,cc} \cdot s} \cdot \frac{\omega_b}{c_f \cdot s} \tag{3.47}$$

Based on open loop transfer function 3.47, the PI voltage controller gains, k_{pv} and k_{iv}, must be computed taking into account the bandwidth limitation introduced by the inner current control and the closed loop transfer function can be written as given by Equation 3.48:

$$h_{CL,vc,dq}(s) = \frac{h_{OL,vc,dq}(s)}{1 + h_{OL,vc,dq}(s)} \tag{3.48}$$

It should be noted that the open loop transfer funtion of the AC voltage controller is similar to the PLL one. Consequently, the voltage controller parameters can be tuned according to the Symmetrical Optimum (SO) Criterion, as well as section 3.1.

The PI controller gains are expressed in terms of a design parameter 'a' that relates the tuning of the PI controller to the damping factor ξ of the closed loop transfer function, as given by 3.49

$$k_{pv} \approx \frac{T_c}{a \cdot T_{eq,cc}}, \quad k_{iv} \approx \frac{T_c}{a^3 \cdot T_{eq,cc}} \tag{3.49}$$

where

$$a \approx 2\xi + 1, \quad T_c = \frac{c_f}{\omega_b} \tag{3.50}$$

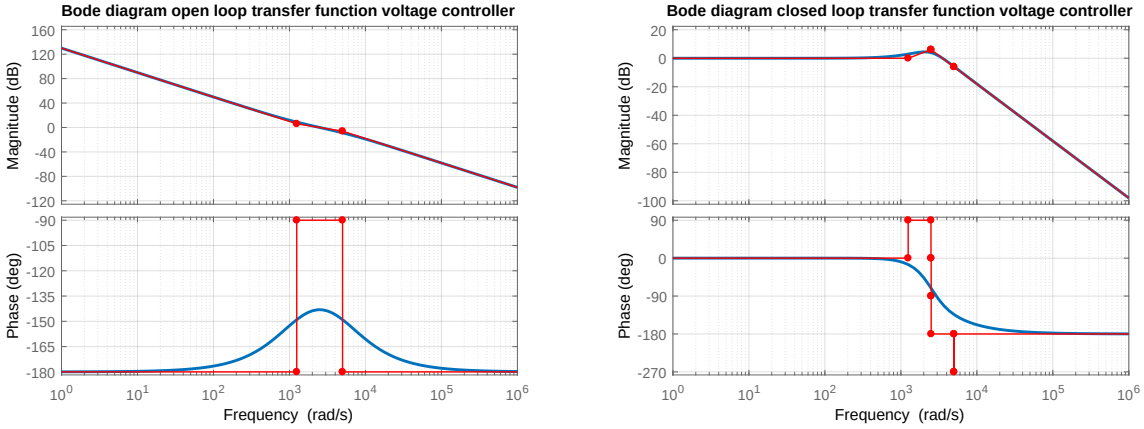

Figure 3.10: *Bode diagram outer loop AC voltage controller - Open and closed loop transfer function, left and right chart respectively. The red lines represent the asymptotic approximation of the frequency response marking the poles and zeros with dots, while the blue lines are the actual frequency response.*

In this thesis, the design parameter a has been selected to get a limited overshoot at the cut-off frequency (i.e. almost 3 dB) but the faster response as possible of the system. These two condition coincide with a value of the design parameter equal to almost 2.

The Bode diagrams representing the magnitude in decibel (dB) and phase in degrees (deg) of the open and closed loop transfer functions, shown in Equation 3.47 and 3.48, have been presented in the Figure 3.10.

3.4 Tuning of DC-Link Voltage Controller

The DC-link controller consist of PI compensator and feed-forward term as it has been presented in subsection 2.4.1. The closed loop current control is considered for the tuning of the PI compensator, as seen in section 3.3. While, the physical system to analyse is mainly represented by the DC capacitor C_{DC} in the Figure 3.3, which models the shunt parameter of the DC cable shown in Figure 2.2.

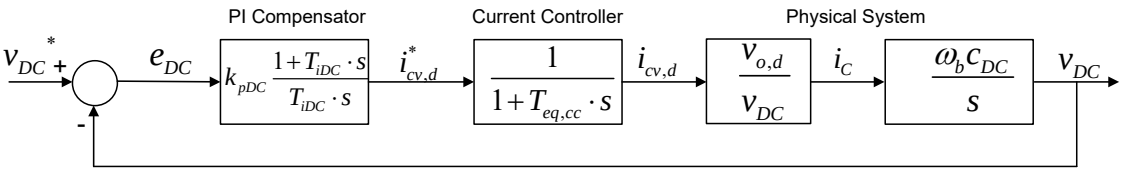

Figure 3.11: *Block diagram DC-link voltage controller*

The structure of the DC-link voltage controller further analysed is represented in Figure 3.11.

3.4.1 PI Compensator

The PI controller processes the error of dc voltage that comes from the comparison $e_{dc} = v^*_{dc} - v_{dc}$ and provide the d-frame converter current reference $i^*_{cv,d}$.

The representative equation of the PI compensator is:

$$K_{dcc}(s) = k_{pdc} + \frac{k_{idc}}{s} = k_{pdc} \cdot \frac{1 + T_{idc} \cdot s}{T_{idc} \cdot s}, \quad where \quad T_{idc} = \frac{k_{pdc}}{k_{idc}} \tag{3.51}$$

The parameters k_{pdc} and T_{idc} are defined as the proportional gain and integral time constant, respectively. These two quantities are the design parameters to be specified through the tuning of the compensator.

For tuning the parameters of the outer-loop dc-link voltage controller, the time constant $T_{eq,cc}$, representing the closed loop current controller, must be considered.

3.4.2 Physical Circuit

There are different method to find out the transfer function of the physical system. The most common methods used are the "Energy Balance" and "Power Balance". In this thesis, the second approach will be used, as further described. [11] [21]

In order to derive the transfer function of the DC-Link some assumption must be done. The first is to neglect the power losses in the VSC considering the equivalent average model. The second hypothesis is to represent the other converter of the two-terminal VSC-HVDC as a constant power source, represented by 3.52:

$$I_L = \frac{P}{V_{dc}}, \qquad P = const \tag{3.52}$$

After the previous assumptions, it is possible to describe the power balance equation $p_{dc} = p_{AC}$, as given by 3.53:

$$v_{dc} \cdot i_{dc} = v_d \cdot i_d + v_q \cdot i_q \tag{3.53}$$

Applying the Kirchhoff's Current Law at the node "A" in the scheme of Figure 3.3, it is possible to write the electrical system equation, as given by 3.54:

$$I_{dc} = -C\frac{dV_{dc}}{dt} + \frac{P}{V_{dc}} \tag{3.54}$$

The per unit Kirchhoff's Current Law can be obtained dividing both terms by the base current $Ib = V_b \omega_b C_b$, as represented in 3.55

$$i_{dc} = -\frac{1}{\omega_b c_{dc}} \cdot \frac{dv_{dc}}{dt} + \frac{P}{v_{dc}} \tag{3.55}$$

Substituting the result obtained in 3.53, it is possible to derive the non-linear state-space equation that describes the physical system of the DC-Link, as given by 3.56:

$$\frac{1}{\omega_b c_{dc}} \cdot \frac{dv_{dc}}{dt} = \frac{v_d \cdot i_d + v_q \cdot i_q - P}{v_{dc}} \tag{3.56}$$

To analyse the stability of a non-linear system around the steady-state operating point, the system must be linearised. Hence, the Taylor's Series Expansion around the steady-state operating point is applied according to the general expression shown in 3.57.

$$\frac{dx}{dt} = f(x,y,z) \Rightarrow \frac{\Delta x}{dt} = \frac{\partial f}{\partial x}\bigg|_{y=y_0}^{z=z_0} \cdot \Delta x + \frac{\partial f}{\partial y}\bigg|_{x=x_0}^{z=z_0} \cdot \Delta y + \frac{\partial f}{\partial z}\bigg|_{x=x_0}^{y=y_0} \cdot \Delta z \tag{3.57}$$

The reference point for the linearization is selected by specifying reference input v_{dc}^* for the non-linear model. Consequently, the linearized form of the dc-link equation around the stationary system operating point is:

$$\begin{aligned} \frac{1}{\omega_b c_{dc}} \cdot \frac{\Delta v_{dc}}{dt} = {} & \frac{v_{d0}}{v_{dc0}} \Delta i_d + \frac{i_{d0}}{v_{dc0}} \Delta v_d - \frac{v_{d0} i_{d0}}{v_{dc0}^2} \Delta v_{dc} \\ & + \frac{v_{q0}}{v_{dc0}} \Delta i_q + \frac{i_{q0}}{v_{dc0}} \Delta v_q - \frac{v_{q0} i_{q0}}{v_{dc0}^2} \Delta v_{dc} \\ & + \frac{P}{v_{dc0}^2} \Delta v_{dc} \end{aligned} \tag{3.58}$$

At this point, several terms of the Equation 3.58 can be simplified or neglected. Firstly, the terms multiplied by v_{q0} are equal to zero. Secondly, the term $\frac{i_{q0}}{v_{dc0}} \Delta v_q$ is almost zero, so it will be neglected. As a result, the Equation 3.59 can be rewrite.

$$\frac{1}{\omega_b c_{dc}} \cdot \frac{\Delta v_{dc}}{dt} = \frac{v_{d0}}{v_{dc0}} \Delta i_d + \frac{i_{d0}}{v_{dc0}} \Delta v_d + \frac{P - v_{d0} i_{d0}}{v_{dc}^2} \Delta v_{dc} \tag{3.59}$$

It can be notice from the 3.59 that the last term coincides to zero by definition, since the HVDC link does not store energy during the state-state operation. Moreover, in the Equation 3.59 Δv_{dc} is the state variable and Δi_d is the control input, while the input Δv_d can be considered as a

disturbance. Therefore, the simplified equation is:

$$\frac{1}{\omega_b c_{dc}} \cdot \frac{\Delta v_{dc}}{dt} = \frac{v_{d0}}{v_{dc0}} \Delta i_d \tag{3.60}$$

3.4.3 Tuning Criterion

Applying the Laplace Transform to 3.60, the open loop transfer function of the DC-link voltage control can be derived, as given by

$$h_{OL,dc}(s) = \frac{\Delta v_{dc}}{i_d} = k_{pdc} \cdot \frac{1 + T_{idc} \cdot s}{T_{idc} \cdot s} \cdot \frac{1}{1 + T_{eq,cc} \cdot s} \cdot \frac{\omega_b c_{dc}}{s} \tag{3.61}$$

It can be easily state that the plant is not stable due to the pole in the origin. The system is stabilized by the PI compensator.

Based on the open loop transfer function 3.47, the closed loop transfer function can be written as given by Equation 3.62:

$$h_{CL,dc}(s) = \frac{h_{OL,dc}(s)}{1 + h_{OL,dc}(s)} \tag{3.62}$$

As it has been described in the section 3.3, the tuning of the PI compensator for the DC-Link voltage controller follows the same criterion (i.e. SO). As a result, the PI controller gains are expressed according to

$$k_{pdc} \approx \frac{T_{dc}}{a \cdot T_{eq,cc}}, \quad k_{idc} \approx \frac{T_{dc}}{a^3 \cdot T_{eq,cc}} \tag{3.63}$$

where

$$T_{dc} = \frac{1}{c_{dc} \cdot \omega_b} \tag{3.64}$$

Although simple to design and implement, a cascade control system is likely to respond to changes more slowly than a control system where all the system variables are processed and acted upon simultaneously. As a consequence, the feed-forward is used to minimize disadvantage of slow dynamic response of cascade control. As the reference values of the inner loop variables are often available, these are fed forward for a faster and safe operation.

Using the feed-forward, the load variation and the large gain of voltage controller can be greatly reduced. Otherwise, the gain should be enough to reduce the large error. This advantages are important from the stability viewpoint.

The DC-link voltage controller governs the capacitor current so as to maintain the power balance. Hence, under balanced condition the current that flow into the capacitance is equal to

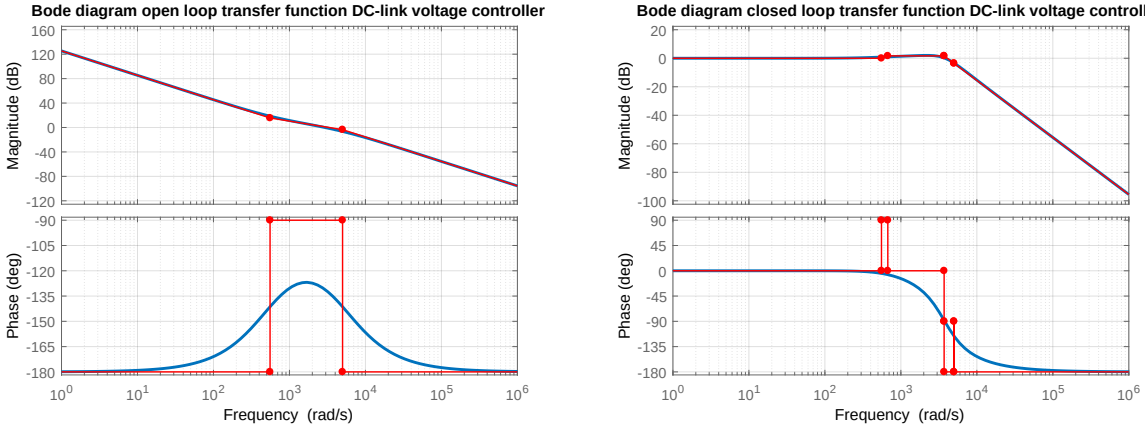

Figure 3.12: *Bode diagram outer loop DC voltage controller - Open and closed loop transfer function, left and right chart respectively. The red lines represent the asymptotic approximation of the frequency response marking the poles and zeros with dots, while the blue lines are the actual frequency response.*

zero. Consequently, the Equation 3.55 can be simplified as:

$$i_d = \frac{v_{dc}}{v_d} \cdot i_L \tag{3.65}$$

The Bode diagrams representing the magnitude in decibel (dB) and phase in degrees (deg) of the open and closed loop transfer functions, shown in Equation 3.61 and 3.62, have been presented in the Figure 3.12.

3.5 Tuning of VSM inertia emulation controller

The VSM implementation investigated in this thesis is based on a conventional swing equation representing the inertia and the damping of a traditional SM. The block diagram of the under analysis functional element is shown on the right side of Figure 2.4.

The tuning of VSM inertia emulation consists in the selection of the parameters that describes this fundamental block. The mechanical time constant T_a has been selected considering an intermediate inertia representative for a distributed generation unit [1] [18], which corresponds to 2 s. While, the damping constant k_d has been set up with the aim of reducing the virtual mechanical oscillation of the VSM. In order to exploit the maximum efficiency of the VSM, a variation of the damping factor has been tested to analyse how the change in loading of the converter is influenced by this parameter.

The proposed idea have been conducted by simulation in *DIgSILENT - Power Factory*,

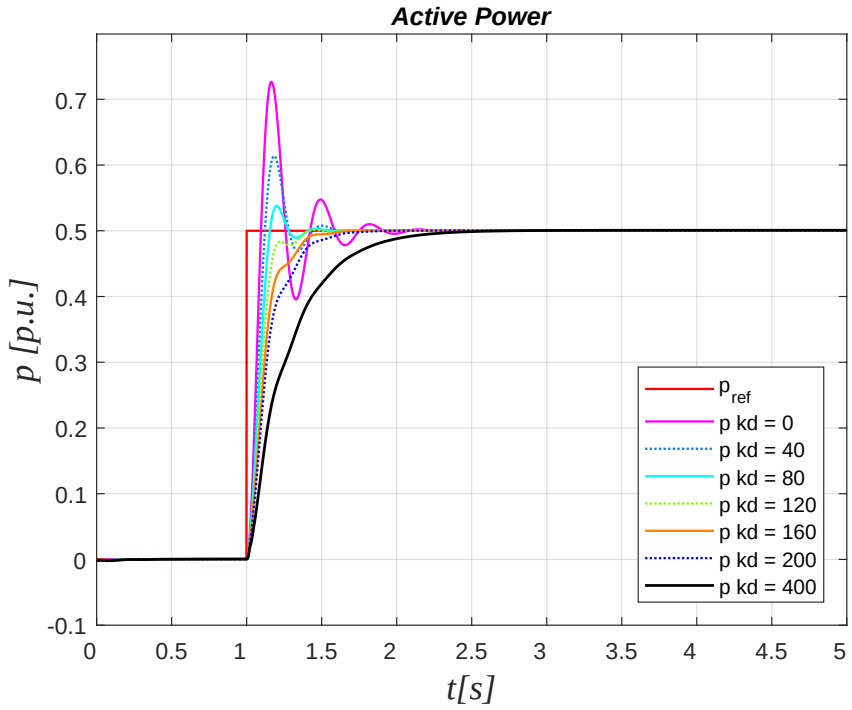

Figure 3.13: *Response of VSM to a step in the power reference input varying the damping factor* k_d

which is complementary to *Simulink* as it is explained in chapter 4. In particular, in the simulated case, the dynamic response of the system is examined for a step in power reference input to the VSM from 0.0 pu to 0.5 pu when the grid frequency and the reference frequency are both equal to 1.0 pu. This case is equivalent to a sudden increase in the input power or torque on the shaft of a SM connected to an infinite bus.

The variation of the active damping factor k_d has been done sweeping the value from zero up to 400. The most meaningful values have been plotted in graphs. In order to highlight how the performance of the VSC-HVDC changes, the active power and the frequency, as given by Figure 3.13 and 3.14.

The power reference and the resulting electrical power from the VSM are plotted in Figure 3.13, where it is shown that the VSM with the selected parameters exhibits different behaviour as a function of the damping factor gain k_d. An oscillatory with a high overshoot response distinguishes the simulation with low or nil value of damping factor, whereas a smooth transient response without any overshoot is obtained using a damping factor of 400. It should be noted that increasing the value of k_d the time to reach the steady state conditions increase while the overshoot is smoothed.

The step change in the reference of active power triggers also a dynamic response in the rotat-

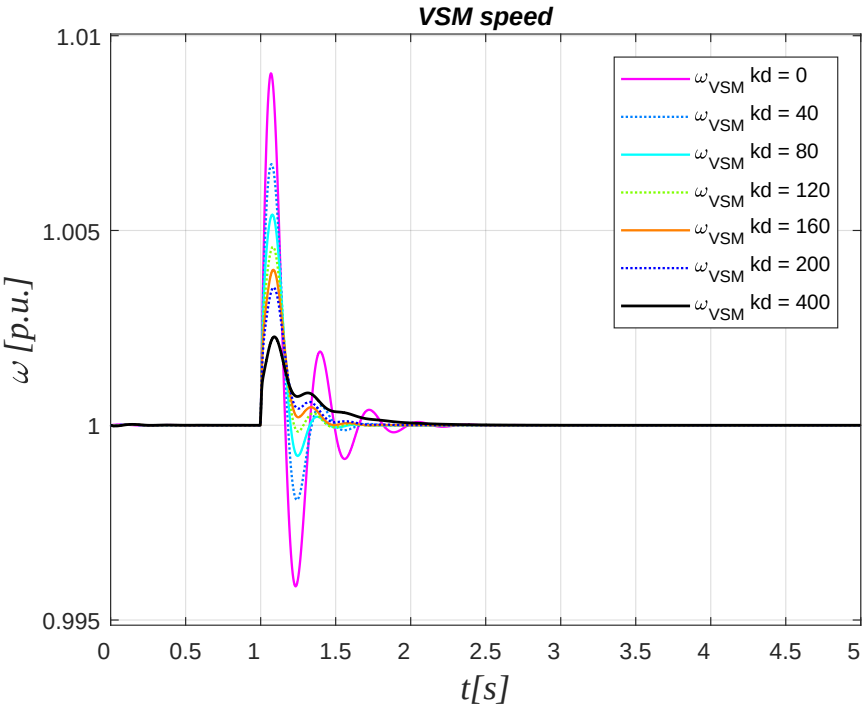

Figure 3.14: *Response of the VSM speed to a step in the power reference input varying the damping factor k_d*

ing speed of the virtual inertia, as shown in Figure 3.14. Indeed, the excess "mechanical" power input is accumulated in the virtual inertia of the VSM, resulting in increasing the speed during the first part of the transient. Of course, the damping factor influences heavily the characteristic of the step response. In other words, the simulations with low or nil value of k_d exhibits a oscillatory behaviour, which would not be tolerable by a SM since it would cause mechanical stress at the shaft of the machine. From the virtual synchronous machine point of view, the mechanical stress at the shaft does not exist being the mechanical power virtual. However, the VSM is usually connected to a power system composed by real SM, which have a real shaft. Consequently, the SM may not tolerate the oscillation introduced by the VSM.

The transient behaviour shown in the presented curves exhibits the same general characteristics as for a conventional SM, but with a less or more damped response as a function of the damping coefficient k_d. Indeed, the VSM replicates the behaviour of a classical SM, but its parameters do not have to comply with any physical constraint. Thus, the parameters of the VSM can be selected with more freedom, without considering any efficiency aspects. In particular, power losses due to the damping effects of the VSM appear only in the control system and not in the physical circuit.

3.6 Tuning of active, reactive power and AC voltage droop controllers

The droop regulation techniques implemented for controlling the power electronics converters govern the exchange of active and reactive powers with the grid, in order to keep the grid voltage frequency and amplitude under control. The main idea to support the droop controls is to emulate the self-regulation capability if the synchronous generator in grid-connection mode, decreasing the injected active power when the frequency of the grid increased and decreasing the delivered reactive power when the grid voltage amplitude increases.

Considering the VSC-HVDC converter as an ideal controllable voltage source, i.e. neglecting the switching effects, that is connected to AC grid through a given line impedance represented by the series parameters R_g and L_g, as shown by Figure 3.3, the active and reactive powers, P and Q respectively, that it will inject into the grid can be defined by Equation 3.66 and 3.67:

$$P = \frac{V_0}{R_g^2 + X_g^2} \cdot [R_g(V_0 - V_g \cdot \cos\delta) + X_g \cdot V_g \cdot \sin\delta] \tag{3.66}$$

$$Q = \frac{V_0}{R_g^2 + X_g^2} \cdot [-R_g \cdot V_g \cdot \sin\delta + X_g(V_0 - V_g \cdot \cos\delta)] \tag{3.67}$$

The angle δ corresponds to the phase-angle difference between the two voltages V_0 and V_g. While, $Z_g = R_g + jX_g$ is the interconnection line impedance and ϕ is the impedance angle. As $R_g = Z_g \cdot \cos\phi$ and $X_g = Z_g \cdot \sin\phi$, the performance of this simplified electrical system can be depicted by its vector representation, as shown in Figure 3.15 It should be noted that the

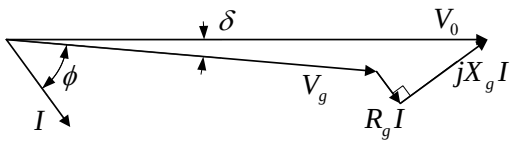

Figure 3.15: *Phasor diagram of a simplified model of power converter connection to a grid*

inductive component of the line impedance in the high voltage network is typically much higher the resistive one [13] [4]. In particular, in the power network under analysis the ratio $X/R \approx 10$. Therefore, the resistive part can be neglected without making any significant error. In addition, the power angle δ is such lines is small, so it can be assumed that $\sin\delta \approx \delta$ and $\cos\delta \approx 1$.

Consequently, Equation 3.66 and 3.67 can be rewritten as:

$$P \approx \frac{V_0}{X_g}(V_g \cdot \sin\delta) \rightarrow \delta \approx \frac{X_g P}{V_0 V_g} \tag{3.68}$$

$$Q \approx \frac{V_0}{X_g}(V_0 - V_g \cdot \cos\delta) \rightarrow V_0 - V_g \approx \frac{X_g Q}{V_0} \tag{3.69}$$

Equation 3.68 and 3.69 show a direct relationship between the power angle δ and the active power P, as well as between the voltage difference $V_0 - V_g$ and the reactive power Q. These relationships permit regulating the grid frequency and voltage at the point of common coupling of the VSC-HVDC converter, by controlling the value of the active and reactive powers injected into the grid.

Therefore, the following droop expressions in per unit values can be derived:

$$k_\omega = \frac{\omega^* - \omega}{p - p^*} \tag{3.70}$$

$$k_q = \frac{q^* - q}{v - v^*} \tag{3.71}$$

where $\omega^* - \omega$ and $v - v^*$ represent the angular grid frequency and the voltage deviations, respectively, from their rated values. While, $p - p^*$ and $q^* - q$ are the variation of active and reactive power delivered by converter to compensate such deviations. These two relationships can be graphically represented by the droop characteristics shown in Figure 3.16, where, as stated in Equation 3.70 and 3.71, the gain of the control action in each case, i.e. the slope of the frequency and voltage droop characteristics, is set by the k_ω and $1/k_q$ parameters, respectively. Therefore, the VSC will participate to the support of the frequency and voltage regulation adjusting the active and reactive power reference according to its p/ω and q/v characteristics.

As a conclusion, the method to select the droop gain parameter k_ω and k_q is divided in two steps. Firstly, it has to select the maximum admissible deviation of frequency and voltage at the point of common coupling. In the power system analysed, it corresponds to $\pm 5\%$ for the frequency and $\pm 20\%$ for the amplitude voltage. Secondly, the correspondent active and reactive powers to counteract the deviation of the variables under control have to be selected. This selection usually coincides to the nominal value of the powers, i.e. 1 in per unit. As a consequence, the value of the droop gains correspond to:

$$k_\omega = 20 \quad \& \quad k_q = 0.2 \tag{3.72}$$

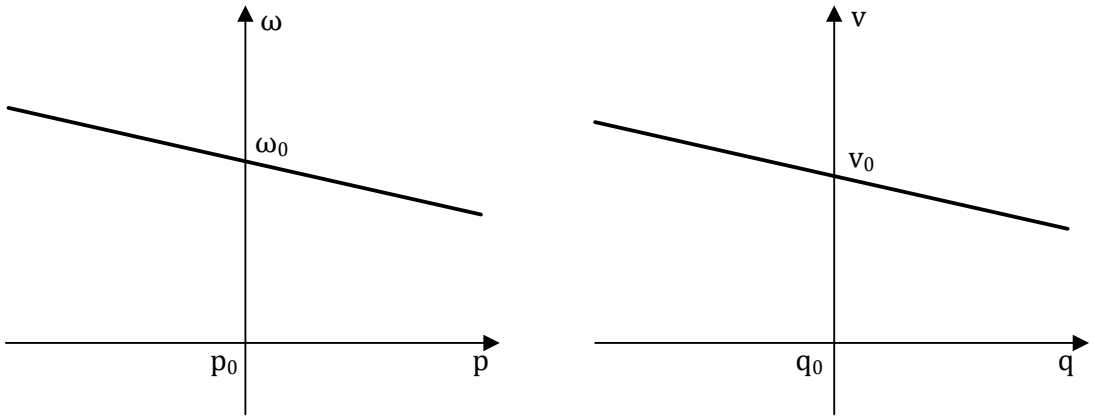

Figure 3.16: *Frequency and voltage droop characteristics in grids with dominant inductive behaviour*

Regarding the AC voltage droop controller gain parameter k_{AC}, a similar analysis can be done as well as for the reactive power droop. Considering the instantaneous reactive power at the converter terminals q presented in subsection 2.2.1 as described by Equation 2.7, it should be noted that it can be simplified considering that the PLL sets the q-frame of the voltage at the filter capacitor equal to zero. As a consequence, the reactive power flow from the converter to the grid can be determined according to:

$$q = -v_d \cdot i_q \quad \rightarrow \quad i_q = -\frac{q}{v_d} \tag{3.73}$$

Equation 3.73 shows that controlling the q-axis of the current reference it is possible to regulate the reactive power injection into the grid.

3.7 Tuning of active damping controller

The active damping controller is an additional control algorithm introduced for stabilizing the LC filter oscillations. The basic concept consists on injecting voltage or current components in counter-phase with respect to the measured oscillations. The effectively cancellation of the oscillatory components is usually obtained isolating the high frequency oscillations through high-pass filter implemented by using low-pass filter, as shown in Figure 2.9.

From the pratical point of view, the description above explained is reached through a very simple tuning of the parameters inside the fundamental block of the active damping. The two

parameters under analysis are the cut-off frequency ω_{AD} of the low-pass filter used to implement the high-pass filter and the active damping gain k_{AD}. The cut-off frequency ω_{AD} has been chosen in order to filter the fundamental frequency ω_0. In other words, the value of the cut-off frequency has been set almost 10 times smaller than the rated angular frequency of the system. While, for simplicity, the proportional gain k_{AD} has been selected equal to 1.0, which corresponds to the complete cancellation of oscillation injecting the counter-phase voltage.

3.8 Summary of parameters

The physical parameters and the quantities obtained using the tuning criteria presented are listed in Table 3.1. It can be noticed that the values of the parameters equal for both the VSCs are not characterized by any subscript.

In addition to the parameters listed in the table, it should be mentioned that the voltage of the feed-forward for the current controller is enabled in both converters while the current feed-forward for both the SRF and the DC-link voltage controllers, k_{ffi} and k_{ffiDC}, are disabled.

Chapter conclusion

In this chapter, the methods for the tuning of the HVDC control system configuration presented in chapter 2 have been described. Starting from the phase locked loop and the inner current controller loop, which are used for both the HVDC terminals, the analysis proceeds presenting the SRF and the DC-link voltage control, which provide the current references for the VSM and DC-link controlled converter, respectively. Furthermore, the selection of the parameter of the virtual synchronous machine has been analysed. Moreover, the approach used for choosing the parameters of the active power and AC-voltage droops is described. To conclude, the method for the tuning of the active damping controller is presented.

Table 3.1: *Values of the parameters for the tuning of the HVDC control system*

Parameter		Value	Parameter		Value
Rated Voltage	$V_s[kV]$	232,7	Filter inductance	$l_f[pu]$	0.08
Rated power	$S_b[MVA]$	750	Filter resistance	$r_f[pu]$	0.003
Rated angular frequency	$\omega_b[rad/s]$	2π*50	Filter capacitance	$c_f[pu]$	0.074
Grid inductance Norway	$l_{g,n}[pu]$	0.0308	Grid resistance Norway	$r_{g,n}[pu]$	9e-4
Grid inductance Europe	$l_{g,e}[pu]$	0.0133	Grid resistance Europe	$r_{g,e}[pu]$	4e-4
DC cable inductance	$l_{dc}[pu]$	0.0	DC cable capacitance	$c_{dc}/2[pu]$	2.12
DC cable resistance	$r_{dc}[pu]$	0.086	DC cable conductance	$g_{dc}/2[pu]$	1.7e-3
PLL filter	$\omega_{LP}[rad/s]$	500	PLL design constant	a_{PLL}	3
PLL proportional gain	$k_{p,PLL}[pu]$	0.084	PLL integral gain	$k_{i,PLL}[pu]$	4.69
Active damping gain	$k_{AD}[pu]$	1	Active damping filter	$\omega_{AD}[rad/s]$	50
Proportional gain c.c.	$k_{pc}[pu]$	1.27	Integral gain c.c.	$k_{ic}[pu]$	14.3
Proportional gain v.c	$k_{pv,n}[pu]$	0.59	Integral gain v.c.	$k_{iv,n}[pu]$	736
Inductance v.i.	$l_{v,n}[pu]$	0.2	Resistance v.i.	$r_{v,n}[pu]$	0.0
VSM Inertia Time	$T_{a,n}[s]$	2	VSM damping coeff.	$k_{d,n}[pu]$	400
Droop gain reac. power	$k_{q,n}[pu]$	0.2	Reactive power filter	$\omega_{f,n}[rad/s]$	1000
Proportional gain dc.c.	$k_{pDC,e}[pu]$	2.508	Integral gain dc.c.	$k_{iDC,e}[pu]$	1390.4
Droop gain AC voltage	$k_{AC,e}[pu]$	20	AC voltage filter	$\omega_{f,e}[rad/s]$	100

Chapter 4

Dynamic simulations with VSM and DC-link controlled HVDC

Chapter introduction

This chapter presents the functional behaviour of the reference control implementation by means of numerical simulation of a few relevant cases. The used dynamic model of the system coincides with the point-to-point HVDC transmission system with VSM and DC-link controlled converters. From the practical point of view, the simulations are modelled using the VSM based converter in Norway while the DC-link based VSC in Europe.

The analysed control system is initially simulated both in *Matlab* and *DIgSILENT*. In order to accomplish the task, the simulations for the comparison have been implemented considering ideal AC grid composed by voltage sources instead of synchronous generators. Successively, the simulations are conducted only in the commercial software for the system analysis *DIgSILENT*, which guarantees the study of realistic power systems.

The interest of the simulations is focused on two principal characteristics. Firstly, the response to change in loading of the VSC. Secondly, the response to change in the grid frequency because of a load step.

4.1 Dynamic response to change in loading with AC ideal voltage sources

In the first simulated case, the dynamic response of the point to point HVDC transmission system with VSM and DC-link voltage control exposed in chapter 2 is examined for a step in

active power reference input to the VSM controlled converter from 0.5 pu to 0.7 pu when the grid frequency and the reference frequency are both equal to 1.0 pu. The electrical scheme for the defined simulation scenario is shown in Figure 4.1.

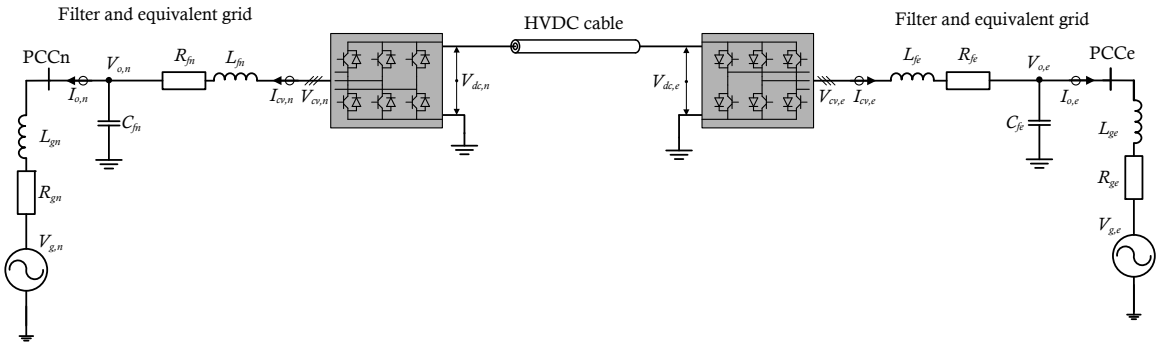

Figure 4.1: *Single-line diagram of a VSC-HVDC transmission system made up by two-level converter connected to AC voltage sources through LC filter.*

All the reference quantities in the investigated HVDC configuration have been obtained from the power flow. The approach for the setpoint selection is based on the objective to have an active power flow of 0.5 pu through the HVDC interconnector that is imposed by the VSM controlled side, i.e. Norwegian side. Moreover, the reactive power flow has been set up equal to 0.0 pu. Instead, on the European side of the HVDC, i.e. the DC-link controlled VSC, the setpoints have been decided in order to maintain the DC voltage level and the AC voltage amplitude at the DC bus and PCC, respectively, equal to 1.0 pu.

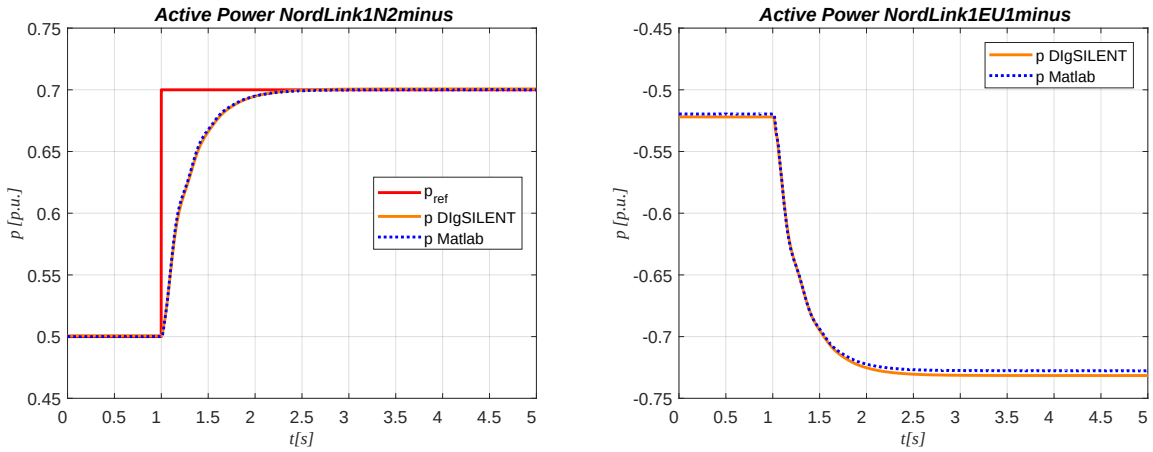

Figure 4.2: *Active power response of HVDC link connected to AC ideal voltage sources to a step in the power reference input - VSM and DC-link controlled VSC response in the left and right part, respectively*

The power reference and the resulting electrical power from the VSM controlled VSC-HVDC

are plotted in the left part of Figure 4.2, while the electrical power from the DC-link controlled converter is reported in right part of Figure 4.2. It can be easily noticed the quite reasonable matching between the simulation result from *Matlab* and *DIgSILENT*, solid orange line and dotted blue line, respectively. It is possible to notice a very tiny deviation at steady state between the two simulation software. This different is related to the modeling of *DIgSILENT*'s components, which are temperature dependent. So, increasing the power flow the thermal condition of the components have a temperature variation which bring to different steady state conditions.

The time response of the VSM controlled VSC shows that the VSM with the selected parameters exhibits a smooth transient response and reaches steady state condition in approximately 1 s without any overshoot.

Regarding the time response of the DC-link controlled VSC, the transient is very similar

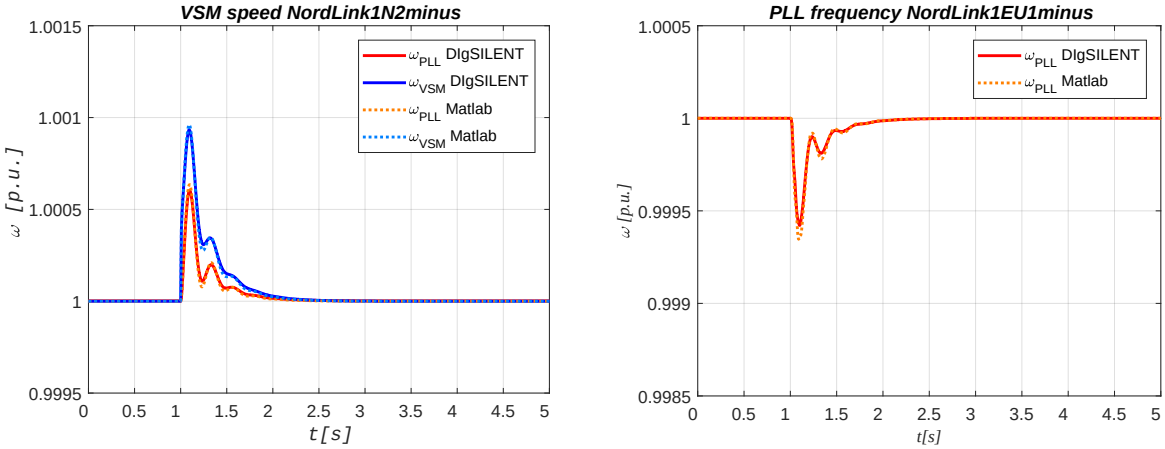

Figure 4.3: *Frequency response of HVDC link connected to AC ideal voltage sources to a step in the power reference input - VSM and DC-link controlled VSC response in the left and right part, respectively*

to the other side of the HVDC with the difference in the offset due to the copper losses in the series reactor resistance of the cable.

The step change in the reference triggers also a dynamic response in the rotating speed of the virtual inertia and in the frequency measurement in the point of common coupling of the phase locked loop, as shown in left part of Figure 4.3. The PLL for the DC-link controlled converter behaves analogously reducing its values to compensate the phase displacement introduced by the voltage drop across the equivalent series impedance of the grid model, as displayed in the right part of Figure 4.3.

It should be noted that the frequency of the grid is always equal to 1 pu even though the PLL measurement differs from this value during the transient. The deviation of the frequency

is only because of the PLL measure the voltages at the terminal of the Thévenin model of the grid and consequently the phase displacement causes a transient in the synchronization.

The left part of Figure 4.3 shows that the excess "mechanical" power input is accumulated

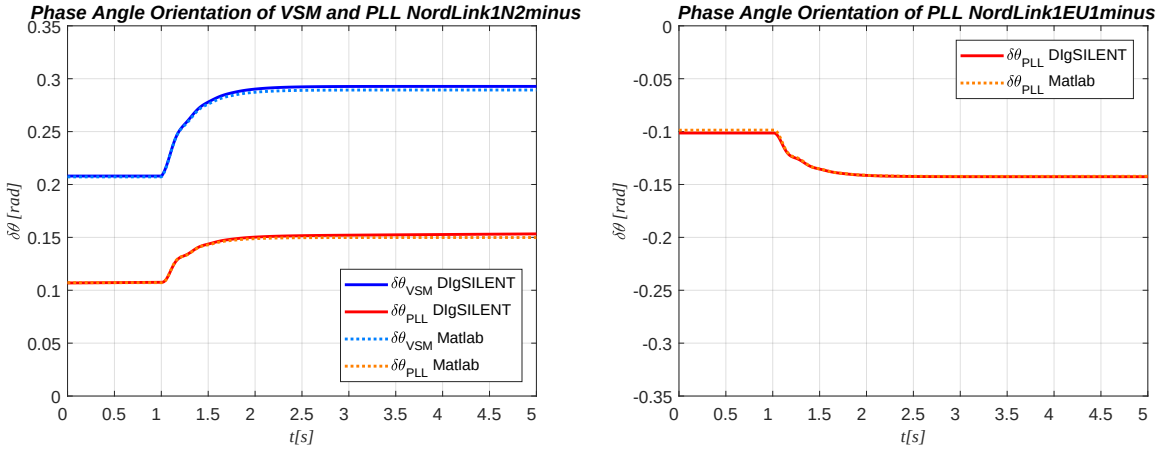

Figure 4.4: *Phase angle orientation of HVDC link connected to AC ideal voltage sources to a step in the power reference input - VSM and DC-link controlled VSC response in the left and right part, respectively*

in the virtual inertia of the VSM, resulting in an increasing speed during the first part of the transient. This leads to an increase in the phase angle between the VSM-oriented frame and the grid voltage vector as shown with the blue line in the left part of Figure 4.4, until the electrical power output from the machine balances its "mechanical" input. When the electrical power reaches the input power and the steady-state power balance of the system is restored, the rotational speed of the virtual inertia returns to the synchronous speed of the grid source, i.e. equal to 1.0 pu, just as for a traditional synchronous generator.

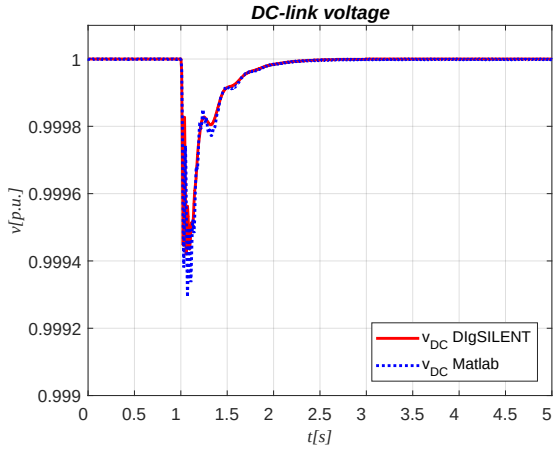

Figure 4.5: *DC voltage response of HVDC link connected to AC ideal voltage sources to a step in the power reference input*

The reference frame orientation of the PLL with respect to the grid voltage vector is shown with the red line in Figure 4.4, for the VSM and DC-link controlled VSC, respectively. The graphs illustrate how the phase angle of the voltage at the filter capacitors is changing with the power flow due to the grid impedance. However, it is noticeable how the phase angle can be considered as equivalent to the phase angle of the VSM changes more than for the PLL, due to the virtual inductance included in the VSM. Thus, the VSM phase angle can be considered as equivalent to the phase angle of the internal voltage behind the synchronous reactance of a traditional SM, while the PLL is tracking the phase angle of the voltage at the terminal of the VSM.

During the step response transient, the electrical active power injected into the grid from the VSM is firstly provided by the energy stored into the DC-link cable, which effects the voltage level across the equivalent capacitors, as shown in Figure 4.5. This voltage reduction is detected by the DC-link controlled VSC, which withdrawn power from its AC terminal to recover the DC voltage drop. It should be noted that the detection of this dynamic from the DC-link controller depends on its tuning or rather its time delay.

The presented figures include results from the simulation of the non-linear model of the VSM and DC-link controlled HVDC in *Matlab* as well as results from simulating the same events with the commercial software for power system stability analysis, so called *DIgSILENT*, in the same plot. It can be observed that all the curves indicate an excellent match between the two models. This verify the validity of the model implemented in *DIgSILENT*, and indicates that can be used for investigating the inertia support provided by the HVDC interconnector during frequency transient disturbance.

The choice to utilize *DIgSILENT* for the inertia support analysis is related to possibility of getting access of a library of a very detailed number of components and control systems for real power system application, consequently having the possibility to test the inertia support of the presented control scheme in a realist power network.

4.2 Dynamic response to change in loading with equivalent AC grids

In this simulation case, the inertia of the grid is added to the previous scenario. Therefore, the two grid frequencies are strictly related on the power balance of the system, as given by:

$$\begin{aligned} p_m - p_e &= \frac{2H}{\omega_s} \cdot \frac{d\omega_s}{dt} \\ \omega - \omega_s &= \frac{d\delta}{dt} \end{aligned} \tag{4.1}$$

In these equations p_m is the mechanical input power of the equivalent SM of the grid, p_e is the electrical power at the machine terminal, H is the inertia constant in per unit, which corresponds to half of the mechanical starting time T_a. Furthermore, ω_s is the synchronous speed of the machine in rad/s and δ is the the angular displacement of the rotor from the synchronously rotating reference axis in electrical radiant. The quantity ω is the speed of the synchronous machine and is expressed in electrical radiant per second as well as ω_s.

The electrical power system investigated in this simulation case consists of the regional power networks connected to to the *NordLink* HVDC interconnector. The choice of representing only the regional grids instead of the whole power system is given by the fact that the relevance of the simulations wil not be useful because of the huge difference in power between the entire power networks and the HVDC under analysis. In other words, the scenario that will be analysed hereafter comprises a load step of the 10% of the power absorbed by the grid. Hence, the contribution in the frequency regulation by the HVDC link would be negligible if the whole grid power was connected to the PCCs.

In this perspective, it has been decided to analyse the load step of 10% of the regional power

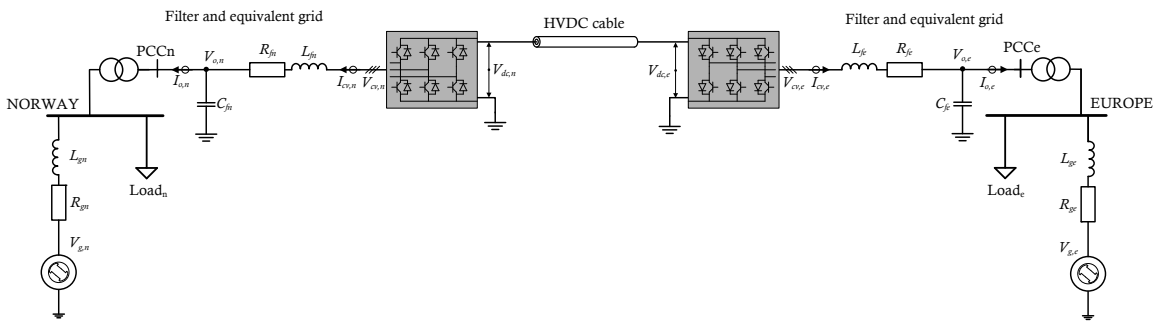

Figure 4.6: *Single-line diagram of a VSC-HVDC transmission system made up by two-level converter connected to equivalent AC grids through LC filter.*

network closest to the *NordLink* assuming that the rest of the grid does not contribute in the inertia support and frequency regulation. The idea behind this assumption is based on the fact that the rest of the grid will not detect the frequency perturbation in the first instants of the transient due to the delay of the frequency propagation, which depends on the structure of the grid. Successively, the participation of the droop will cover the inertia support contribution.

The single line diagram representing the structure of the equivalent system is shown in Figure 4.6.

The simulation scenario analysed in this section is analogous to the one analysed in section 4.1.

Table 4.1: *Parameters of the equivalent synchronous generators and step up transformers*

Synchronous generator					
Nominal power	$S_n[MVA]$	250	Nominal voltage	$V_n[kV]$	22
Power factor	$\cos\phi$	0.9	Inertia constant	$H[s]$	5
Stator reactance	$x_{st}[pu]$	0.14	Stator resistance	$r_{st}[pu]$	0.001
Transformer parameters					
Nominal power	$S_n[MVA]$	250	Nominal voltage	$V_{n1-n2}[kV]$	22/400
Series reactance	$x_{tr}[pu]$	0.06	Series resistance	$r_{tr}[pu]$	0.005
Norway			Europe		
Number of SM	N_{SG}	13	Number of SM	N_{SG}	30
Active power	$P_{SG}[MW]$	200	Active power	$P_{SG}[MW]$	200
Power factor	$\cos\phi$	0.9	Power factor	$\cos\phi$	0.9

Regarding the synchronous generators, the equivalent power for each busbar has been estimated considering the real power request of the network in a generic situation. Consequently, it has been decided to represent this scenario using an equivalent plant composed by a parallel number of SMs of realistic values. Furthermore,a dynamic model of the governors has been implemented in *DIgSILENT* using the standard model of IEEE for a traditional hydro synchronous machine, i.e. the exciters(AVR) is EXST1, the governor (GOV) consists of HYGOV and the stabilizer uses PSS2B model.

It should be noted that the number of machines chosen to be connected simultaneously influences the equivalent inertia of the power network. In other words, the instantaneous power connected to the grid is a function of the number of machines in parallel and their percentage of utilization. The variation of these two quantities have to be done with care, otherwise the dynamics of the system will change.

The resulting number of machines used in the modelling of the equivalent synchronous generators have been listed in Table 4.1:

Consequently, the loads connected to the respective busbar have been set up to withdrawn

the resultant active and reactive power injected from the SMs incremented with the power injected from the HVDC in Norway and deducted from the power withdrawn by the *NordLink* in Europe. In this way the system results stable and with constant frequencies and voltages equal to the nominal values.

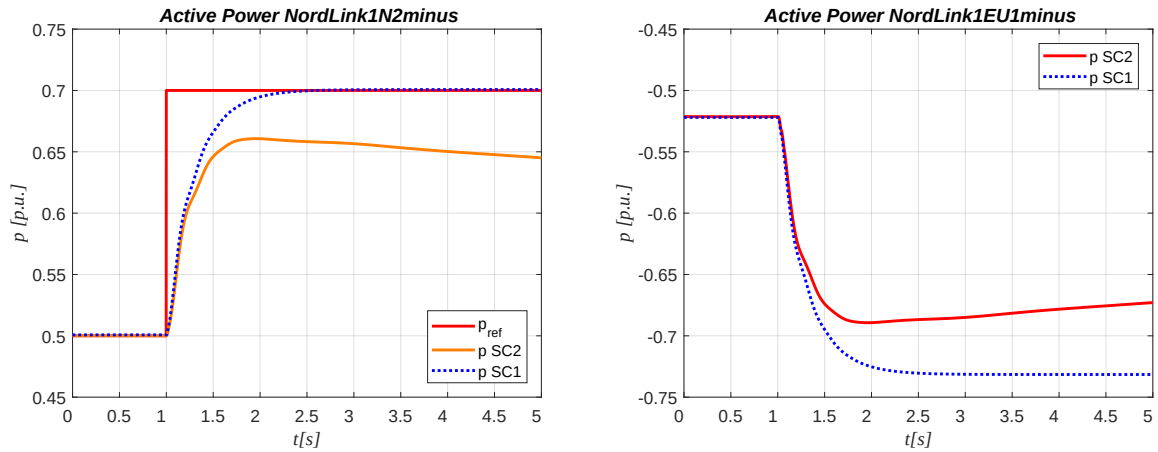

Figure 4.7: *Active power response of HVDC link connected to AC equivalent grids to a step in the power reference input - VSM and DC-link controlled VSC response in the left and right part, respectively*

The presented analysis is intended to complement the studies of the same control system connected to AC ideal voltage sources from section 4.1. Thus, together these studies should provide a comprehensive analysis of the functional behaviour and dynamic characteristics of the investigated HVDC scheme in both ideal and realistic grid connected operation. For this reason, the main system parameters used for the simulations and numerical analysis, as listed in Table 3.1 and described in section 4.1, are maintained the same.

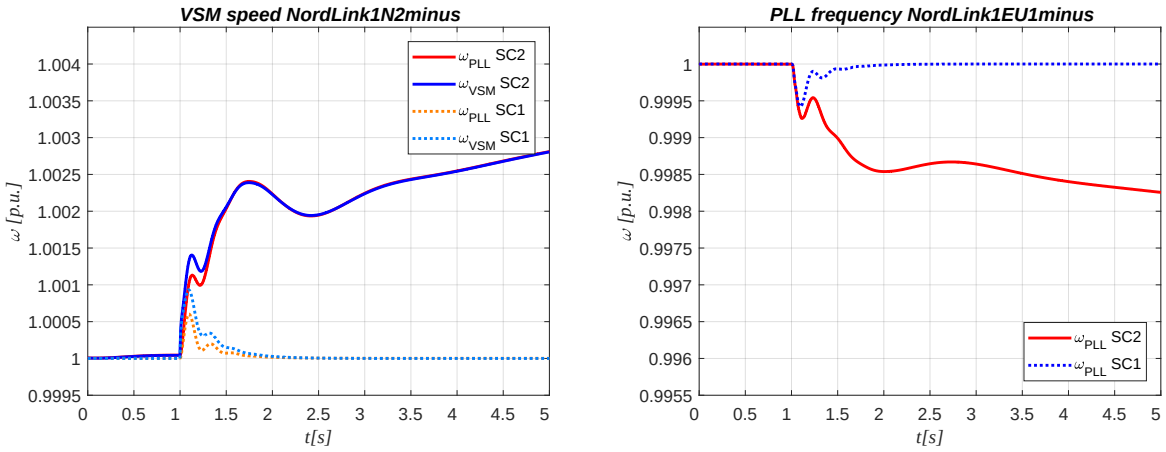

Figure 4.8: *Frequency response of HVDC link connected to AC equivalent grids to a step in the power reference input - VSM and DC-link controlled VSC response in the left and right part, respectively*

For the sake of clarity, the simulation results of the previous scenario are reported again to highlight the comparison between the two simulation cases.

The power response of the VSM and DC-link controlled VSC are shown in Figure 4.7, left and right part respectively.

It can be noticed that the power response of the actual study case (SC2) differs from the one in the ideal scenario due to the action of the droop. In other words, the increasing electrical power injected into the grid causes a frequency variation which trigger the droop intervention. The dynamic described can be appreciated in the left part of Figure 4.8.

The frequency response of the VSM controlled VSC shows how the "mechanical" power

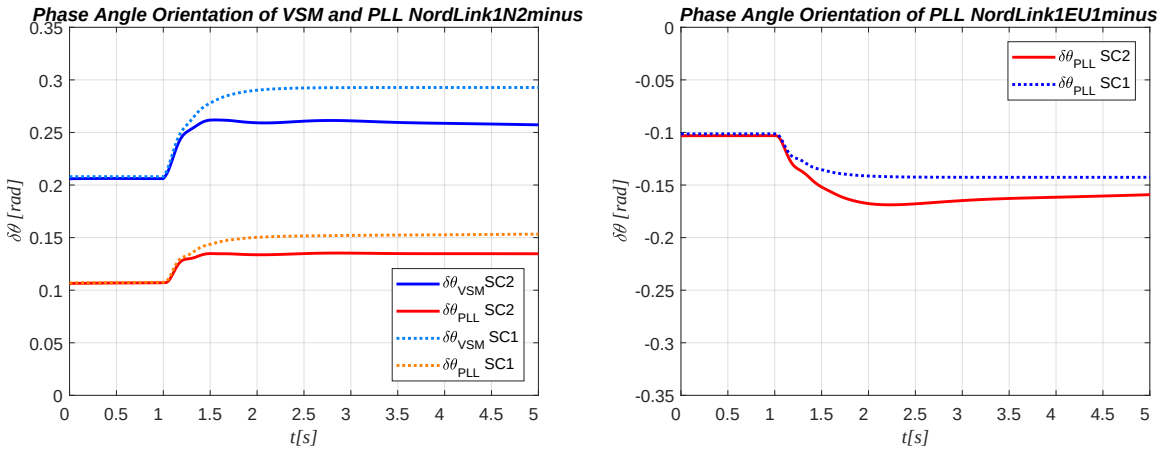

Figure 4.9: *Phase angle orientation of HVDC link connected to AC equivalent grids to a step in the power reference input - VSM and DC-link controlled VSC response in the left and right part, respectively*

input is still accumulated in the virtual inertia of the VSM, resulting in an increasing speed during the first part of the transient. As previously described, this leads to an increase in the phase angle between the VSM-oriented frame and the grid voltage vector as shown with the blue line in the left part of Figure 4.9, until the power balance at the virtual shaft of the VSM is restored. It should be noted that the angle does not reach a steady state condition because of the ongoing frequency variation, which maintains the droop modifying the power balance.

The left part of Figure 4.8 shows how the power response of the DC-link controlled converter effects a frequency perturbation in the Continental power network. It should be noted that the deviation of frequency in Europe is smaller than in, Norway because of the higher number of parallel machine connected, which influences the total inertia constant of the grid.

Regarding the phase angle orientation, the response of the second study case differs from the first scenario because of both the droop intervention of the VSM as well as for the power

response and the droop response of the equivalent SG. In other words, the deviation of the phase angle orientation of the PLL depends on the droop response of the grid SM, while the deviation of the difference between the phase angle orientation of the VSM and the PLL is caused by the droop intervention of the VSM.

Analogously as before, during the transient the electrical power injected is withdrawn from the DC cable, which provides its own energy stored inside the equivalent capacitors. The results is a decreasing of the voltage level until the DC-link voltage controlled VSC detects the difference with respect to the voltage reference, as shown in Figure 4.10.

The presented simulation scenario has verified the similarities in the analysis of the VSM

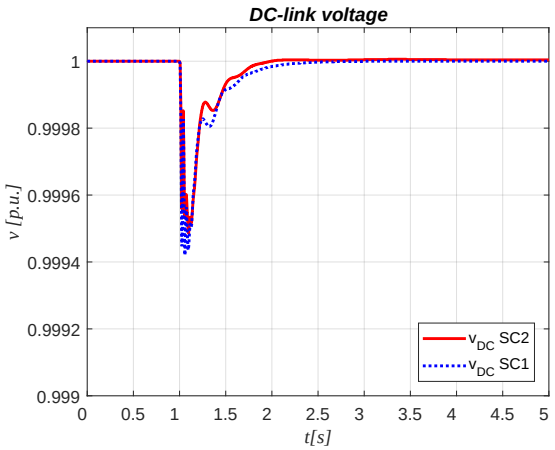

Figure 4.10: *DC voltage response of HVDC link connected to AC equivalent grids to a step in the power reference input*

and DC-link controlled HVDC connected to an ideal and a realistic model of the grid. The model validation permits to investigate the inertia support during a load step, which requires the modelling of the grid composed by equivalent SG, as described before.

4.3 Dynamic response to load step with equivalent AC grids

In this section, the inertia support of the HVDC interconnector is evaluated during a frequency transient perturbation caused by a load step in the Nordic power system.

As previously introduced, it has been decided to analyse the load step of 10% of the regional power network closest to the *NordLink* assuming the rest of the grid does not contribute in the inertia support and frequency regulation.

The load step in the Nordic network, which occurs at the time 1 second, increases the electrical power absorbed by the grid and consequently the power balance in Equation 4.1 will result

in a decreasing of frequency, as represented in the left part of Figure 4.11. In the figure, the frequency responses with and without inertia have been represented in order to highlight the improved performances guaranteed by the analysed implementation.

It should be noted, how the frequency transient response without the inertia support reaches

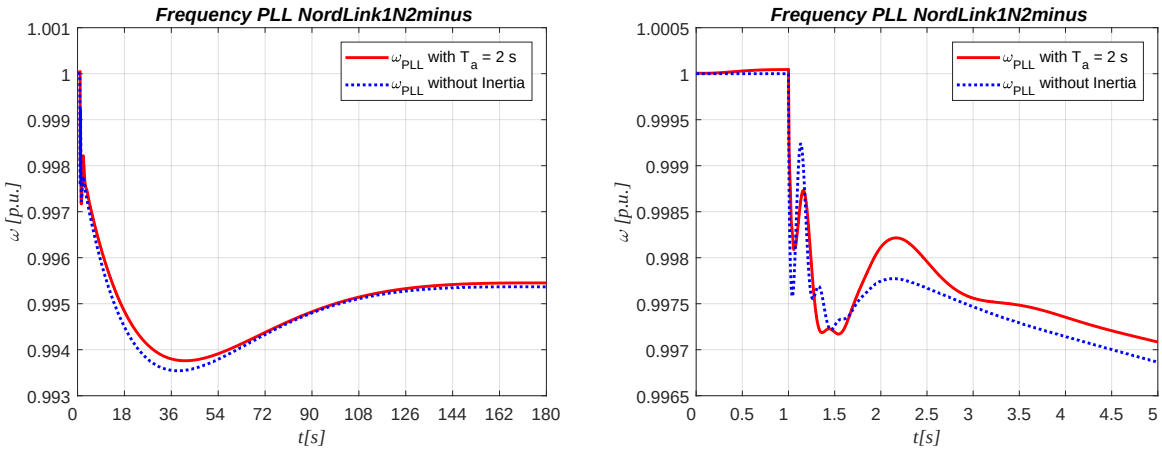

Figure 4.11: *Nordic frequency response of HVDC link connected to AC equivalent grids to a load step of 10% in the Nordic grid*

a lower *NADIR* than the scenarios with inertia. In principle, the inertia guarantees a support in the first instants that permits the droop to act and consequently to stabilize the frequency deviation. In other words, the inertia support gives the possibility to buy time for the droop action and improve the *NADIR* which could cause the triggering of the protections.

The right part of Figure 4.11 represents the zoom of the frequency response which gives a

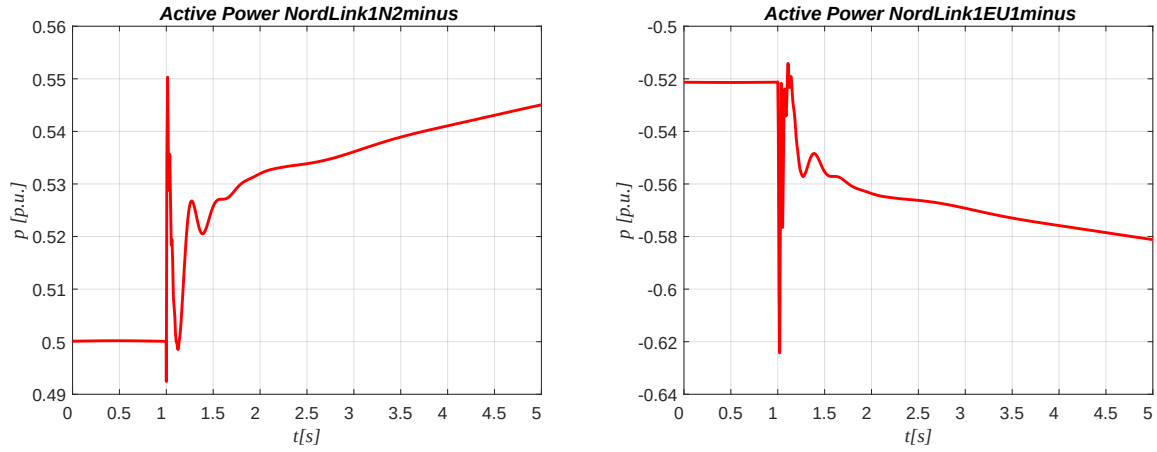

Figure 4.12: *Active power response of HVDC link connected to AC equivalent grids to a load step of 10% in the Nordic grid - VSM and DC-link controlled VSC response in the left and right part, respectively*

better understanding of the inertia dynamics. The graph shows the frequency measured by the

PLL at the point of common coupling, which detects the phase displacement introduced by the changing of the load flow during the load step. The phase displacement caused by the transformer series impedance produces an adjustment of the PLL frequency that can be appreciated in the first minimum around time 1.1 second. Successively, the frequency transient presents a second minimum due to the inertia support which reduce the rate of change of frequency (RoCoF). It should be noted that the simulation with inertia improve the frequency transient.

The frequency variation triggers the dynamic of the VSM inertia block, which reacts inject-

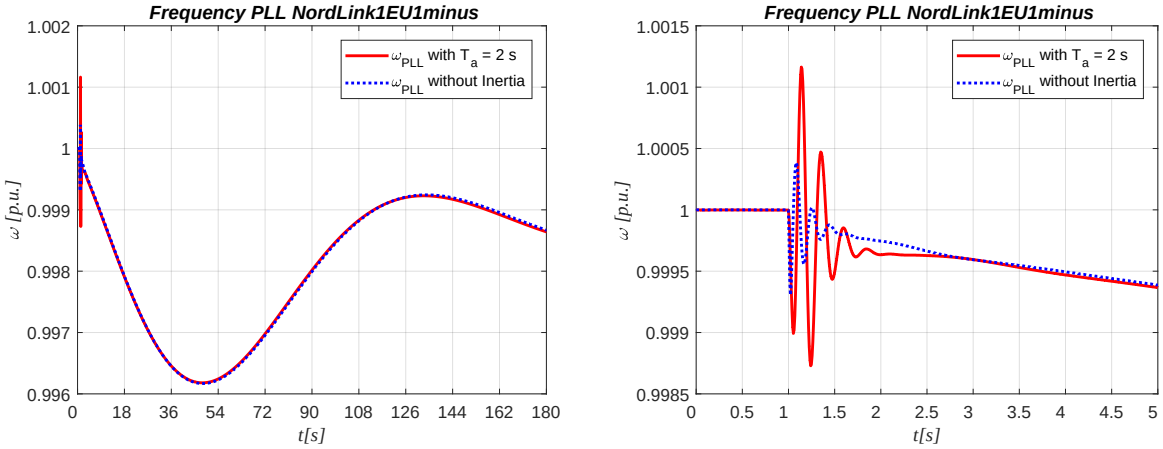

Figure 4.13: *European frequency response of HVDC link connected to AC equivalent grids to a load step of 10% in the Nordic grid*

ing the power as a function of the energy stored in the virtual shaft of the virtual synchronous machine and successively increasing the "mechanical" power thanks to the droop control. The left part of Figure 4.12 shows clearly the different contributions in the transient response. At the beginning, the power injection is caused by the damping contribution highlighted in Equation 2.12, which depends on the difference between the frequency of the VSM and the PLL estimation. Successively, the inertia support can be appreciated in the second power injection at time 1.4 second. At the end, the power constantly increase due to the droop action which is proportional to the frequency deviation.

It should be noted that the energy stored in the virtual shaft of the VSM coincides, from the physical view point, to the energy stored in the DC cable. Of course, it is not possible to exploit completely the energy of the equivalent capacitance of the cable, otherwise the overmodulation occurs. As a conclusion, it should be taken into account that the voltage of the DC-link at the VSM converter terminals must be always higher than two times the amplitude at the AC side.

In order to avoid the overmodulation, the DC-link controlled VSC should react quickly. The fast response of DC voltage control compromises the frequency in the other side of the HVDC

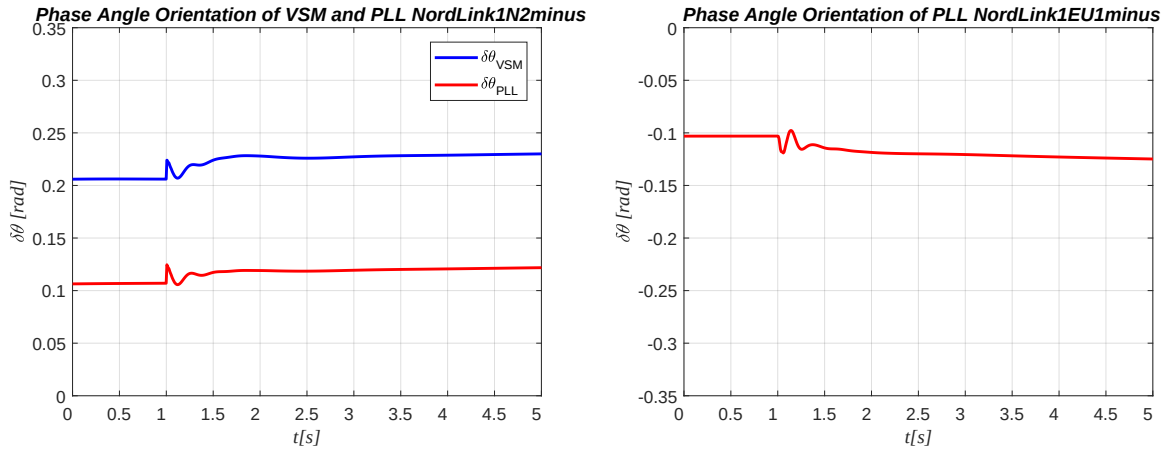

Figure 4.14: *Phase angle orientation of HVDC link connected to AC equivalent grids to a load step of 10% in the Nordic grid - VSM and DC-link controlled VSC response in the left and right part, respectively*

interconnector causing a propagation of the frequency transient disturbance, as shown in Figure 4.13.

In this study case, the importance of the tuning of DC-link control is evident. Indeed, the selection of the time response of the PI controller used influences deeply the behaviour of the frequency propagation through the HVDC interconnector.

In this thesis, the fastest tuning for the DC-link control has been presented. However, fur-

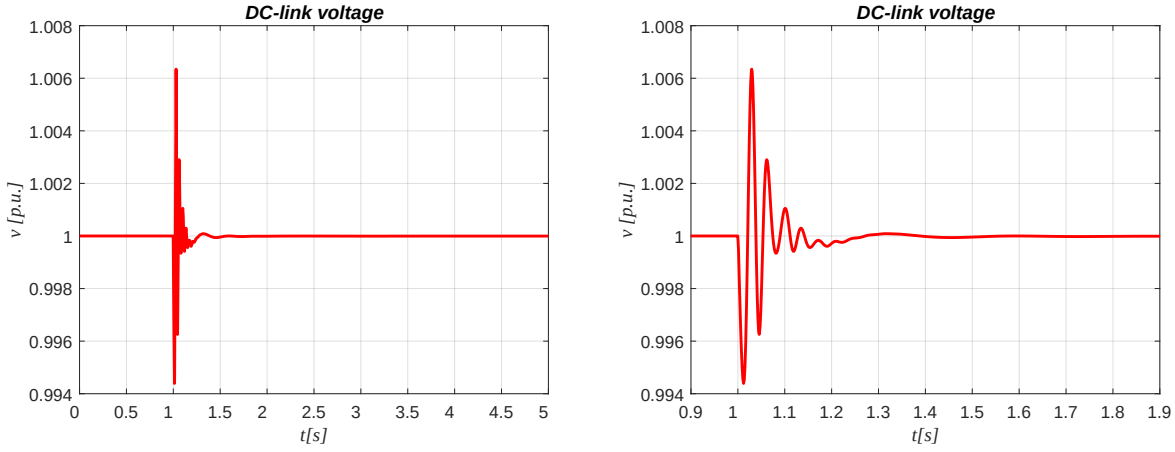

Figure 4.15: *DC voltage response of HVDC link connected to AC equivalent grids to a load step of 10% in the Nordic grid*

ther analysis should be considered to reduce the frequency propagation without occurring in the overmodulation phenomenon.

Figure 4.14 shows the phase angle orientation of the VSM and PLL for the Nordic converter and the PLL phase orientation for the DC-link controlled VSC. From the graphs, the inertia and

droop action can be appreciated. In fact, the first part of the transient response, from 1 to 1.5 s, consists of the damping and inertia support phase angle displacement, which is characterized by an acceleration that causes the increasing of the phase angle orientation. Around the time 1.5 s the inertia transient response has ended and the increasing of the phase angle displacement is because of the frequency droop.

The transient response of the capacitor voltage at the DC-link controlled VSC terminals is presented in Figure 4.15. The fast tuning of the control causes the oscillation in the DC voltage response.

4.3.1 Inertia constant and damping coefficient sensitivity

In this paragraph, the sensitivity at the variation of the inertia constant and the damping coefficient is analysed. The investigation is developed for the scenario of load step since it is the most suitable to understand the inertia support provided by the HVDC system.

Previously, the set-up of the system for the simulation has been explained and the results have been represented and described in detail. In order to understand the sensitivity in the inertia support of the above cited parameters, a set of results is shown considering different selection of inertia time constant T_a and damping coefficient k_d. Furthermore, the results are commented and some considerations are presented.

It should be noted that the frequency droop has been disabled for these simulations since the objective of the treatise is highlighting the sensitivity of the inertia constant in the transient response.

Damping Coefficient

Section 3.5 shows how the damping coefficient influences the dynamics of the VSM for a step in the active power reference input. At the end of the treatise, the value selected was equal to 400 according to the request of obtaining a very smoothed response. However, the high value selected of damping does not exploit completely the powerful of the implementation for inertia support applications.

As a consequence, it has been decided to decrease the damping coefficient up to the minimum value which does not cause a overshoot higher than 5%. The value of damping coefficient that respects this restriction corresponds to 80.

Inertia time constant

In the previous chapter, it has been explained that the selection of the mechanical time constant T_a has been done considering an intermediate inertia representative for a distributed generation unit, which corresponds to 2 s. In particular, this selection has been used to compare the performances of the VSM implementation already presented in [12] and [20] . However, in this thesis the application of the VSM controlled converter is slightly different, so a higher value of mechanical time constant could be more suitable.

In this section different values of inertia constant are analysed. Moreover, the performances are described and compared.

The load step of 10% of the Nordic grid has been simulated, as well as section 4.3. In

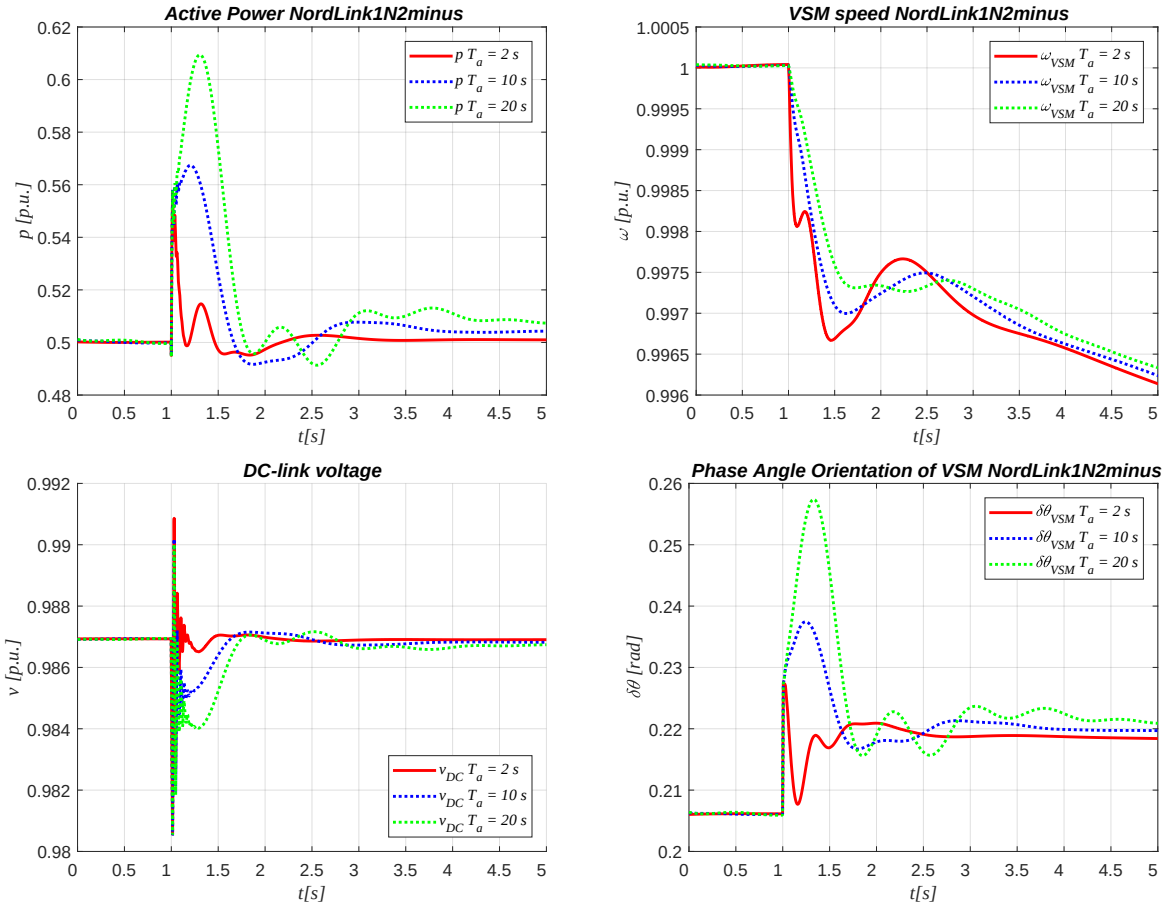

Figure 4.16: *Response of active power of VSM connected to AC equivalent grids to a load step of 10% varying the mechanical time constant T_a*

particular, the dynamic response of the VSM controlled converter has been depicted varying the mechanical time constant among three different values. Figure 4.16 shows the frequency transient zoom of the first seconds in order to highlight the inertia support behaviour.

The active power chart portrays the different power injection as a function of the inertia constant of the VSM. Indeed, the power injection is proportional to the mechanical time constant T_a and it corresponds to the energy stored in the virtual shaft of the VSM, which corresponds to the energy stored in the DC cable. Hence, the voltage across the equivalent DC capacitor decreases until the DC-link controlled converter reacts, as shown in the lower left part of Figure 4.16.

The power injection provided by the VSM into the grid improves the frequency dynamic guaranteeing a reduction of the rate of change of frequency, which improves the position of the first minimum mainly characterized by the inertia of the system, as shown in the higher right part of Figure 4.16. Successively, the frequency transient is influenced by the droop response of the whole system. It should be noted that a high value of inertia constant permits the governor of the traditional synchronous generator to detect the transient disturbance starting from a better situation that a scenario without inertia.

As a conclusion, the inertia of the system would not modify the *NADIR* if the SMs did not have any frequency droop controller. Conversely, the inertia support provides a deceleration of the frequency transient disturbance which guarantees the slower controller, i.e. the frequency droop controller, to reach to the perturbation.

Chapter conclusion

The dynamic simulations of the VSM and DC-link controlled HVDC transmission system have been presented in this chapter. The dynamic response to change in loading of the VSM controlled converter with AC ideal grid model has been analysed both in *Matlab* and *DIgSILENT*. It has been verified the equivalence of the two models.

Successively, the model of the grid has been changed to a realistic scenario with inertia. The dynamic response for a step in active power reference input to the VSM controlled converter has been studied and the analogies with the previous scenario have been described.

Finally, the dynamic response to a load step in the power network connected to the VSM has been proposed and scenarios with different inertia situation have been compared.

Chapter 5

HVDC interconnector with two VSM controlled converters

Chapter introduction

In this chapter an innovative control system implementation for HVDC transmission system is proposed. The overview of the control schemes for the selected power electronics converters used at the two terminals of the DC-link is presented. Furthermore, the main differences with respect to the control scheme described in chapter 2 are empathized. Successively, the small signal model used for studying the stability of the implementation is described. At the end, the dynamic operation of the control scheme are compared with respect to the result obtained in chapter 4.

5.1 Control scheme of HVDC with two VSMs

This section presents an innovative control scheme implementation for the selected HVDC link described in section 2.1.

The selected implementation is composed by a VSM for each side of the HVDC interconnector. As well as before, the control scheme is based on an internal representation of the SM inertia and damping behaviour through a reduced order swing equation, together with cascaded voltage and current controllers for operating a VSC. Moreover, the reactive power control has been implemented to control the AC side voltage.

The utilization of VSM in both sides of the HVDC permits to contribute in frequency transient disturbance with the inertia support not only in one side of the interconnector. However, the

emulation of inertia and damping effects requires an energy buffer with sufficient capacity to represent the energy storage effect to the emulated rotating inertia available. Thus, the amount of virtual inertia that can be added to the system by a single VSM unit will be by the DC-side configuration and by the current rating of the converter.

As already explained, the DC-link voltage level is one of the limitation for the inertia support

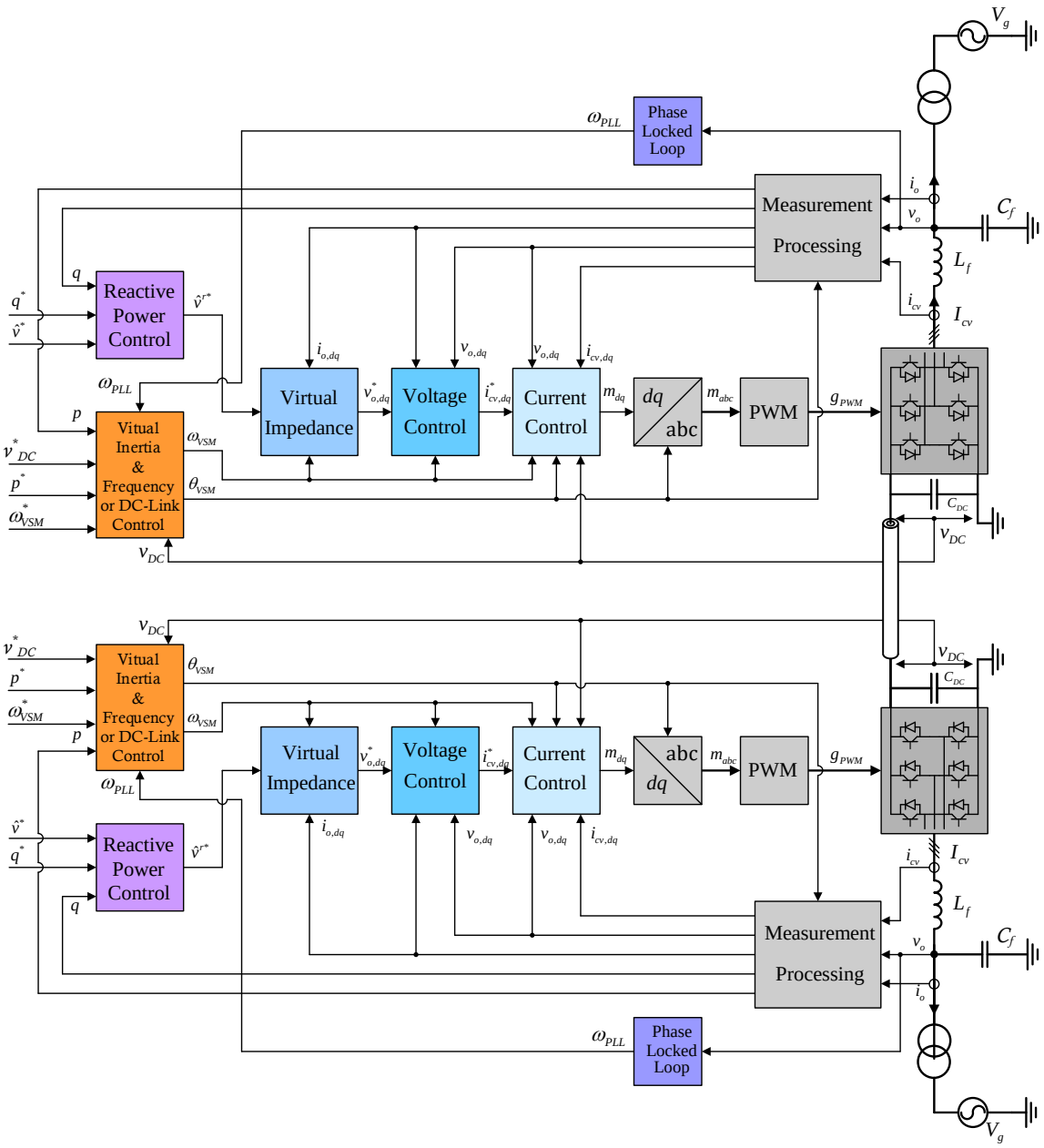

Figure 5.1: *Overview of HVDC control system for a two-level converter with two VSMs.*

from HVDC interconnections. In chapter 2, it has been proposed a configuration where only

one VSC controls the DC-link while the other provides inertia support.

Figure 5.1 shows the overview of the innovative HVDC control scheme for two-level VSC. It is possible to notice that both converters are implemented with the virtual synchronous machine presented in section 2.3. Furthermore, the control system implementation includes an additional block composed by a PI regulator for the DC-link voltage control.

It should be noted that the presented control implementation corresponds to the already described control scheme of section 2.2 excepts for the DC-link control. Moreover, the modelling conventions described are still the same as well as the electrical system equations.

5.2 VSM inertia emulation with active power droop and DC-link voltage control

This section presents the only difference between the already analysed and the new VSM control system implementation. The emulation of a rotating inertia and the power balance synchronization mechanisms of the investigated VSM control structure maintains the working principle described in subsection 2.3.1. In other words, the swing equation used for the implementation is linearized with respect to the speed so that the acceleration of the inertia is determined by the power balance according to Equation 2.12.

The presented swing equation is characterized by the external frequency droop, equivalent

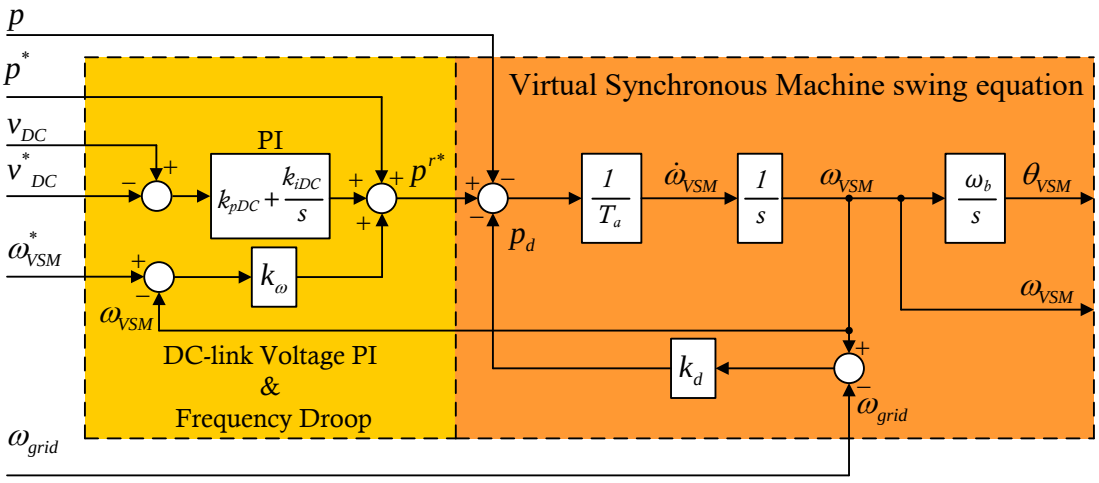

Figure 5.2: *VSM inertia emulation with active power-frequency droop and DC-link voltage control.*

to the steady-state characteristics of the speed governor for a traditional synchronous machine.

However, Equation 2.12 misses the contribution obtained by the DC-link control as shown in the left part of Figure 5.2.

The DC-link voltage PI and power-frequency droop is characterized by two contribution which modify the virtual mechanical input power p^{r^*} to the swing equation. It is given by the sum of the external power reference set-point p^*, the frequency droop effect and the DC-link voltage contribution. Thus, the power balance of the VSM inertia can be expressed by Equation 5.1, where the DC-link PI controller gains are defined by k_{pDC} and k_{iDC}. The state κ is defined to represent the integrator of the PI DC-link voltage controller as given by Equation 5.2

$$\frac{d\delta\omega_{VSM}}{dt} = \frac{p^*}{T_a} - \frac{p}{T_a} - \frac{k_d(\omega_{VSM} - \omega_{PLL})}{T_a} - \frac{k_\omega(\omega_{VSM} - \omega^*)}{T_a} + \frac{k_{pDC}(v_{DC} - v_{DC}^*)}{T_a} + \frac{k_{iDC} \cdot \kappa}{T_a} \quad (5.1)$$

$$\frac{d\kappa}{dt} = v_{DC} - v_{DC}^* \quad (5.2)$$

The objective of the presented control is to provide the inertia support and the primary frequency regulation in both sides of the HVDC link. In this perspective, both the converter should have the possibility to control the DC-link voltage and the frequency through the droop. However, there are a high number of possibilities that stabilize the system but it is tough to find out the best suitable for the inertia support and frequency regulation view point.

In order to obtain a good result for the HVDC inertia support, it has been decide to tune the presented control implementation by the small signal analysis of the system.

5.3 Small signal model of the reference HVDC with two VSMs

Small-signal stability is the ability of the power system to maintain synchronism when subjected to small disturbances. In this context, a disturbance is considered to be small if the equations that describe the resulting response of the system may be linearized for the purpose of analysis.

Instability that may result can be of two forms:

1) Steady increase in the generator rotor angle due to a lack of synchronizing torque;

2) Rotor oscillations of increasing amplitude due to lack of sufficient damping torque.

Small-signal analysis using linear techniques provides valuable information about the inherent dynamic characteristics of the power system and assists in its design.

All the equations needed for detailed modelling of the HVDC with two VSMs in the grid connected operation have been presented in the previous sections, and can be reduced to a model

on state-space form with 43 distinct state variables and 14 input signals, with the state vector $\mathbf{x}$ and the input vector $\mathbf{u}$ defined by 5.3.

$$\begin{aligned}\mathbf{x} = [&v_{on,d} \quad v_{on,q} \quad i_{cvn,d} \quad i_{cvn,q} \quad \gamma_{n,d} \quad \gamma_{n,q} \quad i_{on,d} \quad i_{on,q} \quad \phi_{n,d} \quad \phi_{n,q} \quad v_{PLLn,d} \quad v_{PLLn,q} \quad \dots \\ &\dots \epsilon_n \quad \delta\theta_{VSMn} \quad \xi_{n,d} \quad \xi_{n,q} \quad q_{mn} \quad \delta\omega_{VSMn} \quad \delta\theta_{PLLn} \quad v_{dcn} \quad i_{en} \quad v_{dce} \quad v_{oe,d} \quad v_{oe,q} \quad \dots \\ &\dots i_{cve,d} \quad i_{cve,q} \quad \gamma_{e,d} \quad \gamma_{e,q} \quad i_{oe,d} \quad i_{oe,q} \quad \phi_{e,d} \quad \phi_{e,q} \quad v_{PLLe,d} \quad v_{PLLe,q} \quad \epsilon_e \quad \delta\theta_{VSMe} \quad \dots \\ &\dots \xi_{e,d} \quad \xi_{e,q} \quad q_{me} \quad \delta\omega_{VSMe} \quad \delta\theta_{PLLe} \quad \kappa_e]^T \\ \mathbf{u} = [&p_n^* \quad q_n^* \quad \hat{v}_{gn} \quad \hat{v}_n^* \quad \omega_n^* \quad \omega_{gn} \quad v_{dcn}^* \quad p_e^* \quad q_e^* \quad \hat{v}_{ge} \quad \hat{v}_e^* \quad \omega_e^* \quad \omega_{ge} \quad v_{dce}^*]^T \end{aligned} \tag{5.3}$$

The resulting non-linear state-space model of the overall system is reported in Appendix 5.4.2 and can be expressed as 5.4:

$$\dot{\mathbf{x}} = \mathbf{f}(\mathbf{x}, \mathbf{u}) \tag{5.4}$$

The output variables which can be observed on the system are often of interest. These may be expressed in terms of the state variables and the input variables in the following form:

$$\mathbf{y} = \mathbf{g}(\mathbf{x}, \mathbf{u}) \tag{5.5}$$

5.3.1 Linearization

The procedure to linearize the system described by Equation 5.4 is presented in this section. Considering the intial state $\mathbf{x_0}$ and the input vector $\mathbf{u_0}$ corresponding to the equilibrium point about which the small-signal performance is to be investigated. The steady-state operation point of the system under any combinations of the input signals can be found by solving the non-linear system model with the derivative terms set to zero, as 5.6:

$$\dot{\mathbf{x}} = \mathbf{f}(\mathbf{x_0}, \mathbf{u_0}) = 0 \tag{5.6}$$

From the practical view point, the initial state $\mathbf{x_0}$ corresponds to the array of state variable which respect the equivalence in Equation 5.6 when the input vector $\mathbf{u_0}$ has been set according to, where all the quantities are expressed in per unit:

$p_n^* = 0.5$	$\hat{v}_{gn} = 1$	$q_n^* = 0$	$\hat{v}_n^* = 1$	$\omega_n^* = 1$	$\omega_{gn} = 1$	$v_{dcn}^* = 1$
$p_e^* = -0.5$	$\hat{v}_{ge} = 1$	$q_e^* = 0$	$\hat{v}_e^* = 1$	$\omega_e^* = 1$	$\omega_{ge} = 1$	$v_{dce}^* = 1$

The physical parameters and the quantities used for the tuning of the controllers used in the HVDC with two VSMs control system implementation are listed in Table 5.1. It can be noticed that the values of the parameters equal for both the VSCs are not characterized by any subscript.

Table 5.1: *Parameters of the HVDC with two VSMs control system implementation*

Parameter		Value	Parameter		Value
Rated Voltage	$V_s[kV]$	232,7	Filter inductance	$l_f[pu]$	0.08
Rated power	$S_b[MVA]$	750	Filter resistance	$r_f[pu]$	0.003
Rated angular frequency	$\omega_b[rad/s]$	2π*50	Filter capacitance	$c_f[pu]$	0.074
Grid inductance Norway	$l_{g,n}[pu]$	0.0308	Grid resistance Norway	$r_{g,n}[pu]$	9e-4
Grid inductance Europe	$l_{g,e}[pu]$	0.0133	Grid resistance Europe	$r_{g,e}[pu]$	4e-4
DC cable inductance	$l_{dc}[pu]$	0.0	DC cable capacitance	$c_{dc}/2[pu]$	2.12
DC cable resistance	$r_{dc}[pu]$	0.086	DC cable conductance	$g_{dc}/2[pu]$	1.7e-3
PLL filter	$\omega_{LP}[rad/s]$	500	PLL design constant	a_{PLL}	3
PLL proportional gain	$k_{p,PLL}[pu]$	0.084	PLL integral gain	$k_{i,PLL}[pu]$	4.69
Active damping gain	$k_{AD}[pu]$	1	Active damping filter	$\omega_{AD}[rad/s]$	50
Proportional gain c.c.	$k_{pc}[pu]$	1.27	Integral gain c.c.	$k_{ic}[pu]$	14.3
Proportional gain v.c	$k_{pv}[pu]$	0.59	Integral gain v.c.	$k_{iv}[pu]$	736
Inductance v.i.	$l_v[pu]$	0.2	Resistance v.i.	$r_v[pu]$	0.0
VSM Inertia Time	$T_a[s]$	2	VSM damping coeff.	$k_d[pu]$	400
Droop gain reac. power	$k_q[pu]$	0.2	Reactive power filter	$\omega_f[rad/s]$	1000
Proportional gain DC c.	$k_{p,DCn/e}[pu]$	0, 0.5	Integral gain DC c.	$k_{i,DCe}[pu]$	0.1

Let us now perturb the system from the state reached solving the Equation 5.6, by letting

$$\mathbf{x} = \mathbf{x_0} + \Delta\mathbf{x} \qquad \mathbf{u} = \mathbf{u_0} + \Delta\mathbf{u}$$

where the prefix Δ denotes a small signal deviation.

Since the state-space model from Appendix 5.4.2 is non-linear, classical stability assessment techniques based on eigenvalues are not directly applicable. Thus, a corresponding linearized small-signal state-space model is derived in the form given by 5.7:

$$\begin{cases} \Delta\dot{\mathbf{x}} &= \mathbf{A}\cdot\Delta\mathbf{x} + \mathbf{B}\cdot\Delta\mathbf{u} \\ \Delta\mathbf{y} &= \mathbf{C}\cdot\Delta\mathbf{x} + \mathbf{D}\cdot\Delta\mathbf{u} \end{cases} \tag{5.7}$$

The values of the state variables at this linearization point are denoted by the subscript "0" when they appear in the matrices.

In the Equation 5.7, $\Delta\mathbf{x}$ is the state vector of dimension n, $\Delta\mathbf{y}$ is the output vector of dimension m and $\Delta\mathbf{u}$ is the input vector of dimension r. Furthermore, $\mathbf{A}$ is the state or dynamic matrix of size $(n \times n)$, $\mathbf{B}$ is the input or control matrix of dimension $(n \times r)$, $\mathbf{C}$ is the output matrix of size $(m \times n)$ and $\mathbf{D}$ is the feed forward matrix, which defines the proportion of input that appears directly in the output, of size $(m \times r)$.

5.3.2 Analysis of stability

According to **Lyapunov's first method**, the *stability in the small* of a nonlinear system is given by the roots of the characteristic equation of the system of first approximations, i.e. by the eigenvalues of $\mathbf{A}$:

(i) When the eigenvalues have negative real parts, the original system is asymptotically stable.

(ii) When at least one the eigenvalues has a positive real part, the original system is unstable.

(iii) When the eigenvalues have real parts equal to zero, it is not possible on the basis of the first approximation to say anything in general.

The time dependent characteristic of a mode corresponding to an eigenvalue λ_i is given by $e^{\lambda_i t}$. Therefore, the stability of the system is determined by the eigenvalues as follows:

(a) A real eigenvalue corresponds to a non-oscillatory mode. A negative real eigenvalue represents a decaying mode. The larger its magnitude, the faster the decay. A positive real eigenvalue represents aperiodic instability.

(b) Complex eigenvalues occur in conjugate pairs, and each pair corresponds to an oscillatory mode.

The root locus of all the system poles for the linearized equilibrium point is represented in Figure 5.3.

As already explained, the system is asymptotically stable only if the eigenvalues have negative real parts. In the lower right chart of Figure 5.3 is possible to see a pair of complex conjugate poles marked with red color which are in the positive real half plane.

According to **Lyapunov's first method** the system results to be *unstable*. In the next subsections, the participation factor and the eigenvalue sensitivity analysis is carried out in order to stabilize the system.

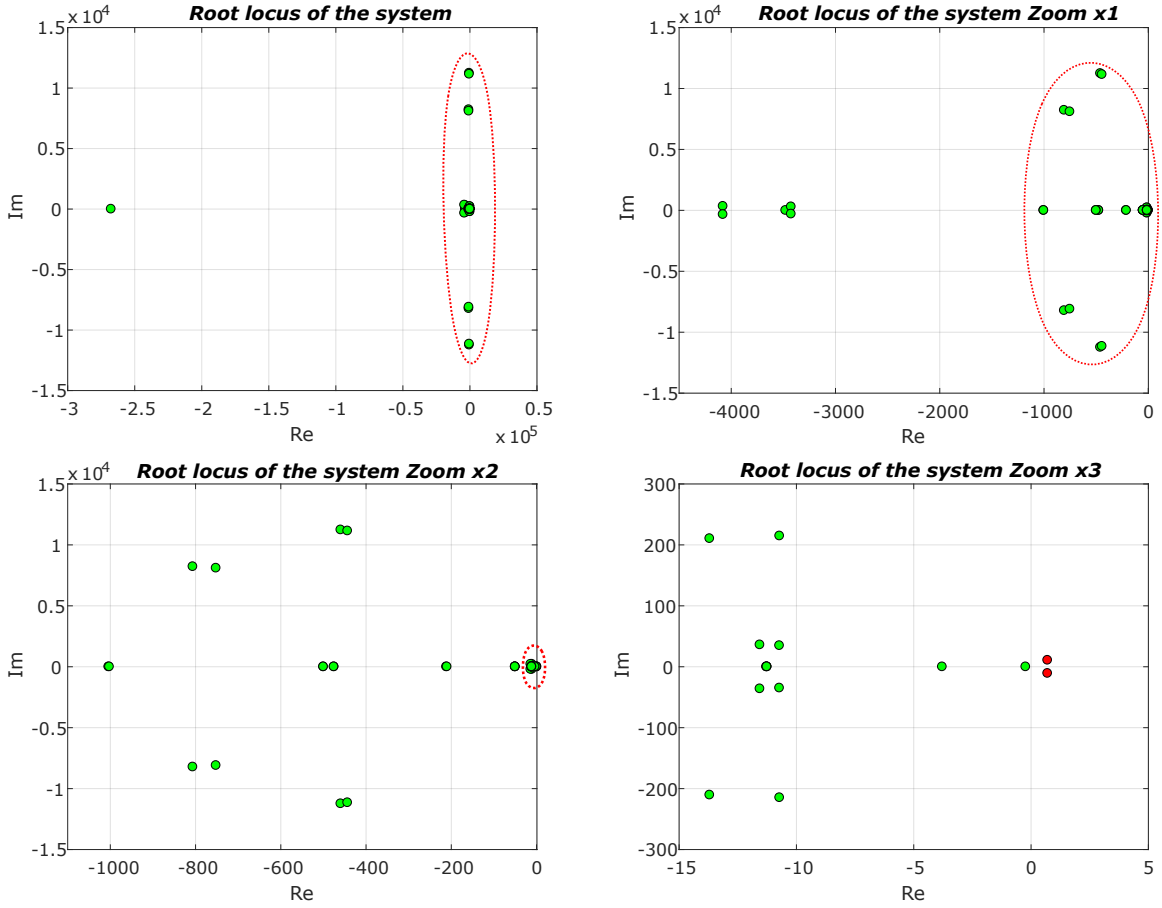

Figure 5.3: *Root locus of all the system poles for the linearized equilibrium point. The four figures represent the progressive zoom of the root locus of all the system.*

Table 5.2: *System eigenvalues - the unstable pair of complex conjugate poles is highlighted with red.*

$\lambda_1 = -267600$	$\lambda_{2,3} = -806.37 \pm j8220.3$	$\lambda_{4,5} = -751.93 \pm j8098.3$	$\lambda_{6,7} = -459.38 \pm j11236$
$\lambda_{8,9} = -443.33 \pm j11151$	$\lambda_{10} = -3478.5$	$\lambda_{11,12} = -3425.1 \pm j297.82$	$\lambda_{13,14} = -4078.7 \pm j337.46$
$\lambda_{15} = -1004$	$\lambda_{16} = -1002.2$	$\lambda_{17} = -475.01$	$\lambda_{18} = -475.37$
$\lambda_{19,20} = -10.718 \pm j214.77$	$\lambda_{21,22} = -13.697 \pm j210.43$	$\lambda_{23} = -500$	$\lambda_{24} = -211.49$
$\lambda_{25} = -210.03$	$\lambda_{26} = -500$	$\lambda_{27,28} = -11.5577 \pm j36.0763$	$\lambda_{29,30} = -10.7234 \pm j34.8010$
$\lambda_{31} = -50.2497$	$\lambda_{32} = -50.0857$	$\lambda_{33} = -50.1028$	$\lambda_{34} = -50.1520$
$\lambda_{35,36} = 0.7038 \pm j10.7876$	$\lambda_{37} = -0.229$	$\lambda_{38} = -3.7851$	$\lambda_{39} = -11.2801$
$\lambda_{40} = -11.2486$	$\lambda_{41} = -11.2570$	$\lambda_{42} = -11.2586$	

5.3.3 Participation factor

In this subsection, a matrix called the participation matrix ($\mathbf{P}$), which combines the right and left eigenvectors as follows is proposed as a measure of the association between the state

variables and the modes.

$$\mathbf{P} = [\mathbf{p}_1 \quad \mathbf{p}_2 \quad \dots \quad \mathbf{p}_n] \tag{5.8}$$

with

$$\mathbf{p}_i = \begin{bmatrix} p_{1i} \\ p_{2i} \\ \vdots \\ p_{ni} \end{bmatrix} = \begin{bmatrix} \Phi_{1i}\Psi_{i1} \\ \Phi_{2i}\Psi_{i2} \\ \vdots \\ \Phi_{ni}\Psi_{in} \end{bmatrix} \tag{5.9}$$

The element $p_{ki} = \Phi_{ki}\Psi_{ik}$ is termed *participation factor* [1]. It is a measure of the relative participation of the kth state variable in the ith mode, and vice versa.

Since Φ_{ki} measures the activity of x_k in the ith mode and Ψ_{ik} weights the contribution of this activity to the mode, the product p_{ki} measures the net participation.

The relative participation of the unstable pair of complex conjugate poles has been conducted and the results have been represented in Figure 5.4.

It should be noted that the phase angle of the virtual synchronous machine in Europe $\delta\theta_{vsme}$

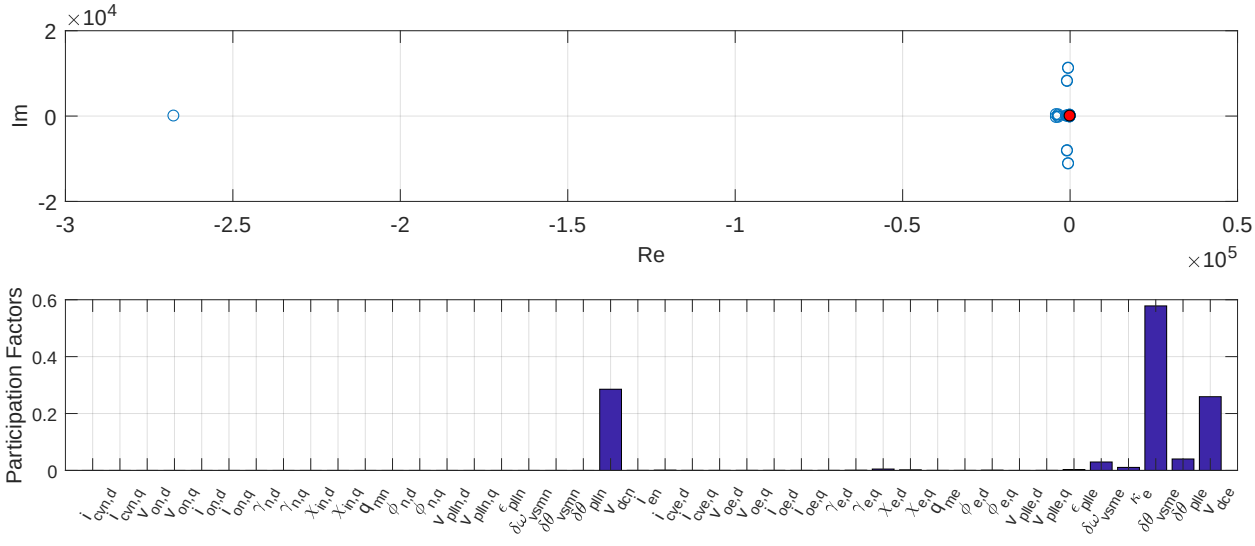

Figure 5.4: *Participation factor of the unstable complex conjugate pair poles.*

and voltage at the DC terminals of both the power electronics converter, i.e. v_{dcn} and v_{dce}.

5.3.4 Eigenvalue sensitivity

Let us now examine the sensitivity of eigenvalues to the elements of the state matrix. Consider Equation 5.10 which defines the eigenvalues and eigenvectors:

$$\mathbf{A}\mathbf{\Phi_i} = \lambda_i \mathbf{\Phi_i} \tag{5.10}$$

differentiating with respect to a_{kj} (the element of $\mathbf{A}$ in kth row and jth column) and manipulating yields:

$$\frac{\partial \lambda_i}{\partial a_{kj}} = \Psi_{ik}\Phi_{ji} \tag{5.11}$$

Thus, the sensitivity of the eigenvalue λ_i to the element a_{kj} of the state matrix is equal to the product of the left eigenvector element Ψ_{ik} and the right eigenvector element Φ_{ji}.

The HVDC control system implementation is characterized by a state matrix $\mathbf{A}$ of size (42×42), which means that there are 42 eigenvalues to be differentiated with respect to each element of the dynamic matrix a_{kj}. However, the HVDC control system implementation under analysis is mainly composed by the VSM control that its stability has been already studied in [12], [20] and [22]. In the previous studies, the DC link has been modelled as an ideal voltage source, while it has parameters limitation both in the control and in physical parameters. Moreover, the participation factor analysis has provided the states that causes the instability of the system. For this reason, it has been decided to perform the eigenvalue sensitivity only with respect to the parameters of the control system which describe the DC link and the VSM coupled dynamics. The list of the parameters are:

$$T_{an} \quad k_{dn} \quad k_{\omega n} \quad k_{p,dcn} \quad T_{ae} \quad k_{de} \quad k_{\omega e} \quad k_{p,dce} \quad k_{i,dce}$$

The parametric sensitivity analysis of the unstable complex conjugate pair poles of the HVDC control system reference implementation with respect to the above set of parameters is shown in the right Figure 5.5.

It should be noted that the parametric sensitivity of a complex conjugate pair of poles is the same. This is the reason why only one of the two charts has been plotted.

The parametric sensitivity proves that the proportional and integral gains of the dc PI controller and the inertia time constant have impact on the unstable pair of complex conjugate poles. It also proves that reducing the mentioned parameters would help to move the poles towards the left and consequently stabilize the system.

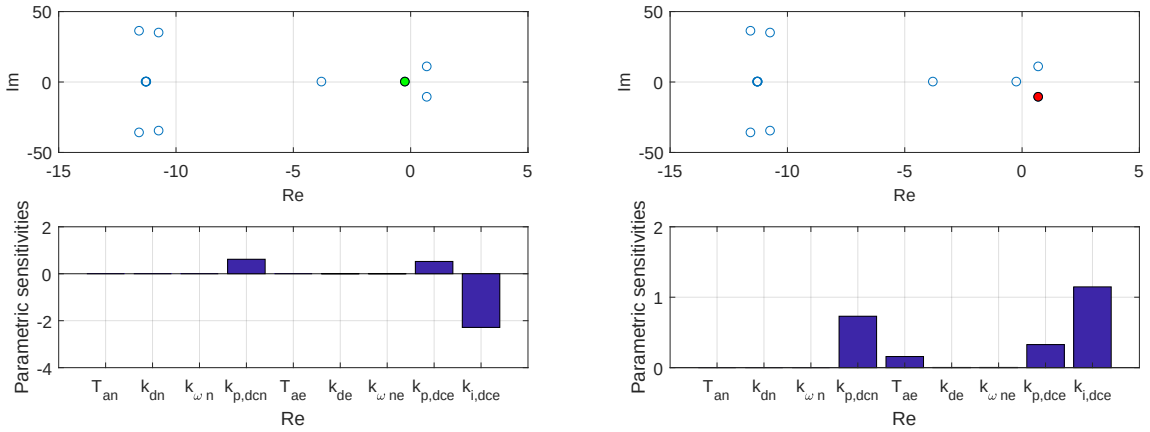

Figure 5.5: *Parametric sensitivity of the unstable complex conjugate pair poles and the low damped pole, right and left part respectively.*

It should be noted that the proportional gain of the DC control in the VSM connected to Norway ($k_{p,dcn}$) is set equal to zero. So, its value cannot be reduced.

Regarding the PI parameters of the DC voltage control in the VSM of Europe, the parametric sensitivity of the low damped pole represented in the left part of Figure 5.5 shows that the reduction of the integral gain of the DC-link PI compensator would move the pole towards an unstable position. Furthermore, it is important to consider the ratio between the proportional $k_{p,dce}$ and integral $k_{i,dce}$ gain of the PI regulator. It is the integral time constant of the controller which should be larger than the inertia time response of the VSM otherwise the inertia support would be limited by the PI compensator, i.e. it has been considered $T_{i,dce} \geq 1s$.

According to the previous consideration it has been chosen a proper tuning for the PI compensator of the DC controller in the European VSC which gives the following values:

$$k_{p,dce} = k_{i,dce} = 1.0pu$$

At this point only the inertia time constant remains to be studied for stabilizing the system. From the parametric sensitivity analysis, it can be noted that the inertia constant of the VSM which controls both the frequency and the DC-link voltage, i.e. T_{ae}, should be decreased to move the unstable poles towards the negative real semi-plane. However, it means to annihilate completely the inertia support of the analysed VSM. Moreover, the inertia constant of both the VSMs have been set to 20 s in order to improve the inertia support.

From the physical point of view, the "mechanical" energy stored in the virtual synchronous machine corresponds to the energy stored in the equivalent capacitance composed by the DC

cable and the additional buffer capacitor connected to the DC terminal of the VSC.

In this thesis, the additional buffer capacitor has not been considered so far. However, it can been noticed the necessity to add an additional capacitance to stabilize the system and furthermore increase the energy exploitable for the inertia support.

In order to design the buffer capacitance, it has been considered the equivalent Modular Multilevel Converter model which would be used for the reference HVDC implementation. The equivalence of the detailed model with respect to an average-value model has been performed in [23], and the robustness and scalability has been demonstrated.

The submodule (SM) capacitor is selected with a value so that the ripple is kept within a range of 5%. To achieve this, the energy stored in each SM should be in the range of 80-100 kJ/MVA [24]. The SM capacitance C_{SM} has been estimated as follow:

$$C_{SM} = \frac{2S_b E_{MMC}}{6N_{arm} v_{cell}^2} \tag{5.12}$$

where E_{MMC} is the energy per megavolt-ampere (MVA) stored in each MMC, S_b is the nominal capacity of the MMC (750MVA), N_{arm} is the number of SMs per multivalve arm (400), and the nominal value for v_{cell} is 1312.5 V. For a stored energy of 100 kJ/MVA, the resulting capacitor value is 36 mF.

The C_{buffer} represents a capacitance equivalent to the detailed model. It is derived using the energy conservation principle:

$$E_{MMC} = 6\frac{1}{2} C_{SM} \sum_{k=1}^{N_{arm}} v_{cell,k}^2 = \frac{1}{2} C_{buffer} V_{dc}^2 \tag{5.13}$$

Assuming all the SMs have the same voltage v_{cell}, the equivalent capacitor C_{buffer} can be derived from:

$$C_{buffer} = \frac{6C_{SM}}{N_{arm}} \tag{5.14}$$

The equivalent value of buffer capacitance C_{buffer} obtained is equal to 544 μF, which corresponds to 18.52 pu. This capacitor would be characterized by a charging time equal to 100 ms or 5 cycles at the fundamental frequency according to Equation 5.15. The value of the buffer capacitance have been swept from 0 pu, which corresponds to the cable only, up to computed value 18.52 pu. The root locus of the eigenvalues during the sweeping is shown in the left part of Figure 5.6.

$$t_{charging} = \frac{\frac{1}{2} C_{buffer} \cdot U_{DC}^2}{P_b} \tag{5.15}$$

It can be noticed that the unstable poles move from the positive real semi-plane to the

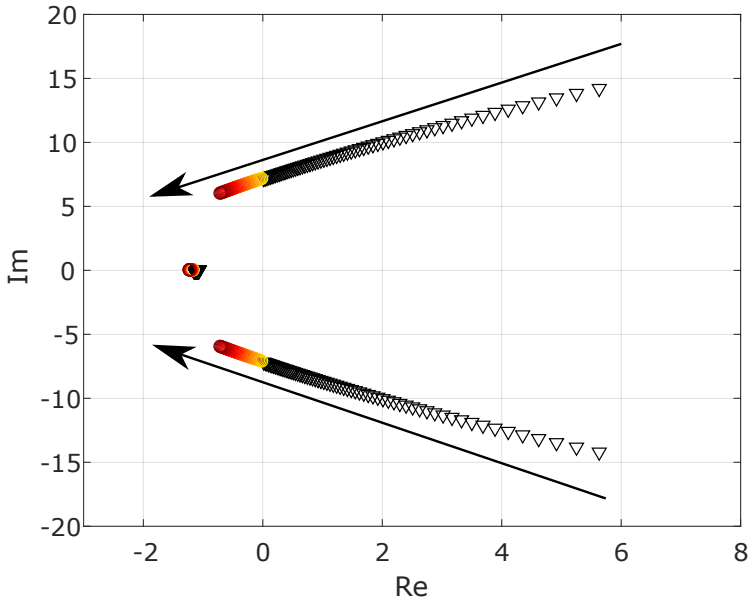

Figure 5.6: *Root locus of the unstable pole pair when the DC buffer capacitances are swept from 0 pu to 18.51 pu*

negative one bringing the system to a stable situation. Moreover, the slowest mode related to the state of the PI compensator of the DC link in the VSM reduces the settling time improving the dynamics of the system.

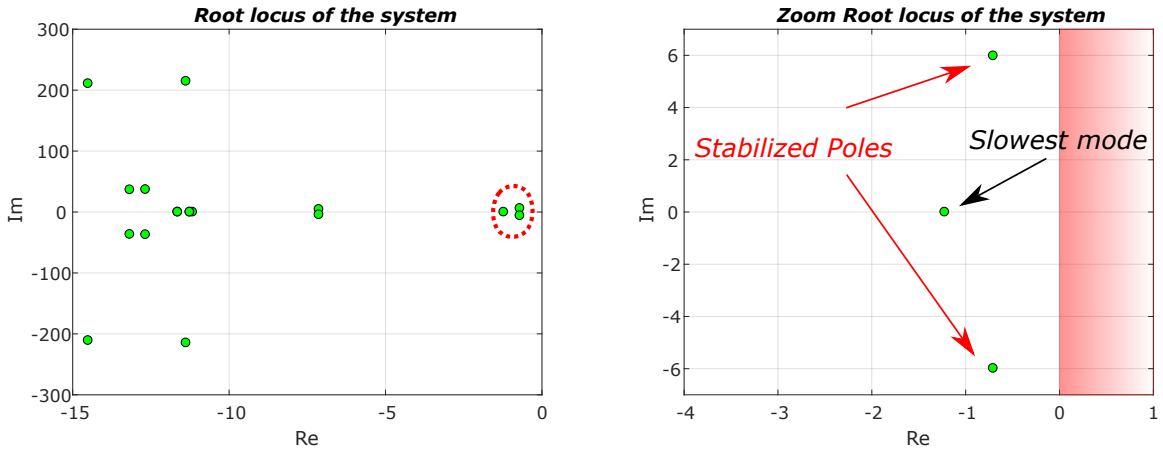

Figure 5.7: *Root locus of all the system poles for the linearized equilibrium point with buffer capacitance.*

The root locus of the system after the addiction of the calculated buffer capacitance and the changing of the inertia time constant is shown in Figure 5.7.

5.4 Dynamic simulations of HVDC control system with two VSMs

This section presents the functional behaviour of the analysed control system implementation by means of numerical simulation of a few relevant cases. The dynamic model of the system coincides to the point to point HVDC transmission system with two VSMs described in the previous sections.

The control system implementation is compared with respect to the HVDC transmission system with VSM and DC-link controlled converters described in chapter 2 and tested in chapter 4. All the simulations results have been executed utilizing *DIgSILENT - Power Factory*, which has been verified to be reliable as well as *Matlab - Simulink*.

As already treated in the previous chapter, the interest of the simulations is focused on two characteristics: the response to change in loading of the VSC and the response to change in the grid frequency because of a load step.

5.4.1 Dynamic response to change in loading with AC ideal voltage sources

In the first simulated case, the dynamic response of the point to point HVDC transmission system with two VSMs is examined for a step in active power reference input to the VSM controlled converter from 0.5 pu to 0.7 pu when the grid frequency and the reference frequency are both equal to 1.0 pu.

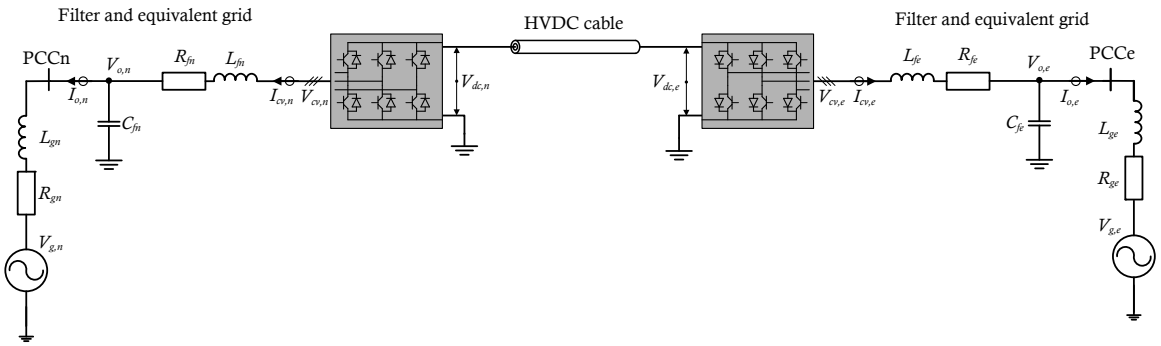

Figure 5.8: *Single-line diagram of a VSC-HVDC transmission system made up by two-level converter connected to AC voltage sources through LC filter.*

The electrical scheme of the defined simulation scenario is shown in Figure 5.8.

All the references quantities used in the investigated HVDC configuration coincide with

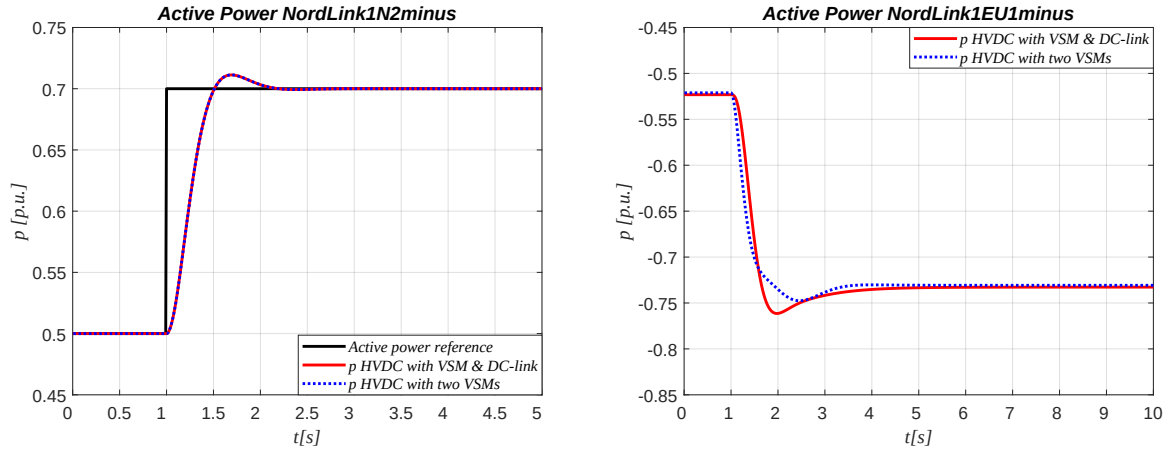

Figure 5.9: *Active power response of HVDC link connected to AC ideal voltage sources to a step in the power reference input - Comparison between HVDC with VSM and DC-link controlled converter and HVDC with two VSMs, solid and dotted line respectively.*

the expressed during the linerization process in section 5.3. Furthermore, the proposed control system implementation is compared with respect to the HVDC transmission system with VSM and DC-link controlled converter, which has been described in the previous chapters. Since the DC buffer capacitor has been added at the DC-link converter terminals, the tuning of the DC-link control has been changed since the equivalent DC capacitance is different. The resultant values of the proportional gain $k_{p,dce}$ and the integral time constant $T_{i,dce}$ are 2.508 pu and 1 s, respectively.

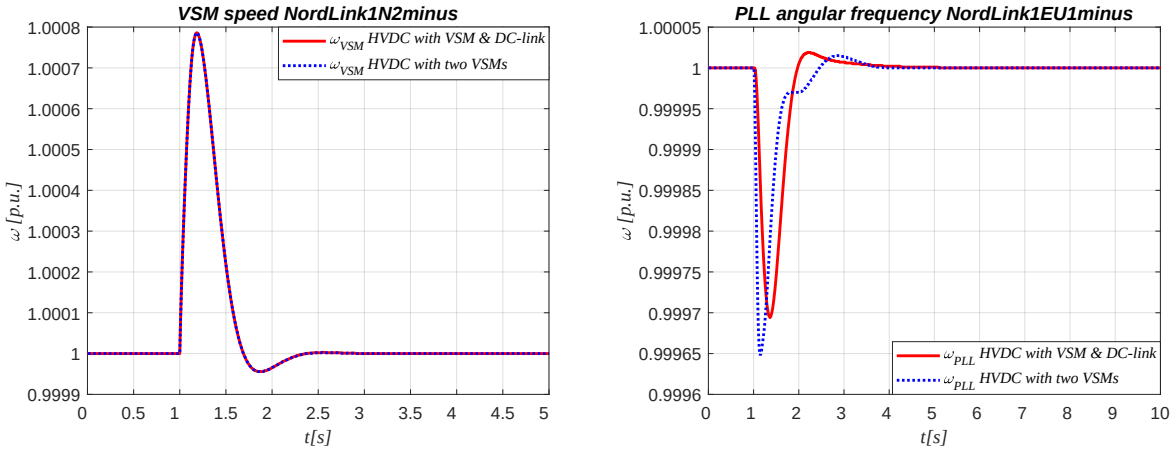

Figure 5.10: *Frequency response of HVDC link connected to AC ideal voltage sources to a step in the power reference input - Comparison between HVDC with VSM and DC-link controlled converter and HVDC with two VSMs, solid and dotted line respectively.*

The power reference and the resulting electrical power from the VSM controlled converter in Norway are plotted in the left part of Figure 5.9, while the active power from the other converter is reported in the right part of Figure 5.9.

It can be easily notice the perfect matching of the active power injected by the VSM in Norway. Obviously, the results coincide since the configuration in that side of the HVDC are the same.

As regards the active power response of the other converter, a deviation in the first seconds

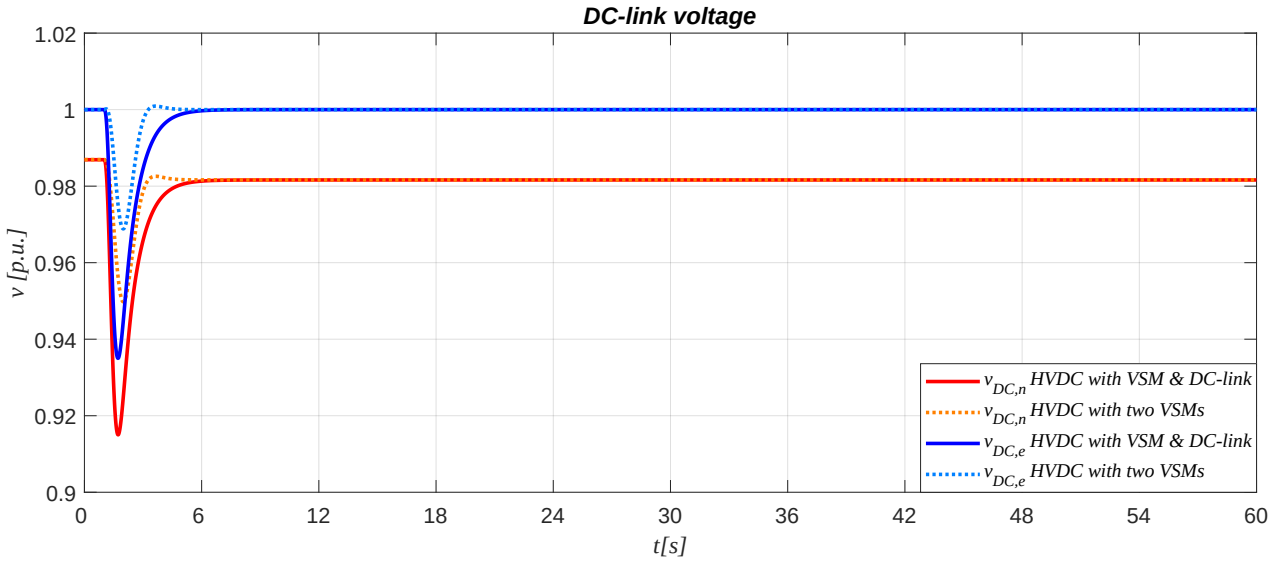

Figure 5.11: *DC voltage response of HVDC link connected to AC ideal voltage sources to a step in the power reference input - Comparison between HVDC with VSM and DC-link controlled converter and HVDC with two VSMs, solid and dotted line respectively.*

can be appreciated. This deviation is mainly characterized by the tuning of the controllers operating to maintain the DC-link constant at steady state operating condition and by the possibility to step both the active power references in the two VSMs controlled configuration.

The rotating speed of the virtual inertia, as already seen in the previous chapter, is triggered by the step change in the active power reference and its response is shown in the left part of Figure 5.10.

The two VSMs implementation, thanks to the dual power step, improves the dc voltage dynamics, producing a smaller deviation from the steady state values of the voltages, as shown in Figure 5.11.

5.4.2 Dynamic response to load step with equivalent AC grids

In this subsection, the inertia support from the point to point HVDC transmission system with two VSMs is evaluated during a frequency transient perturbation caused by a load step in the Nordic power system. As before, the dynamic response of the reference control scheme implementation are compared with respect to the control scheme implementation analysed in chapter 4. Moreover, the frequency droop controlled converter without inertia support has been presented as benchmark for the evaluation of the performance of the implementations.

The single line diagram representing the structure of the equivalent system is shown in Figure 5.12.

The simulation event has been maintained as well as in the previous chapter, which means

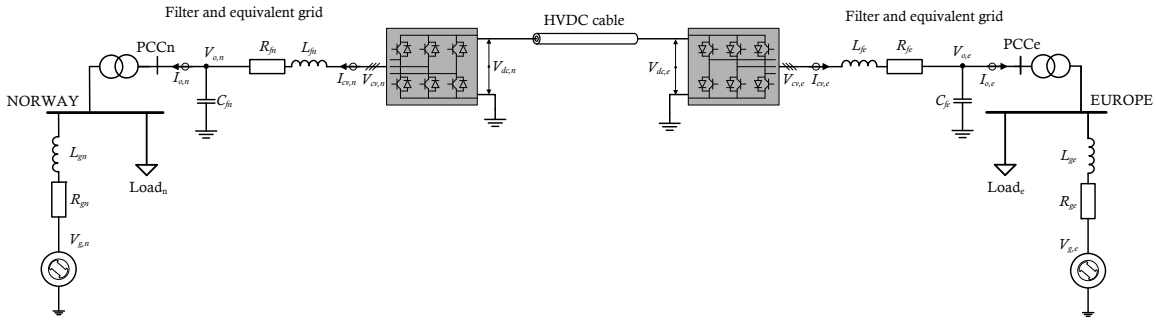

Figure 5.12: *Single-line diagram of a VSC-HVDC transmission system made up by two-level converter connected to equivalent AC grids through LC filter.*

that the load step of 10% of the regional power network closest to the *NordLink* occurs at the time equal to 1 second.

The frequency transient response in both sides of the HVDC interconnector are represented in the upper part of Figure 5.13, while the zoom of the first 10 seconds is shown in the lower part.

It can be noted that the dynamic response of the VSM located in Norway is equivalent in both configurations and improves the frequency transient response with respect the HVDC control system characterized only by the frequency droop control. While the frequency transient in the European side shows different dynamics between the two configuration analysed. In particular, a slight improvement in the dynamics can be appreciated looking at the *Nadir* highlighted in the upper right part of Figure 5.13 using the two VSMs controlled HVDC. Furthermore, the zoom of the transient response of the first 10 seconds shows a smother response in case of two VSMs, which implies less stress for the mechanical component connected in the power network.

The frequency variation triggers the dynamic of the VSM inertia block, which reacts injecting

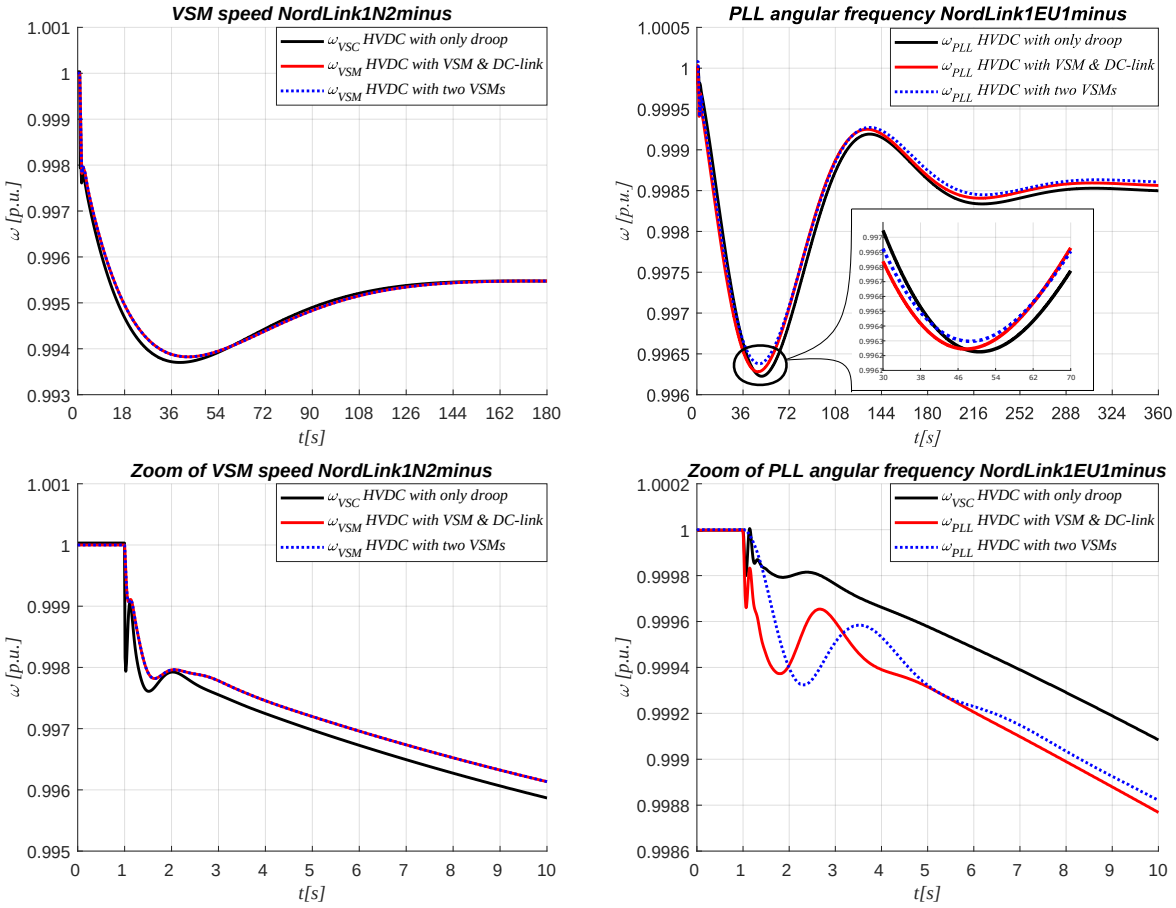

Figure 5.13: *Frequency response of HVDC link connected to equivalent AC grids to a load step - Comparison between HVDC with VSM and DC-link controlled converter and HVDC with two VSMs, solid and dotted line respectively.*

power into the power network as a function of the energy stored in the virtual shaft of the VSM and successively increasing the "mechanical" power thanks to the droop control. The different contributions in the transient response are easily recognizable in the left part of Figure 5.14, where the comparison with respect to the frequency droop without inertia controlled converter is presented. As it is expected, the power responses of the VSM connected to the Nordic power system present the same behaviour for both configurations. On the other hand, the transient response in the other side of the HVDC interconnector is characterized by a notable deviation. This difference is mainly caused by the different dynamics of the two DC-link controllers.

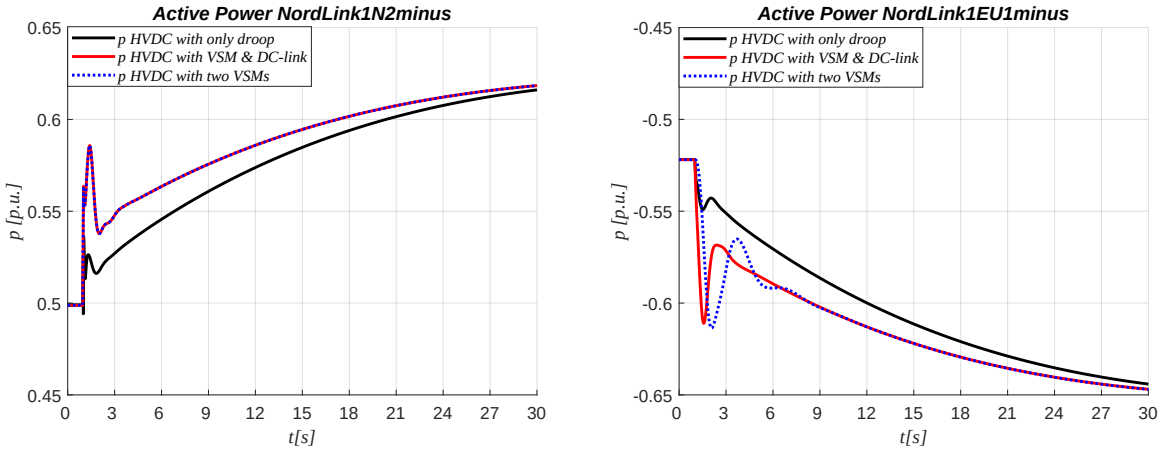

Figure 5.14: *Active power response of HVDC link connected to equivalent AC grids to a load step - Comparison between HVDC with VSM and DC-link controlled converter and HVDC with two VSMs, solid and dotted line respectively.*

Comparing the active power responses at the two sides of the HVDC interconnector it can be noticed that are almost complementary in case of the control scheme with VSM and standard DC-link control, solid red line. The slight different is because of the losses in the DC system and fast transient of the DC voltage. Instead, the two responses of the two VSMs configuration are merely recognizable complementary. The reason of their difference is depicted in Figure 5.15.

The HVDC control scheme with two VSMs exploits more energy stored in the equivalent

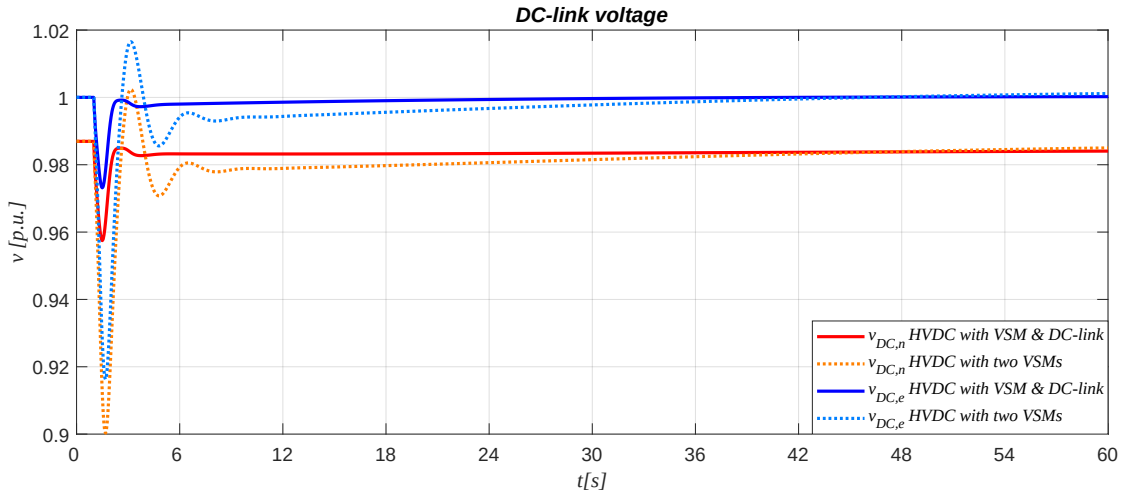

Figure 5.15: *DC voltage transient response of HVDC link connected to equivalent AC grids to a load step - Comparison between HVDC with VSM and DC-link controlled converter and HVDC with two VSMs, solid and dotted line respectively.*

DC capacitances causing a larger voltage drop. However, the minimum voltage such that the overmodulation does not occur is $v_{dc,crit} = 0.8865pu$. So, the response is largely above the limitation.

Chapter conclusion

An innovative control scheme implementation for HVDC transmission system has been presented in this chapter highlighting the main differences with respect to the control scheme described and simulated in the previous chapters.

Subsequently, the small signal model of the system have been built. The equilibrium point for the linearization has been computed and the stability has been studied. It has been shown how to stabilize the system, which was unstable with the first design and tuning, using the participation factor and parametric sensibility analysis. Finally, The stabilized system have been shown.

Lastly, the dynamic simulation of the HVDC control scheme have been presented comparing the result with respect to the HVDC configuration with VSM and standard DC-link control.

Conclusion and Suggestion for Further Research

A short summary of the main results from the previous chapters is presented here. On the basis of these results, possible applications of the developed methods and suggestions for further research on similar topic will be outlined.

Summary of the Main results and contributions

The research question identified in the Abstract of this thesis was to find a control system implementation for HVDC interconnectors which introduces virtual inertia and frequency support. It has been addressed in two steps, as documented in chapter 2 and chapter 5.

In chapter 2, a control scheme for HVDC transmission system with virtual inertia and frequency support only in one side of the interconnector has been proposed. The presented control scheme is characterized by a Virtual Synchronous Machine (VSM) implementation and a standard DC-link control. The mathematical equations of the control scheme implementation have been presented and the non-linear state space model has been reported in Appendix 5.4.2.

The tuning method for the control system has been described step by step in chapter 3 and it has further been presented the dynamic simulations in chapter 4, where the results of *Matlab - Simulink* and *DIgSILENT - Power Factory* has been compared furnishing an equivalence of the software for the simulations. The dynamic response to a step of the active power reference of the VSM and to a load step in the power network have been used to test the performance of the reference control scheme implementation. The results have shown the improvement in the frequency response after the load step in case of inertia support instead of without. Moreover, the sensitivity of the transient response to the inertia constant and the damping coefficient of the VSM has been presented in the last section of chapter 4 providing a good understanding of the dynamics.

The second step to address the objective of this thesis has been carried out in chapter 5, where an innovative control scheme implementation characterized by two VSMs which control both active and reactive power and DC-voltage. The small signal model of the presented control scheme have been built and the stability has been studied. Moreover, the design of the parameters and the tuning of the control have been performed thanks to the state space model.

The dynamic simulations of the innovative control scheme have been compared with respect to the HVDC implementation characterized by VSM and DC-link control. The results show the improvement in the frequency response using the two VSMs control scheme. However, some considerations should point out:

(a) It should be noted that the HVDC control scheme with VSM and DC-link control utilized in the dynamic simulation in chapter 4 is characterized by a marginal contribution due to the low value of inertia constant. However, at the end of the chapter, it has been shown that the tuning might be characterized by a higher value of inertia. On the other hand, the active power injection will be almost completely provided by the DC-link controlled converter, which will cause a frequency disturbance in its power system. As a conclusion, the control scheme presented in chapter 2 and the tuning described in chapter 3 are characterized by a huge frequency propagation through the HVDC interconnector that could be not accepted by the Transmission System Operators.

(b) The HVDC control scheme with two VSMs has shown the necessity to add a buffer capacitance to the VSC DC terminals in order to stabilize the system. The buffer capacitance increases the energy stored in the DC-link providing a increasing of the virtual "kinetic" energy of the two VSMs. For this reason, the control scheme implementation with two VSMs permits to exploit the inertia support in both sides of the HVDC interconnector and provides all the benefits for the frequency and voltage regulation that are not exploitable by the standard DC control implementation.

To conclude, the two control scheme implementations have drawbacks and pros which should be weighted as a function of the application. In this thesis, the *NordLink* HVDC trasmission system have been analysed, which connect two areas managed by different TSOs. For this reason, the control scheme implementation with two VSMs has been considered with better performance giving frequency regulation in both sides and moreover reducing the frequency propagation through the DC-link. However, there are several applications where only one side of the HVDC requires frequency regulation, f.i. HVDC to connect offshore wind power plant to

the shore. In these application, the implementation with VSM and standard DC voltage control might be more useful since it is not necessary to add any buffer capacitance.

Outline of relevant topics for further research

There are several topics that can be relevant for further studies and research by starting from the results presented in the previous chapters. Some of these issues can be of general interest with respect to power system stability studies involving grid integration of VSCs, while other issues are more related to the local control of individual converter units.

A general topics related to power system integration and stability of VSCs in HVDC applications is the quantification of the inertia support. In particular, there are different methods in literature to quantify the inertia support, however it is still an open question to address.

In chapter 5 a possible configuration for inertia support in both sides of the HVDC link has been presented, nevertheless other possible configurations can be used and studied.

Finally, the control scheme implementations should be analysed in a more accurate model of electric power system and proper saturation should be added in case of reaching the limit of the converters.

Closing remarks

Two HVDC control scheme implementations presented in chapter 2 and chapter 5 can be considered as valid solution for inertia support and frequency regulation capability by the power electronics converters in HVDC interconnectors. Thus, the identified research question form the abstract has been addressed, as the presented approach can be potentially adapted for a wide range of applications changing the tuning or the configuration.

Bibliography

[1] Prabha Kundur, Neal J Balu, and Mark G Lauby. *Power system stability and control*, volume 7. McGraw-hill New York, 1994.

[2] USEA USAID. Black sea regional transmission planning project, 2017.

[3] Salvatore D'Arco and Jon Are Suul. Virtual synchronous machines—classification of implementations and analysis of equivalence to droop controllers for microgrids. In *PowerTech (POWERTECH), 2013 IEEE Grenoble*, pages 1–7. IEEE, 2013.

[4] Birron Mathew Weedy, Brian John Cory, Nick Jenkins, Janaka B Ekanayake, and Goran Strbac. *Electric power systems*. John Wiley & Sons, 2012.

[5] Marco Liserre, Frede Blaabjerg, and Steffan Hansen. Design and control of an lcl-filter-based three-phase active rectifier. *IEEE Transactions on industry applications*, 41(5):1281–1291, 2005.

[6] Lennart Harnefors, Antonios Antonopoulos, Staffan Norrga, Lennart Angquist, and Hans-Peter Nee. Dynamic analysis of modular multilevel converters. *IEEE Transactions on Industrial Electronics*, 60(7):2526–2537, 2013.

[7] Nexas. Nordlink hvdc interconnector, 2018.

[8] Walter A Hill and Suresh C Kapoor. Effect of two-level pwm sources on plant power system harmonics. In *Industry Applications Conference, 1998. Thirty-Third IAS Annual Meeting. The 1998 IEEE*, volume 2, pages 1300–1306. IEEE, 1998.

[9] Minyuan Guan, Jingzhou Cheng, Chao Wang, Quanrui Hao, Wulue Pan, Jing Zhang, and Xiang Zheng. The frequency regulation scheme of interconnected grids with vsc-hvdc links. *IEEE Transactions on Power Systems*, 32(2):864–872, 2017.

[10] Cuiqing Du and Evert Agneholm. A novel control of vsc-hvdc for improving power quality of an industrial plant. In *IEEE Industrial Electronics, IECON 2006-32nd Annual Conference on*, pages 1962–1967. IEEE, 2006.

[11] Amirnaser Yazdani and Reza Iravani. *Voltage-sourced converters in power systems: modeling, control, and applications*. John Wiley & Sons, 2010.

[12] Salvatore D'Arco, Jon Are Suul, and Olav B Fosso. Control system tuning and stability analysis of virtual synchronous machines. In *Energy Conversion Congress and Exposition (ECCE), 2013 IEEE*, pages 2664–2671. IEEE, 2013.

[13] Joan Rocabert, Alvaro Luna, Frede Blaabjerg, and Pedro Rodriguez. Control of power converters in ac microgrids. *IEEE transactions on power electronics*, 27(11):4734–4749, 2012.

[14] Vikram Kaura and Vladimir Blasko. Operation of a phase locked loop system under distorted utility conditions. *IEEE Transactions on Industry applications*, 33(1):58–63, 1997.

[15] Salvatore D'Arco, Giuseppe Guidi, and Jon Are Suul. Embedded limitations and protections for droop-based control schemes with cascaded loops in the synchronous reference frame. In *Power Electronics Conference (IPEC-Hiroshima 2014-ECCE-ASIA), 2014 International*, pages 1544–1551. IEEE, 2014.

[16] Remus Teodorescu, Marco Liserre, and Pedro Rodriguez. *Grid converters for photovoltaic and wind power systems*, volume 29. John Wiley & Sons, 2011.

[17] Salvatore D'Arco, Jon Are Suul, and Marta Molinas. Implementation and analysis of a control scheme for damping of oscillations in vsc-based hvdc grids. In *Power Electronics and Motion Control Conference and Exposition (PEMC), 2014 16th International*, pages 586–593. IEEE, 2014.

[18] Werner Leonhard. *Control of electrical drives*. Springer Science & Business Media, 2001.

[19] Simone Buso and Paolo Mattavelli. Digital control in power electronics. *Lectures on power electronics*, 1(1):1–158, 2006.

[20] Salvatore D'Arco, Jon Are Suul, and Olav B Fosso. A virtual synchronous machine implementation for distributed control of power converters in smartgrids. *Electric Power Systems Research*, 122:180–197, 2015.

[21] Chandra Bajracharya, Marta Molinas, Jon Are Suul, Tore M Undeland, et al. Understanding of tuning techniques of converter controllers for vsc-hvdc. In *Nordic Workshop on Power and Industrial Electronics (NORPIE/2008), June 9-11, 2008, Espoo, Finland.* Helsinki University of Technology, 2008.

[22] Salvatore D'Arco, Jon Are Suul, and Olav B Fosso. Small-signal modeling and parametric sensitivity of a virtual synchronous machine in islanded operation. *International Journal of Electrical Power & Energy Systems*, 72:3–15, 2015.

[23] Jaime Peralta, Hani Saad, Sébastien Dennetière, Jean Mahseredjian, and Samuel Nguefeu. Detailed and averaged models for a 401-level mmc-hvdc system. *IEEE Transactions on Power Delivery*, 27(3):1501, 2012.

[24] G. Asplund L. Harnefors B. Jacobson, P. Karlsson and T. Jonsson. Vsc-hvdc transmission with cascaded two-level converters. *Proc. CIGRE Conf., Paris, France*, page B4–110., 2010.

Appendix A

Non-Linear State Space Model of HVDC with VSM and DC control

$$\frac{dv_{on,d}}{dt} = \omega_b \omega_{gn} v_{on,q} + \frac{\omega_b}{c_{fn}} i_{cvn,d} - \frac{\omega_b}{c_{fn}} i_{on,d}$$

$$\frac{dv_{on,q}}{dt} = \omega_b \omega_{gn} v_{on,d} + \frac{\omega_b}{c_{fn}} i_{cvn,q} - \frac{\omega_b}{c_{fn}} i_{on,q}$$

$$\begin{aligned}\frac{di_{cvn,d}}{dt} &= \frac{\omega_b(k_{ffvn} - 1 - k_{ADn} - k_{pcn}k_{pvn})}{l_{fn}} v_{on,d} - \frac{\omega_b c_{fn} k_{pcn}}{l_{fn}} \omega_{gn} v_{on,q} - \frac{\omega_b(k_{pcn} + r_{fn})}{l_{fn}} i_{cvn,d} + \frac{\omega_b k_{icn}}{l_{fn}} \gamma_{n,d} \\ &+ \frac{\omega_b k_{pcn}(k_{ffin} - k_{pvn} r_{vn})}{l_{fn}} i_{on,d} + \frac{\omega_b k_{pcn} k_{pvn} l_{vn}}{l_{fn}} \omega_{gn} i_{on,q} + \frac{\omega_b k_{ADn}}{l_{fn}} \phi_{n,d} + \frac{\omega_b k_{ivn} k_{pcn}}{l_{fn}} \xi_{n,d} \\ &- \frac{\omega_b k_{pcn} k_{pvn} k_{qn}}{l_{fn}} q_{mn} - \omega_b i_{cvn,q} \delta\omega_{VSMn} + \frac{\omega_b k_{pcn} k_{pvn} l_{vn}}{l_{fn}} i_{on,q} \delta\omega_{VSMn} - \frac{\omega_b c_{fn} k_{pcn}}{l_{fn}} v_{on,q} \delta\omega_{VSMn} \\ &+ \frac{\omega_b k_{pcn} k_{pvn} k_{qn}}{l_{fn}} q_n^* + \frac{\omega_b k_{pcn} k_{pvn}}{l_{fn}} \hat{v}_n^*\end{aligned}$$

$$\begin{aligned}\frac{di_{cvn,q}}{dt} &= \frac{\omega_b(k_{ffvn} - 1 - k_{ADn} - k_{pcn}k_{pvn})}{l_{fn}} v_{on,q} + \frac{\omega_b c_{fn} k_{pcn}}{l_{fn}} \omega_{gn} v_{on,d} - \frac{\omega_b(k_{pcn} + r_{fn})}{l_{fn}} i_{cvn,q} + \frac{\omega_b k_{icn}}{l_{fn}} \gamma_{n,q} \\ &+ \frac{\omega_b k_{pcn}(k_{ffin} - k_{pvn} r_{vn})}{l_{fn}} i_{on,q} - \frac{\omega_b k_{pcn} k_{pvn} l_{vn}}{l_{fn}} \omega_{gn} i_{on,d} + \frac{\omega_b k_{ADn}}{l_{fn}} \phi_{n,q} + \frac{\omega_b k_{ivn} k_{pcn}}{l_{fn}} \xi_{n,q} \\ &+ \omega_b i_{cvn,d} \delta\omega_{VSMn} - \frac{\omega_b k_{pcn} k_{pvn} l_{vn}}{l_{fn}} i_{on,d} \delta\omega_{VSMn} + \frac{\omega_b c_{fn} k_{pcn}}{l_{fn}} v_{on,d} \delta\omega_{VSMn}\end{aligned}$$

$$\begin{aligned}\frac{\gamma_{n,d}}{dt} &= -k_{pvn} v_{on,d} - c_{fn} \omega_{gn} v_{on,q} - i_{cvn,d} + (k_{ffin} - k_{pvn} r_{vn}) i_{on,d} + k_{pvn} l_{vn} \omega_{gn} i_{on,q} + k_{ivn} \xi_{n,d} - k_{pvn} k_{qn} q_{mn} \\ &+ k_{pvn} l_{vn} i_{on,q} \delta\omega_{VSMn} - c_{fn} v_{on,q} \delta\omega_{VSMn} + k_{pvn} k_{qn} q_n^* + k_{pvn} \hat{v}_n^*\end{aligned}$$

$$\begin{aligned}\frac{\gamma_{n,q}}{dt} &= +k_{pvn} v_{on,q} + c_{fn} \omega_{gn} v_{on,d} - i_{cvn,q} + (k_{ffin} - k_{pvn} r_{vn}) i_{on,q} - k_{pvn} l_{vn} \omega_{gn} i_{on,d} + k_{ivn} \xi_{n,q} \\ &- k_{pvn} l_{vn} i_{on,d} \delta\omega_{VSMn} + c_{fn} v_{on,d} \delta\omega_{VSMn}\end{aligned}$$

$$\frac{di_{on,d}}{dt} = \frac{\omega_b}{l_{gn}} v_{on,d} - \frac{\omega_b r_{gn}}{l_{gn}} i_{on,d} + \omega_b \omega_{gn} i_{on,q} + \frac{\omega_b \hat{v}_{gn}}{l_{gn}} cos(\delta\theta_{VSMn})$$

$$\frac{di_{on,q}}{dt} = \frac{\omega_b}{l_{gn}} v_{on,q} - \frac{\omega_b r_{gn}}{l_{gn}} i_{on,q} - \omega_b \omega_{gn} i_{on,d} + \frac{\omega_b \hat{v}_{gn}}{l_{gn}} sin(\delta\theta_{VSMn})$$

$$\frac{\phi_{n,d}}{dt} = \omega_{ADn} v_{on,d} - \omega_{ADn} \phi_{n,d}$$
$$\frac{\phi_{n,q}}{dt} = \omega_{ADn} v_{on,q} - \omega_{ADn} \phi_{n,q}$$
$$\frac{v_{PLLn,d}}{dt} = \omega_{LP,PLLn} v_{on,d} cos(\delta\theta_{PLLn} - \delta\theta_{VSMn}) + \omega_{LP,PLLn} v_{on,q} sin(\delta\theta_{PLLn} - \delta\theta_{VSMn}) - \omega_{LP,PLLn} v_{PLLn,d}$$
$$\frac{v_{PLLn,q}}{dt} = -\omega_{LP,PLLn} v_{on,d} sin(\delta\theta_{PLLn} - \delta\theta_{VSMn}) + \omega_{LP,PLLn} v_{on,q} cos(\delta\theta_{PLLn} - \delta\theta_{VSMn}) - \omega_{LP,PLLn} v_{PLLn,q}$$
$$\frac{d\epsilon_{PLLn}}{dt} = tan^{-1}\left(\frac{v_{PLLn,q}}{v_{PLLn,d}}\right)$$
$$\frac{\delta\theta_{VSMn}}{dt} = \omega_b \delta\omega_{VSMn}$$
$$\frac{d\xi_{n,d}}{dt} = -v_{on,d} - r_{vn} i_{on,d} + l_{vn}\omega_{gn} i_{on,q} - k_{qn} q_{mn} + l_{vn} i_{on,q} \delta\omega_{VSMn} + k_{qn} q_n^* + \hat{v}_n^*$$
$$\frac{d\xi_{n,q}}{dt} = -v_{on,q} - r_{vn} i_{on,q} - l_{vn}\omega_{gn} i_{on,d} - l_{vn} i_{on,d} \delta\omega_{VSMn}$$
$$\frac{dq_{mn}}{dt} = -\omega_{fn} i_{on,q} v_{on,d} + \omega_{fn} i_{on,d} v_{on,q} - \omega_{fn} q_{mn}$$
$$\frac{d\delta\omega_{VSMn}}{dt} = -\frac{1}{T_{an}} i_{on,d} v_{on,d} - \frac{1}{T_{an}} i_{on,q} v_{on,q} + \frac{k_{dn} k_{p,PLLn}}{T_{an}} tan^{-1}\left(\frac{v_{PLLn,q}}{v_{PLLn,d}}\right) + \frac{k_{dn} k_{i,PLLn}}{T_{an}} \epsilon_{PLLn}$$
$$- \frac{k_{dn} - k_{\omega n}}{T_{an}} \delta\omega_{VSMn} + \frac{1}{T_{an}} p_n^* + \frac{k_{\omega n}}{T_{an}} \omega_n^* - \frac{k_{\omega n}}{T_{an}} \omega_g$$
$$\frac{d\delta\theta_{PLLn}}{dt} = \omega_b k_{p,PLLn} tan^{-1}\left(\frac{v_{PLLn,q}}{v_{PLLn,d}}\right) + \omega_b k_{i,PLLn} \epsilon_{PLLn}$$
$$\frac{dv_{dcn}}{dt} = \frac{\omega_b}{c_{dcn}} i_{en} + \frac{\omega_b k_{pcn}}{c_{dcn} v_{dcn}} i_{cvn,d}^2 + \frac{\omega_b (k_{ADn} - k_{ffvn} + k_{pcn} k_{pvn})}{c_{dcn} v_{dcn}} i_{cvn,d} v_{on,d} - \frac{\omega_b k_{icn}}{c_{dcn} v_{dcn}} i_{cvn,d} \gamma_{n,d}$$
$$+ \frac{\omega_b k_{pcn} (k_{pvn} r_{vn} - k_{ffin})}{c_{dcn} v_{dcn}} i_{cvn,d} i_{on,d} + \frac{\omega_b k_{pcn} k_{pvn} k_{qn}}{c_{dcn} v_{dcn}} i_{cvn,d} q_{mn} - \frac{\omega_b k_{pcn} k_{pvn} k_{qn}}{c_{dcn} v_{dcn}} i_{cvn,d} q_n^*$$
$$- \frac{\omega_b k_{pcn} k_{pvn}}{c_{dcn} v_{dcn}} i_{cvn,d} \hat{v}_n^* + \frac{\omega_b k_{pcn} k_{ADn}}{c_{dcn} v_{dcn}} i_{cvn,d} \phi_{n,d} + \frac{\omega_b k_{pcn}}{c_{dcn} v_{dcn}} i_{cvn,q}^2 - \frac{\omega_b k_{pcn} (k_{pvn} r_{vn} - k_{ffin})}{c_{dcn} v_{dcn}} i_{cvn,q} i_{on,q}$$
$$+ \frac{\omega_b (k_{ADn} - k_{ffvn} + k_{pcn} k_{pvn})}{c_{dcn} v_{dcn}} i_{cvn,q} v_{on,q} - \frac{\omega_b k_{icn}}{c_{dcn} v_{dcn}} i_{cvn,q} \gamma_{n,q} - \frac{\omega_b k_{pcn} k_{ivn}}{c_{dcn} v_{dcn}} i_{cvn,q} \xi_{n,q} - \frac{\omega_b k_{ADn}}{c_{dcn} v_{dcn}} i_{cvn,q} \phi_{n,q}$$
$$+ \frac{k_{pcn} k_{pvn} l_{vn} \omega_b}{c_{dcn} v_{dcn}} \delta\omega_{VSMn} i_{cvn,q} i_{on,d} + \frac{k_{pcn} k_{pvn} l_{vn} \omega_b \omega_{gn}}{c_{dcn} v_{dcn}} i_{cvn,q} i_{on,d} - \frac{k_{pcn} k_{pvn} l_{vn} \omega_b}{c_{dcn} v_{dcn}} \delta\omega_{VSMn} i_{cvn,d} i_{on,q}$$
$$- \frac{k_{pcn} k_{pvn} l_{vn} \omega_b \omega_{gn}}{c_{dcn} v_{dcn}} i_{cvn,d} i_{on,q} - \frac{k_{pcn} c_{fn} \omega_b}{c_{dcn} v_{dcn}} \delta\omega_{VSMn} i_{cvn,q} v_{on,d} - \frac{k_{pcn} c_{fn} \omega_b \omega_{gn}}{c_{dcn} v_{dcn}} i_{cvn,q} v_{on,d}$$
$$+ \frac{k_{pcn} c_{fn} \omega_b}{c_{dcn} v_{dcn}} \delta\omega_{VSMn} i_{cvn,d} v_{on,q} + \frac{k_{pcn} c_{fn} \omega_b \omega_{gn}}{c_{dcn} v_{dcn}} i_{cvn,d} v_{on,q} - \frac{\omega_b g_{dcn}}{c_{dcn}} v_{dcn}$$
$$\frac{di_{en}}{dt} = \frac{\omega_b}{l_{en}} v_{dcn} - \frac{\omega_b}{l_{en}} v_{dce} - \frac{\omega_b r_{en}}{l_{en}} i_{en}$$
$$\frac{dv_{dce}}{dt} = -\frac{\omega_b k_{pce}}{c_{dce} v_{dce}} i_{cve,d}^2 - \frac{\omega_b k_{pce}}{c_{dce} v_{dce}} i_{cve,q}^2 - \frac{\omega_b k_{ACe} k_{pce}}{c_{dce} v_{dce}} i_{cve,q} \hat{v}_e^* - \frac{\omega_b}{c_{dce} v_{dce}} i_{en} v_{dce} - \frac{\omega_b k_{pce} k_{pDCe}}{c_{dce} v_{dce}} i_{cve,d} v_{dcfe}$$
$$+ \frac{\omega_b k_{pce} k_{pDCe}}{c_{dce} v_{dce}} i_{cve,d} v_{dce}^* + \frac{\omega_b (k_{ADe} - k_{ffve})}{c_{dce} v_{dce}} i_{cve,d} v_{oe,d} + \frac{\omega_b (k_{ADe} - k_{ffve})}{c_{dce} v_{dce}} i_{cve,q} v_{oe,q} + \frac{\omega_b k_{ACe} k_{pce}}{c_{dce} v_{dce}} i_{cve,q} |v_{ome}|$$
$$- \frac{\omega_b k_{ice}}{c_{dce} v_{dce}} i_{cve,d} \gamma_{e,d} - \frac{\omega_b k_{ice}}{c_{dce} v_{dce}} i_{cve,q} \gamma_{e,q} + \frac{\omega_b k_{pce} k_{idce}}{c_{dce} v_{dce}} i_{cve,d} \kappa_e - \frac{\omega_b k_{ADe}}{c_{dce} v_{dce}} i_{cve,d} \phi_{e,d} - \frac{\omega_b k_{ADe}}{c_{dce} v_{dce}} i_{cve,q} \phi_{e,q}$$

$$\frac{di_{cve,d}}{dt} = -\frac{\omega_b(k_{pce}+r_{fe})}{l_{fe}}i_{cve,d} + \frac{\omega_b k_{pce}k_{pDCe}}{l_{fe}}v_{dcfe} - \frac{\omega_b k_{pce}k_{pDCe}}{l_{fe}}v^*_{dce} + \frac{\omega_b(k_{ffve}-1-k_{ADe})}{l_{fe}}v_{oe,d} + \frac{\omega_b k_{ice}}{l_{fe}}\gamma_{e,d}$$
$$- \omega_b k_{i,plle}i_{cve,q}\epsilon_{PLLe} - \frac{\omega_b k_{pce}k_{iDCe}}{l_{fe}}\kappa_e + \frac{\omega_b k_{ADe}}{l_{fe}}\phi_{e,d} - \omega_b k_{p,PLLe}i_{cve,q}tan^{-1}\left(\frac{v_{PLLe,q}}{v_{PLLe,d}}\right)$$

$$\frac{di_{cve,q}}{dt} = -\frac{\omega_b(k_{pce}+r_{fe})}{l_{fe}}i_{cve,q} + \frac{\omega_b k_{pce}k_{ACe}}{l_{fe}}v^*_{ACe} + \frac{\omega_b(k_{ffve}-1-k_{ADe})}{l_{fe}}v_{oe,q} - \frac{\omega_b k_{pce}k_{ACe}}{l_{fe}}|v_{ome}|$$
$$+ \frac{\omega_b k_{ice}}{l_{fe}}\gamma_{e,q} + \omega_b k_{i,plle}i_{cve,d}\epsilon_{PLLe} + \frac{\omega_b k_{ADe}}{l_{fe}}\phi_{e,q} + \omega_b k_{p,PLLe}i_{cve,d}tan^{-1}\left(\frac{v_{PLLe,q}}{v_{PLLe,d}}\right)$$

$$\frac{dv_{oe,d}}{dt} = \omega_b\omega_{ge}v_{oe,q} + \frac{\omega_b}{c_{fe}}i_{cve,d} - \frac{\omega_b}{c_{fe}}i_{oe,d}$$

$$\frac{dv_{oe,q}}{dt} = -\omega_b\omega_{ge}v_{oe,d} + \frac{\omega_b}{c_{fe}}i_{cve,q} - \frac{\omega_b}{c_{fe}}i_{oe,q}$$

$$\frac{di_{oe,d}}{dt} = \frac{\omega_b}{l_{ge}}v_{oe,d} - \frac{\omega_b r_{ge}}{l_{ge}}i_{oe,d} + \omega_b\omega_{ge}l_{ge}i_{oe,q} - \frac{\omega_b\hat{v}_{ge}}{l_{ge}}cos(\delta\theta_{PLLe})$$

$$\frac{di_{oe,q}}{dt} = \frac{\omega_b}{l_{ge}}v_{oe,q} - \frac{\omega_b r_{ge}}{l_{ge}}i_{oe,q} - \omega_b\omega_{ge}l_{ge}i_{oe,d} + \frac{\omega_b\hat{v}_{ge}}{l_{ge}}sin(\delta\theta_{PLLe})$$

$$\frac{d\gamma_{e,d}}{dt} = -i_{cve,d} + k_{pDCe}v_{dcfe} - k_{pDCe}v_{dce} * -k_{iDCe}\kappa_e$$

$$\frac{d\gamma_{e,q}}{dt} = -i_{cve,q} + k_{ACe}v^*_{ACe} - k_{ACe}|v_{ome}|$$

$$\frac{d\phi_{e,d}}{dt} = \omega_{ADe}v_{oe,d} - \omega_{ADe}\phi_{e,d}$$

$$\frac{d\phi_{e,q}}{dt} = \omega_{ADe}v_{oe,q} - \omega_{ADe}\phi_{e,q}$$

$$\frac{dv_{dcfe}}{dt} = \omega_{DCe}v_{dce} - \omega_{DCe}\phi_{dcfe}$$

$$\frac{dv_{PLLe,d}}{dt} = \omega_{LP,PLLe}v_{oe,d} - \omega_{LP,PLLe}v_{PLLe,d}$$

$$\frac{dv_{PLLe,q}}{dt} = \omega_{LP,PLLe}v_{oe,q} - \omega_{LP,PLLe}v_{PLLe,q}$$

$$\frac{d\epsilon_{PLLe}}{dt} = tan^{-1}\left(\frac{v_{PLLe,q}}{v_{PLLe,d}}\right)$$

$$\frac{d\delta\theta_{PLLe}}{dt} = \omega_b k_{i,PLLe}\epsilon_{PLLe}\omega_b k_{p,PLLe}tan^{-1}\left(\frac{v_{PLLe,q}}{v_{PLLe,d}}\right)$$

$$\frac{d\kappa_n}{dt} = -v_{dcn} + v^*_{dcn}$$

$$\frac{d|v_{ome}|}{dt} = \omega_{fve}\sqrt{v^2_{oe,d} + v^2_{oe,2}} - \omega_{fve}|v_{ome}|$$

Appendix B

Non-Linear State Space Model of HVDC with two VSMs

$$\frac{dv_{on,d}}{dt} = \omega_b \omega_{gn} v_{on,q} + \frac{\omega_b}{c_{fn}} i_{cvn,d} - \frac{\omega_b}{c_{fn}} i_{on,d}$$

$$\frac{dv_{on,q}}{dt} = \omega_b \omega_{gn} v_{on,d} + \frac{\omega_b}{c_{fn}} i_{cvn,q} - \frac{\omega_b}{c_{fn}} i_{on,q}$$

$$\begin{aligned}\frac{di_{cvn,d}}{dt} &= \frac{\omega_b(k_{ffvn} - 1 - k_{ADn} - k_{pcn}k_{pvn})}{l_{fn}} v_{on,d} - \frac{\omega_b c_{fn} k_{pcn}}{l_{fn}} \omega_{gn} v_{on,q} - \frac{\omega_b(k_{pcn} + r_{fn})}{l_{fn}} i_{cvn,d} + \frac{\omega_b k_{icn}}{l_{fn}} \gamma_{n,d} \\ &+ \frac{\omega_b k_{pcn}(k_{ffin} - k_{pvn} r_{vn})}{l_{fn}} i_{on,d} + \frac{\omega_b k_{pcn} k_{pvn} l_{vn}}{l_{fn}} \omega_{gn} i_{on,q} + \frac{\omega_b k_{ADn}}{l_{fn}} \phi_{n,d} + \frac{\omega_b k_{ivn} k_{pcn}}{l_{fn}} \xi_{n,d} \\ &- \frac{\omega_b k_{pcn} k_{pvn} k_{qn}}{l_{fn}} q_{mn} - \omega_b i_{cvn,q} \delta\omega_{VSMn} + \frac{\omega_b k_{pcn} k_{pvn} l_{vn}}{l_{fn}} i_{on,q} \delta\omega_{VSMn} - \frac{\omega_b c_{fn} k_{pcn}}{l_{fn}} v_{on,q} \delta\omega_{VSMn} \\ &+ \frac{\omega_b k_{pcn} k_{pvn} k_{qn}}{l_{fn}} q_n^* + \frac{\omega_b k_{pcn} k_{pvn}}{l_{fn}} \hat{v}_n^*\end{aligned}$$

$$\begin{aligned}\frac{di_{cvn,q}}{dt} &= \frac{\omega_b(k_{ffvn} - 1 - k_{ADn} - k_{pcn}k_{pvn})}{l_{fn}} v_{on,q} + \frac{\omega_b c_{fn} k_{pcn}}{l_{fn}} \omega_{gn} v_{on,d} - \frac{\omega_b(k_{pcn} + r_{fn})}{l_{fn}} i_{cvn,q} + \frac{\omega_b k_{icn}}{l_{fn}} \gamma_{n,q} \\ &+ \frac{\omega_b k_{pcn}(k_{ffin} - k_{pvn} r_{vn})}{l_{fn}} i_{on,q} - \frac{\omega_b k_{pcn} k_{pvn} l_{vn}}{l_{fn}} \omega_{gn} i_{on,d} + \frac{\omega_b k_{ADn}}{l_{fn}} \phi_{n,q} + \frac{\omega_b k_{ivn} k_{pcn}}{l_{fn}} \xi_{n,q} \\ &+ \omega_b i_{cvn,d} \delta\omega_{VSMn} - \frac{\omega_b k_{pcn} k_{pvn} l_{vn}}{l_{fn}} i_{on,d} \delta\omega_{VSMn} + \frac{\omega_b c_{fn} k_{pcn}}{l_{fn}} v_{on,d} \delta\omega_{VSMn}\end{aligned}$$

$$\begin{aligned}\frac{\gamma_{n,d}}{dt} &= -k_{pvn} v_{on,d} - c_{fn} \omega_{gn} v_{on,q} - i_{cvn,d} + (k_{ffin} - k_{pvn} r_{vn}) i_{on,d} + k_{pvn} l_{vn} \omega_{gn} i_{on,q} + k_{ivn} \xi_{n,d} - k_{pvn} k_{qn} q_{mn} \\ &+ k_{pvn} l_{vn} i_{on,q} \delta\omega_{VSMn} - c_{fn} v_{on,q} \delta\omega_{VSMn} + k_{pvn} k_{qn} q_n^* + k_{pvn} \hat{v}_n^*\end{aligned}$$

$$\begin{aligned}\frac{\gamma_{n,q}}{dt} &= +k_{pvn} v_{on,q} + c_{fn} \omega_{gn} v_{on,d} - i_{cvn,q} + (k_{ffin} - k_{pvn} r_{vn}) i_{on,q} - k_{pvn} l_{vn} \omega_{gn} i_{on,d} + k_{ivn} \xi_{n,q} \\ &- k_{pvn} l_{vn} i_{on,d} \delta\omega_{VSMn} + c_{fn} v_{on,d} \delta\omega_{VSMn}\end{aligned}$$

$$\frac{di_{on,d}}{dt} = \frac{\omega_b}{l_{gn}} v_{on,d} - \frac{\omega_b r_{gn}}{l_{gn}} i_{on,d} + \omega_b \omega_{gn} i_{on,q} + \frac{\omega_b \hat{v}_{gn}}{l_{gn}} cos(\delta\theta_{VSMn})$$

$$\frac{di_{on,q}}{dt} = \frac{\omega_b}{l_{gn}} v_{on,q} - \frac{\omega_b r_{gn}}{l_{gn}} i_{on,q} - \omega_b \omega_{gn} i_{on,d} + \frac{\omega_b \hat{v}_{gn}}{l_{gn}} sin(\delta\theta_{VSMn})$$

$$\frac{\phi_{n,d}}{dt} = \omega_{ADn} v_{on,d} - \omega_{ADn} \phi_{n,d}$$
$$\frac{\phi_{n,q}}{dt} = \omega_{ADn} v_{on,q} - \omega_{ADn} \phi_{n,q}$$
$$\frac{v_{PLLn,d}}{dt} = \omega_{LP,PLLn} v_{on,d} cos(\delta\theta_{PLLn} - \delta\theta_{VSMn}) + \omega_{LP,PLLn} v_{on,q} sin(\delta\theta_{PLLn} - \delta\theta_{VSMn}) - \omega_{LP,PLLn} v_{PLLn,d}$$
$$\frac{v_{PLLn,q}}{dt} = -\omega_{LP,PLLn} v_{on,d} sin(\delta\theta_{PLLn} - \delta\theta_{VSMn}) + \omega_{LP,PLLn} v_{on,q} cos(\delta\theta_{PLLn} - \delta\theta_{VSMn}) - \omega_{LP,PLLn} v_{PLLn,q}$$
$$\frac{d\epsilon_{PLLn}}{dt} = tan^{-1}\left(\frac{v_{PLLn,q}}{v_{PLLn,d}}\right)$$
$$\frac{\delta\theta_{VSMn}}{dt} = \omega_b \delta\omega_{VSMn}$$
$$\frac{d\xi_{n,d}}{dt} = -v_{on,d} - r_{vn} i_{on,d} + l_{vn} \omega_{gn} i_{on,q} - k_{qn} q_{mn} + l_{vn} i_{on,q} \delta\omega_{VSMn} + k_{qn} q_n^* + \hat{v}_n^*$$
$$\frac{d\xi_{n,q}}{dt} = -v_{on,q} - r_{vn} i_{on,q} - l_{vn} \omega_{gn} i_{on,d} - l_{vn} i_{on,d} \delta\omega_{VSMn}$$
$$\frac{dq_{mn}}{dt} = -\omega_{fn} i_{on,q} v_{on,d} + \omega_{fn} i_{on,d} v_{on,q} - \omega_{fn} q_{mn}$$
$$\begin{aligned}\frac{d\delta\omega_{VSMn}}{dt} = &-\frac{1}{T_{an}} i_{on,d} v_{on,d} - \frac{1}{T_{an}} i_{on,q} v_{on,q} + \frac{k_{dn} k_{p,PLLn}}{T_{an}} tan^{-1}\left(\frac{v_{PLLn,q}}{v_{PLLn,d}}\right) + \frac{k_{dn} k_{i,PLLn}}{T_{an}} \epsilon_{PLLn} \\ &- \frac{k_{dn} - k_{\omega n}}{T_{an}} \delta\omega_{VSMn} + \frac{1}{T_{an}} p_n^* + \frac{k_{\omega n}}{T_{an}} \omega_n^* - \frac{k_{\omega n}}{T_{an}} \omega_g + \frac{k_{pDCn}}{T_{an}} v_{dcn} - \frac{k_{pDCn}}{T_{an}} v_{dcn}^* + \frac{k_{iDCn}}{T_{an}} \kappa_n\end{aligned}$$
$$\frac{d\kappa_n}{dt} = v_{dcn} - v_{dcn}^*$$
$$\frac{d\delta\theta_{PLLn}}{dt} = \omega_b k_{p,PLLn} tan^{-1}\left(\frac{v_{PLLn,q}}{v_{PLLn,d}}\right) + \omega_b k_{i,PLLn} \epsilon_{PLLn}$$
$$\begin{aligned}\frac{dv_{dcn}}{dt} = &\frac{\omega_b}{c_{dcn}} i_{en} + \frac{\omega_b k_{pcn}}{c_{dcn} v_{dcn}} i_{cvn,d}^2 + \frac{\omega_b (k_{ADn} - k_{ffvn} + k_{pcn} k_{pvn})}{c_{dcn} v_{dcn}} i_{cvn,d} v_{on,d} - \frac{\omega_b k_{icn}}{c_{dcn} v_{dcn}} i_{cvn,d} \gamma_{n,d} \\ &+ \frac{\omega_b k_{pcn} (k_{pvn} r_{vn} - k_{ffin})}{c_{dcn} v_{dcn}} i_{cvn,d} i_{on,d} + \frac{\omega_b k_{pcn} k_{pvn} k_{qn}}{c_{dcn} v_{dcn}} i_{cvn,d} q_{mn} - \frac{\omega_b k_{pcn} k_{pvn} k_{qn}}{c_{dcn} v_{dcn}} i_{cvn,d} q_n^* \\ &- \frac{\omega_b k_{pcn} k_{pvn}}{c_{dcn} v_{dcn}} i_{cvn,d} \hat{v}_n^* + \frac{\omega_b k_{pcn} k_{ADn}}{c_{dcn} v_{dcn}} i_{cvn,d} \phi_{n,d} + \frac{\omega_b k_{pcn}}{c_{dcn} v_{dcn}} i_{cvn,q}^2 - \frac{\omega_b k_{pcn} (k_{pvn} r_{vn} - k_{ffin})}{c_{dcn} v_{dcn}} i_{cvn,q} i_{on,q} \\ &+ \frac{\omega_b (k_{ADn} - k_{ffvn} + k_{pcn} k_{pvn})}{c_{dcn} v_{dcn}} i_{cvn,q} v_{on,q} - \frac{\omega_b k_{icn}}{c_{dcn} v_{dcn}} i_{cvn,q} \gamma_{n,q} - \frac{\omega_b k_{pcn} k_{ivn}}{c_{dcn} v_{dcn}} i_{cvn,q} \xi_{n,q} - \frac{\omega_b k_{ADn}}{c_{dcn} v_{dcn}} i_{cvn,q} \phi_{n,q} \\ &+ \frac{k_{pcn} k_{pvn} l_{vn} \omega_b}{c_{dcn} v_{dcn}} \delta\omega_{VSMn} i_{cvn,q} i_{on,d} + \frac{k_{pcn} k_{pvn} l_{vn} \omega_b \omega_{gn}}{c_{dcn} v_{dcn}} i_{cvn,q} i_{on,d} - \frac{k_{pcn} k_{pvn} l_{vn} \omega_b}{c_{dcn} v_{dcn}} \delta\omega_{VSMn} i_{cvn,d} i_{on,q} \\ &- \frac{k_{pcn} k_{pvn} l_{vn} \omega_b \omega_{gn}}{c_{dcn} v_{dcn}} i_{cvn,d} i_{on,q} - \frac{k_{pcn} c_{fn} \omega_b}{c_{dcn} v_{dcn}} \delta\omega_{VSMn} i_{cvn,q} v_{on,d} - \frac{k_{pcn} c_{fn} \omega_b \omega_{gn}}{c_{dcn} v_{dcn}} i_{cvn,q} v_{on,d} \\ &+ \frac{k_{pcn} c_{fn} \omega_b}{c_{dcn} v_{dcn}} \delta\omega_{VSMn} i_{cvn,d} v_{on,q} + \frac{k_{pcn} c_{fn} \omega_b \omega_{gn}}{c_{dcn} v_{dcn}} i_{cvn,d} v_{on,q} - \frac{\omega_b g_{dcn}}{c_{dcn}} v_{dcn}\end{aligned}$$
$$\frac{di_{en}}{dt} = \frac{\omega_b}{l_{en}} v_{dcn} - \frac{\omega_b}{l_{en}} v_{dce} - \frac{\omega_b r_{en}}{l_{en}} i_{en}$$
$$\frac{dv_{oe,d}}{dt} = \omega_b \omega_{ge} v_{oe,q} + \frac{\omega_b}{c_{fe}} i_{cve,d} - \frac{\omega_b}{c_{fe}} i_{oe,d}$$
$$\frac{dv_{oe,q}}{dt} = \omega_b \omega_{ge} v_{oe,d} + \frac{\omega_b}{c_{fe}} i_{cve,q} - \frac{\omega_b}{c_{fe}} i_{oe,q}$$

$$\frac{dv_{dce}}{dt} = \frac{\omega_b}{c_{dce}} i_{en} + \frac{\omega_b k_{pce}}{c_{dce} v_{dce}} i_{cve,d}^2 + \frac{\omega_b (k_{ADe} - k_{ffve} + k_{pce} k_{pve})}{c_{dce} v_{dce}} i_{cve,d} v_{oe,d} - \frac{\omega_b k_{ice}}{c_{dce} v_{dce}} i_{cve,d} \gamma_{e,d}$$
$$+ \frac{\omega_b k_{pce} (k_{pve} r_{ve} - k_{ffie})}{c_{dce} v_{dce}} i_{cve,d} i_{oe,d} + \frac{\omega_b k_{pce} k_{pve} k_{qe}}{c_{dce} v_{dce}} i_{cve,d} q_{me} - \frac{\omega_b k_{pce} k_{pve} k_{qe}}{c_{dce} v_{dce}} i_{cve,d} q_e^*$$
$$- \frac{\omega_b k_{pce} k_{pve}}{c_{dce} v_{dce}} i_{cve,d} \hat{v}_e^* + \frac{\omega_b k_{pce} k_{ADe}}{c_{dce} v_{dce}} i_{cvn,d} \phi_{e,d} + \frac{\omega_b k_{pce}}{c_{dce} v_{dce}} i_{cve,q}^2 - \frac{\omega_b k_{pce} (k_{pve} r_{ve} - k_{ffie})}{c_{dce} v_{dce}} i_{cve,q} i_{oe,q}$$
$$+ \frac{\omega_b (k_{ADe} - k_{ffve} + k_{pce} k_{pve})}{c_{dce} v_{dce}} i_{cve,q} v_{oe,q} - \frac{\omega_b k_{ice}}{c_{dce} v_{dce}} i_{cve,q} \gamma_{e,q} - \frac{\omega_b k_{pce} k_{ive}}{c_{dce} v_{dce}} i_{cve,q} \xi_{e,q} - \frac{\omega_b k_{ADe}}{c_{dce} v_{dce}} i_{cve,q} \phi_{e,q}$$
$$+ \frac{k_{pce} k_{pve} l_{ve} \omega_b}{c_{dce} v_{dce}} \delta\omega_{VSMe} i_{cve,q} i_{oe,d} + \frac{k_{pce} k_{pve} l_{ve} \omega_b \omega_{ge}}{c_{dce} v_{dce}} i_{cve,q} i_{oe,d} - \frac{k_{pce} k_{pve} l_{ve} \omega_b}{c_{dce} v_{dce}} \delta\omega_{VSMe} i_{cve,d} i_{oe,q}$$
$$- \frac{k_{pce} k_{pve} l_{ve} \omega_b \omega_{ge}}{c_{dce} v_{dce}} i_{cve,d} i_{oe,q} - \frac{k_{pce} c_{fe} \omega_b}{c_{dce} v_{dce}} \delta\omega_{VSMe} i_{cve,q} v_{oe,d} - \frac{k_{pce} c_{fe} \omega_b \omega_{ge}}{c_{dce} v_{dce}} i_{cve,q} v_{oe,d}$$
$$+ \frac{k_{pce} c_{fe} \omega_b}{c_{dce} v_{dce}} \delta\omega_{VSMe} i_{cve,d} v_{oe,q} + \frac{k_{pce} c_{fe} \omega_b \omega_{ge}}{c_{dce} v_{dce}} i_{cve,d} v_{oe,q} - \frac{\omega_b g_{dce}}{c_{dce}} v_{dce}$$

$$\frac{di_{cve,d}}{dt} = \frac{\omega_b (k_{ffve} - 1 - k_{ADe} - k_{pce} k_{pve})}{l_{fe}} v_{oe,d} - \frac{\omega_b c_{fe} k_{pce}}{l_{fe}} \omega_{ge} v_{oe,q} - \frac{\omega_b (k_{pce} + r_{fe})}{l_{fe}} i_{cve,d} + \frac{\omega_b k_{ice}}{l_{fe}} \gamma_{e,d}$$
$$+ \frac{\omega_b k_{pce} (k_{ffie} - k_{pve} r_{ve})}{l_{fe}} i_{oe,d} + \frac{\omega_b k_{pce} k_{pve} l_{ve}}{l_{fe}} \omega_{ge} i_{oe,q} + \frac{\omega_b k_{ADe}}{l_{fe}} \phi_{e,d} + \frac{\omega_b k_{ive} k_{pce}}{l_{fe}} \xi_{e,d}$$
$$- \frac{\omega_b k_{pce} k_{pve} k_{qe}}{l_{fe}} q_{me} - \omega_b i_{cve,q} \delta\omega_{VSMe} + \frac{\omega_b k_{pce} k_{pve} l_{ve}}{l_{fe}} i_{oe,q} \delta\omega_{VSMe} - \frac{\omega_b c_{fe} k_{pce}}{l_{fe}} v_{oe,q} \delta\omega_{VSMe}$$
$$+ \frac{\omega_b k_{pce} k_{pve} k_{qe}}{l_{fe}} q_e^* + \frac{\omega_b k_{pce} k_{pve}}{l_{fe}} \hat{v}_e^*$$

$$\frac{di_{cve,q}}{dt} = \frac{\omega_b (k_{ffve} - 1 - k_{ADe} - k_{pce} k_{pve})}{l_{fe}} v_{oe,q} + \frac{\omega_b c_{fe} k_{pce}}{l_{fe}} \omega_{ge} v_{oe,d} - \frac{\omega_b (k_{pce} + r_{fe})}{l_{fe}} i_{cve,q} + \frac{\omega_b k_{ice}}{l_{fe}} \gamma_{e,q}$$
$$+ \frac{\omega_b k_{pce} (k_{ffie} - k_{pve} r_{ve})}{l_{fe}} i_{oe,q} - \frac{\omega_b k_{pce} k_{pve} l_{ve}}{l_{fe}} \omega_{ge} i_{oe,d} + \frac{\omega_b k_{ADe}}{l_{fe}} \phi_{e,q} + \frac{\omega_b k_{ive} k_{pce}}{l_{fe}} \xi_{e,q}$$
$$+ \omega_b i_{cve,d} \delta\omega_{VSMe} - \frac{\omega_b k_{pce} k_{pve} l_{ve}}{l_{fe}} i_{oe,d} \delta\omega_{VSMe} + \frac{\omega_b c_{fe} k_{pce}}{l_{fe}} v_{oe,d} \delta\omega_{VSMe}$$

$$\frac{\gamma_{e,d}}{dt} = -k_{pve} v_{oe,d} - c_{fe} \omega_{ge} v_{oe,q} - i_{cve,d} + (k_{ffie} - k_{pve} r_{ve}) i_{oe,d} + k_{pve} l_{ve} \omega_{ge} i_{oe,q} + k_{ive} \xi_{e,d} - k_{pve} k_{qe} q_{me}$$
$$+ k_{pve} l_{ve} i_{oe,q} \delta\omega_{VSMe} - c_{fe} v_{oe,q} \delta\omega_{VSMe} + k_{pve} k_{qe} q_e^* + k_{pve} \hat{v}_e^*$$

$$\frac{\gamma_{e,q}}{dt} = +k_{pve} v_{oe,q} + c_{fe} \omega_{ge} v_{oe,d} - i_{cve,q} + (k_{ffie} - k_{pve} r_{ve}) i_{oe,q} - k_{pve} l_{ve} \omega_{ge} i_{oe,d} + k_{ive} \xi_{e,q}$$
$$- k_{pve} l_{ve} i_{oe,d} \delta\omega_{VSMe} + c_{fe} v_{oe,d} \delta\omega_{VSMe}$$

$$\frac{di_{oe,d}}{dt} = \frac{\omega_b}{l_{ge}} v_{oe,d} - \frac{\omega_b r_{ge}}{l_{ge}} i_{oe,d} + \omega_b \omega_{ge} i_{oe,q} + \frac{\omega_b \hat{v}_{ge}}{l_{ge}} cos(\delta\theta_{VSMe})$$

$$\frac{di_{oe,q}}{dt} = \frac{\omega_b}{l_{ge}} v_{oe,q} - \frac{\omega_b r_{ge}}{l_{ge}} i_{oe,q} - \omega_b \omega_{ge} i_{oe,d} + \frac{\omega_b \hat{v}_{ge}}{l_{ge}} sin(\delta\theta_{VSMe})$$

$$\frac{\phi_{e,d}}{dt} = \omega_{ADe} v_{oe,d} - \omega_{ADe} \phi_{e,d}$$

$$\frac{\phi_{e,q}}{dt} = \omega_{ADe} v_{oe,q} - \omega_{ADe} \phi_{e,q}$$

$$\frac{d\epsilon_{PLLe}}{dt} = tan^{-1} \left(\frac{v_{PLLe,q}}{v_{PLLe,d}} \right)$$

$$\frac{\delta\theta_{VSMe}}{dt} = \omega_b \delta\omega_{VSMe}$$

$$\frac{v_{PLLe,d}}{dt} = \omega_{LP,PLLe} v_{oe,d} cos(\delta\theta_{PLLe} - \delta\theta_{VSMe}) + \omega_{LP,PLLe} v_{oe,q} sin(\delta\theta_{PLLe} - \delta\theta_{VSMe}) - \omega_{LP,PLLe} v_{PLLe,d}$$

$$\frac{v_{PLLe,q}}{dt} = -\omega_{LP,PLLe} v_{oe,d} sin(\delta\theta_{PLLe} - \delta\theta_{VSMe}) + \omega_{LP,PLLe} v_{oe,q} cos(\delta\theta_{PLLe} - \delta\theta_{VSMe}) - \omega_{LP,PLLe} v_{PLLe,q}$$

$$\frac{d\xi_{e,d}}{dt} = -v_{oe,d} - r_{ve} i_{oe,d} + l_{ve} \omega_{ge} i_{oe,q} - k_{qe} q_{me} + l_{ve} i_{oe,q} \delta\omega_{VSMe} + k_{qe} q_e^* + \hat{v}_e^*$$

$$\frac{d\xi_{e,q}}{dt} = -v_{oe,q} - r_{ve} i_{oe,q} - l_{ve} \omega_{ge} i_{oe,d} - l_{ve} i_{oe,d} \delta\omega_{VSMe}$$

$$\frac{dq_{me}}{dt} = -\omega_{fe} i_{oe,q} v_{oe,d} + \omega_{fe} i_{oe,d} v_{oe,q} - \omega_{fe} q_{me}$$

$$\frac{d\delta\omega_{VSMe}}{dt} = -\frac{1}{T_{ae}} i_{oe,d} v_{oe,d} - \frac{1}{T_{ae}} i_{oe,q} v_{oe,q} + \frac{k_{de} k_{p,PLLe}}{T_{ae}} tan^{-1}\left(\frac{v_{PLLe,q}}{v_{PLLe,d}}\right) + \frac{k_{de} k_{i,PLLe}}{T_{ae}} \epsilon_{PLLe}$$
$$- \frac{k_{de} - k_{\omega e}}{T_{ae}} \delta\omega_{VSMe} + \frac{1}{T_{ae}} p_e^* + \frac{k_{\omega e}}{T_{ae}} \omega_e^* - \frac{k_{\omega e}}{T_{ae}} \omega_g + \frac{k_{pDCe}}{T_{ae}} v_{dce} - \frac{k_{pDCe}}{T_{ae}} v_{dce}^* + \frac{k_{iDCe}}{T_{ae}} \kappa_e$$

$$\frac{d\kappa_e}{dt} = v_{dce} - v_{dce}^*$$

$$\frac{d\delta\theta_{PLLe}}{dt} = \omega_b k_{p,PLLe} tan^{-1}\left(\frac{v_{PLLe,q}}{v_{PLLe,d}}\right) + \omega_b k_{i,PLLe} \epsilon_{PLLe}$$